ScuDo

Scuola di Dottorato ~ Doctoral School

WHAT YOU ARE, TAKES YOU FAR

Doctoral Dissertation

Doctoral Program in Mechanical Engineering (30^{th}cycle)

Design and Characterization of Regenerative Shock Absorbers based on Electrohydrostatic Actuation

By

Yijun Xu

******

Supervisor(s):

Prof. Nicola Amati

Doctoral Examination Committee:

Prof. Lei Zuo, Reviewer, Virginia Polytechnic Institute and State University

Prof. Subhash Rakheja, Reviewer, Concordia University Montreal

Prof. Andrea Tonoli, Committee, Politecnico di Torino

Politecnico di Torino

2018

Declaration

I hereby declare that, the contents and organization of this dissertation constitute my own original work and does not compromise in any way the rights of third parties, including those relating to the security of personal data.

Yijun Xu
2018

* This dissertation is presented in partial fulfillment of the requirements for **Ph.D. degree** in the Graduate School of Politecnico di Torino (ScuDo).

"A man has free choice to the extent that he is rational."

-St. Thomas Aquinas

Acknowledgements

I am grateful to the whole staff of the Mechatronics Laboratory of Politecnico di Torino (LIM) for their constant support and help through my three years of work as a Ph.D. student. Their friendship and professional collaboration allowed for a great deal of personal and professional improvements.

I would like to express my most grateful acknowledgments to my supervisor Prof. Nicola Amati for his professional advice based on his extensive experience. I gratefully acknowledge the director of LIM, Prof. Andrea Tonoli for his generous and creative comments and observations that broadened the limits of our knowledge.

This dissertation was developed within the research contract 236/2016 which was funded by Magneti Marelli Shock Absorbers and coordinated by Politecnico di Torino. During the development of this project, I found invaluable help in my colleague and also a dear friend Ph.D. Eng. Renato Galluzzi, who volunteered to help me during the development of this project. His talent and untiring attitude towards our objectives in the research contributed a lot to this work.

Furthermore, I am grateful to my dear friends Joaquim Girardello Detoni, Maria di Napoli and Qingwen Cui, with whom I have shared all the good moments during my Ph.D. period and these valuable memories in Italy will never be forgotten.

Most of all, I would like to dedicate this work to my family, I am grateful to my father and mother who have always been my stronghold after I left my country to follow this journey in Italy.

Abstract

The trend of reducing the emissions in automotive sector leads to the development of electrification of vehicle powertrain and chassis. Those vehicles equipped with regenerative shock absorbers can transfer the vibrational energy coming through the road irregularities into electricity which can be further used for other purpose, i.e. to charge the battery. To realize the regeneration target, the developed device should be able to vary their damping behaviors while converting part of the dissipated power into electricity. Therefore, an electric machine together with a suitable transmission system need to be integrated to the vehicle. Several types of solutions have been investigated during the last two decades. In the present thesis, one prototype of regenerative damper with controllable damping and energy harvesting features is developed. The regenerative shock absorber employs the electro-hydrostatic actuation principle, uses a hydraulic actuator directly interfaced with a motor-pump group by means of hydraulic circuit to convert the linear motion of the piston into rotation. To maximize the energy regeneration as well as to guarantee the damping features, the hydraulic, mechanical and electric subsystems must be integrated and optimized as an entire system. The thesis establishes a system-level approach during the design phase while complying with important constraints such as envelop volume and supply voltage limitation. Different aspects that will affect the final conversion efficiency are analyzed individually, a prototype is also produced and fully characterized with experimental tests. Furthermore, this approach can be extended to any motor-pump unit for hydraulic regenerative dampers. The significance of the present work can be seen also from its integration with the electric powertrain. Since the shock absorber is electrical, it can easily transfer the power to the vehicle battery which is also electrical, in this case, a single system can be used to handle the energy. Another important aspect is about the autonomous driving technology, since systems and devices nowadays are getting towards having more controlled damping properties to enhance the driving comfort experience.

Contents

List of Figures

List of Tables

Nomenclature

Roman Symbols

A_p	piston cross section
V_g	volumetric displacement
Q_g	input flow rate
ΔP_g	input pressure drop
T_m	electromagnetic torque
T_ro	radial viscous drag torque
T_a	axial viscous drag torque
V_dc	DC bus voltage
I_dc	DC bus current
c_p	linear damping coefficient
F_p	piston/damping force
v_p	piston/damping speed
K_t	torque constant
K_e	back-EMF constant
R	phase resistance
R_ext	external impedance
R_1o	outer gear outside radius
R_1l	outer gear lobe radius
R_1r	outer gear root radius
R_2o	inner gear outside radius
R_2i	inner gear inside radius
l_g	gear axial length
e_g	gear eccentricity
g_t	inter-teeth clearance
N_g	number of inner gear teeth
V_j	volume of the jth chamber
f_v	chamber volume function
θ_g	pump shaft angular position
f_a	axial viscous drag function
J_cyl	cylinder moment of inertia
l_cyl	cylinder length
$R_\mathrm{cyl,o}$	cylinder outside radius
$R_\mathrm{cyl,i}$	cylinder inside radius
$R_\mathrm{p,o}$	port outside radius

$R_{p,i}$	port inside radius
$R_{cyl,o}$	cylinder outside radius
d_p	minimum distance between ports
g_i	inside diameter clearance
g_o	outside diameter clearance
g_a	axial clearance
D_s	shaft diameter
D_p	pocket diameter
l_p	pocket depth
c_{sc}	maximum rotary damping coefficient
p	number of pole pairs
N_c	number of coils
N_t	number of turns per coil
A_s	slot cross section
K_λ	PM flux per unit length
l_m	active length
l_{et}	end-turn length
A_w	wire cross section
K_{cp}	coil packing factor
$P_{m,avg}$	average power loss
c_{ref}	linear damping reference
P_g	harvested power
d	direct axis
q	quadrature axis

Greek Symbols

η_e	electrical efficiency
η_{hm}	hydro-mechanical efficiency
η_t	total conversion efficiency
η_v	volumetric efficiency
η_g	pump total efficiency
Ω_g	angular speed
τ	electrohydrostatic transmission ratio
α_t	teeth aspect ratio
α_{g1}	outer gear aspect ratio
α_{g2}	inner gear aspect ratio
δ_g	pulsation index
γ_p	port opening angle
ρ_{cyl}	cylinder mass density
μ_f	dynamic viscosity
λ_p	PM flux linkage amplitude
ρ_{Cu}	copper resistivity
Θ_0	initial temperature
Θ_c	winding temperature
Θ_p	PM temperature

Other Symbols

$\mathscr{A}_z$ magnetic vector potential z component

$\mathscr{F}_j$ emptying rate function of the jth chamber

Acronyms / Abbreviations

ICE Internal Combustion Engine

HEV Hybrid Electric Vehicle

PLDV Passenger Light Duty Vehicle

RDE Real Driving Emission

RSA Regenerative Shock Absorber

EHA Electro-Hydrostatic Actuation

MMR Mechanical Motion Rectifier

HMR Hydraulic Motion Rectifier

GA Genetic Algorithm

AC Alternating Current

DC Direct Current

BLDC Brushless DC electric

EMF Electromotive Force

BEMF Back Electromotive Force

PSD Power Spectral Density

NEDC New European Driving Cycle

SOC State of Charge

CFD Computational Fluid Dynamics

FEA Finite Element Analysis

RMS Root Mean Square

PM Permanent Magnet

LPTN Lumped Parameter Thermal Network

PI Proportional Integral

ECU Electronic Control Unit

DOF Degree of Freedom

MPPM Multi-purpose Power Module

Chapter 1

Introduction

1.1 Motivation

By considering an energy outlook scenario which is in line with Kyoto and Copenhagen (450 Scenario) as shown in Fig.1.1 [1], IEA estimates for 2035 shows that:

- More than 80% of PLDV sales will have on-board ICEs (Internal Combustion Engines).
- Most of these ICEs will be high-efficient and flex fuels (capable of running with alternative fuels, biofules, synthesis fuels,etc).
- More than 2/3 of these ICEs will be integrated in hybrid powertrain of the thermal-electric type (HEVs).

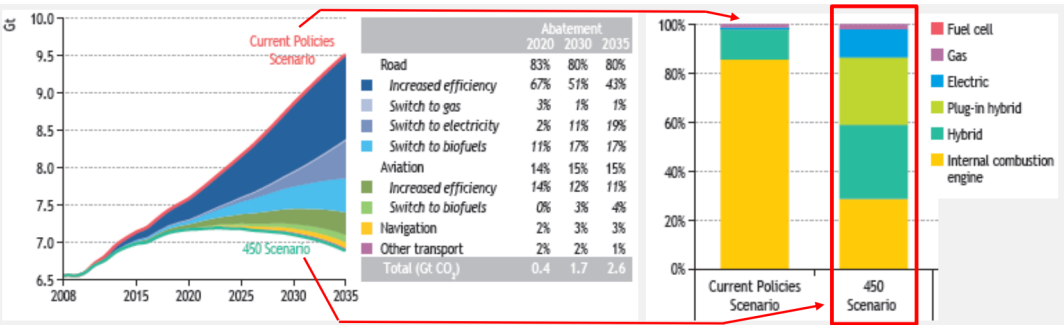

Fig. 1.1 IEA, WEO 2010, 450 Scenario [1]

Air pollution is the effect caused by concentrations of solids, liquids or gases in the air that have a negative impact on the surrounding environment and people.

Primary pollutants are those emitted directly as a result of human activity or natural processes, while secondary pollutants are created from primary pollutants, sunlight and components in the atmosphere reacting with one another.

Examples of primary air pollutants from combustion systems are:

- Generated by incomplete and non-ideal combustion process: CO, HC, NOx, PM
- Derived by additives or other chemical species present in the fuel: SOx, metal compounds (such as salt of Pb in old gasoline fuel)
- Derived from lubricant oil (aerosol of lubricant oil) or material coming from wear of machine components

Non-combustion emissions are also relevant. They consist of process emissions in industry and non-exhaust emissions in transport. Process emissions in industry relate to the formation of emitted compounds from non-combustion chemical syntheses or dust production, and stem from activities such as iron and steel, aluminum paper and brick production, mining and chemical and petrochemical production. Non-exhaust emissions are very significant in transport, relating to emissions from the abrasion and corrosion of vehicle parts (e.g. tyres, brakes) and road surfaces, and are (in many cases) still relevant for those vehicles that have no exhaust emissions.

Main secondary air pollutants includes ground-level ozone, photochemical smog, and acid rains (acid deposition). Manmade industrial chemicals (CFC) and pollutants (NOx) can also deplete the ozone layer in the stratospheric ozone (so called "ozone hole").

Fig.1.2 shows the statistical data about NOx emissions all around the world [2], from which it is clear to see that China and U.S are the most polluted regions and nearly 40% of the NOx emissions are coming from the transport system.

The air pollution mentioned above can significantly affect the human health (e.g. heart and lung diseases), it also can cause the acidification and eutrophication of water and soil, crop damage, climate change (both warming and cooling effects), damage to cultural sites and biodiversity and reduced visibility.

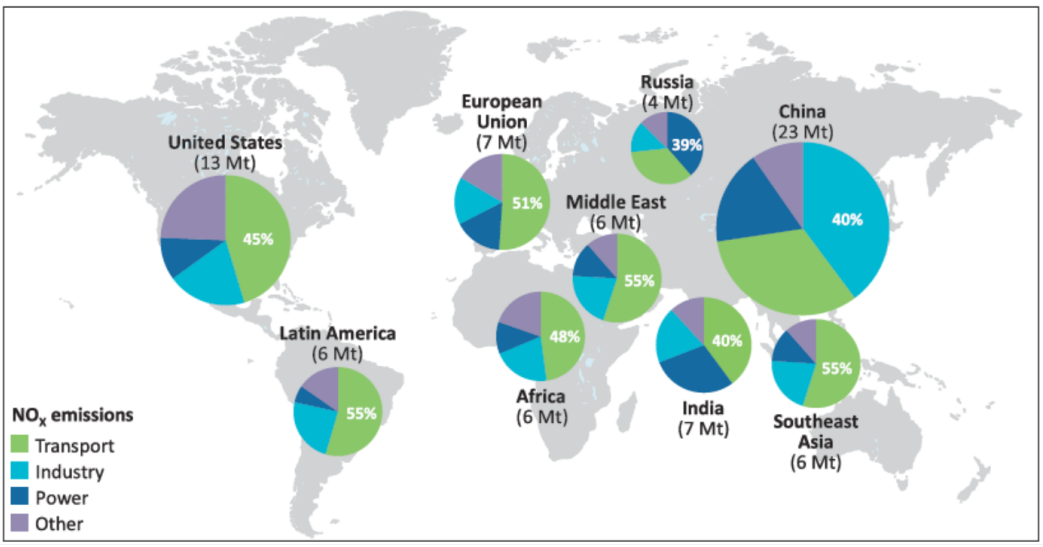

Fig. 1.2 Energy related NOx emissions around the world in 2015 [2]

However, the European Union (EU) has also established some regulatory frameworks regarding the emissions for road vehicles. According to document NO.443/2009 [3], for reducing CO_2 emissions for passenger vehicles as shown in Fig.1.3, the fleet average to be achieved by all cars registered in the EU is 130g CO_2/km. From the year 2020, this value should be reduced to 95 g/km, and from 2025, CO_2 fleet average should be further reduced to 68-78g CO_2/km. Furthermore, starting from 2019 there is also an excess emissions premium which is 95 Euro per each exceeding g CO_2/km for each sold vehicle.

Document NO.715/2007 established the pollutant emission limits for passenger cars (CO, HC, NOx, PM, PN). It sets emission standards for vehicle type-approval and different emission targets for vehicle running on SI/CI ICEs, Real Driving Emissions (RDE) testing requirements are being phased-in between 2017 and 2021 to control vehicle emissions in real operation, outside of the laboratory emission test.

However, this critical environment issue together with the strict regulations on vehicle emissions motivate the research to improve the energy efficiency in all the vehicle subsystems. Among these, the vehicle suspension is no exception. It is well known that this subsystem plays a key role in filtering the road irregularities in order to guarantee the comfort and safety features of driving. The conventional shock absorber systems dissipate the kinetic energy coming from the road unevenness into wasted heat. Nevertheless, recent research efforts have addressed the possibility of

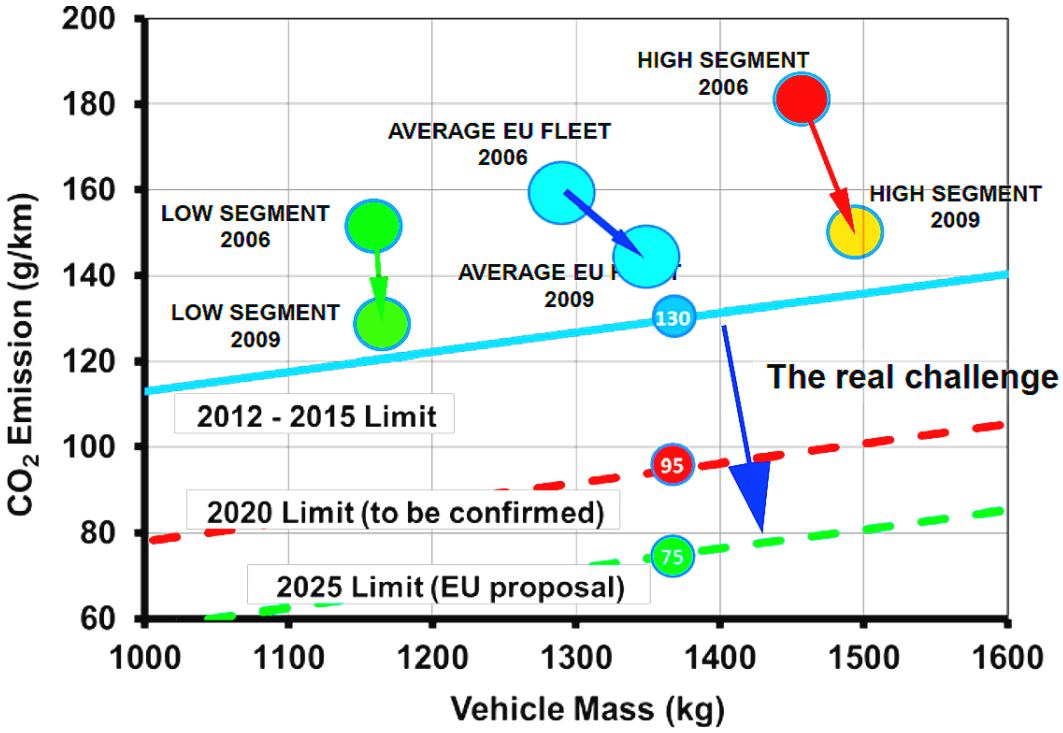

Fig. 1.3 EU NO.443/2009 for reducing CO_2 emissions for passenger vehicles [3]

implementing regenerative shock absorber (RSA) devices This kind of suspension is able to vary its damping behavior while converting part of the otherwise-dissipated power into electricity. This technology exploits the intrinsic reversibility of electric machines and a suitable transmission system for the integration into vehicles.

Among the available solutions to address the problem of regenerating energy, shock absorbers equipped with electro-hydrostatic actuation (EHA) systems seem to be a promising method compared with other alternatives in terms of power density, reliability and flexibility. By adopting this solution, the regenerating capability is heavily influenced by the motor-pump unit which is the core element of the system. To maximize the energy regeneration, hydraulic, mechanical and electric subsystems must be integrated and optimized together while preserving the damping functionality. Nevertheless, the state of the art does not offer clear guidelines on the design of this motor-pump group as a whole.

1.2 Aim of the Work

The aim of the present dissertation is to design and characterize a regenerative shock absorber implementing the electro-hydrostatic solution in automotive field. In order to achieve this objective and maximize the energy harvesting capability, the design process follows a system-level approach that investigates the role of different design aspects in order to understand which is the most critical requirement through the design, production and testing phase. Prototypes will be assembled and installed on the four corners of a testing vehicle. Furthermore, in order to provide full-active functionality, a power stage with a three-phase bridge is also adopted. A fully characterization process will be provided including static, dynamic and real road testing. The aim is to validate the design from energy recovery point of view. Although the design and characterization are based on the development of particular prototypes, the followed approach can be extended to any motor-pump unit for hydraulic regenerative dampers.

The significance of this project is that integration with the electric powertrain. since the shock absorber is electrical, it can easily transfer the power to the battery of the car which is also electric, so there is a single system can handle the energy.

1.3 State of the Art

As mentioned earlier in the motivation part, the environmental problem due to CO_2 emissions is getting more severe over the past decades. And it is already known that a large portion of the pollutant is coming from the transportation system. To solve this critical issue, in recent years, one of the main targets in automotive field is to increase the vehicle efficiency.

In these efforts, research and development has been focusing not only on the ICE, but also on other vehicle subsystems. In many cases, the goal is to recover energy from inevitable energy sinks [24]. For example the recuperation of the dissipated kinetic energy through friction brakes is well investigated by researchers. In addition to recover the energy from friction brakes, another approach which is getting more popular is recuperation from the vehicle shock absorbers because of its high-energy conversion efficiency, design simplicity, quick response, strong controllability and capability in energy recovery [25, 26], for example, the GenShock

made by ClearMotion. These regenerative dampers can convert the linear movement of the suspension into electricity through an electromagnetic circuit.

In recent years, many researchers have made their efforts in the field of regenerative shock absorbers. Studies and researches regarding active [27–41] and semi-active [42–52] suspensions are well investigated from different aspects such as design methodology [31, 38, 50, 52–54], control strategy [33, 36, 37, 42, 43, 46, 47, 49, 51, 55], and simulation techniques [34, 44, 45]. While there are also some other works focused other aspects for example the damper dynamic behavior [56], design optimization process [57–59] and experimental validation [60].

Furthermore, the potential energy that can be recovered from vehicle shock absorbers are investigated in [24, 61], while the main performance of the vehicle considering its ride comfort and harshness are also addressed in the works [58, 62].

Regenerative shock absorber system can be realized in different ways and based on how the linear vibrations are translated into electricity, usually it can be categorized into linear electromagnetic harvesters (direct energy harvesters) and rotary electromagnetic harvesters (indirect energy harvesters). Both the linear and rotary electromagnetic based regenerative suspensions with their configurations and working principles will be investigated in the following parts. At the end of this section, a comparison of different studies conducted on energy harvesting shock absorbers is also addressed.

1.3.1 Linear Regenerative Shock Absorber

Karnopp's research [4] was the first to examine the feasibility of using a permanent-magnet linear motor with variable resistors to substitute the conventional dampers.

Different from the rotary based solution which depends on a transmission system to provide the rotary generator with a unidirectional motion, the linear regenerative shock absorber transforms the kinetic energy of the suspension directly into electricity by electromagnetic induction. In this regard, the linear solution can offer a high capacity of the regenerated power due to the lack of power losses by the transmissions.

Figure1.4 shows the scheme of a generic voice coil which can be considered as a typical type of linear motion actuator. We assume that the magnets generate a

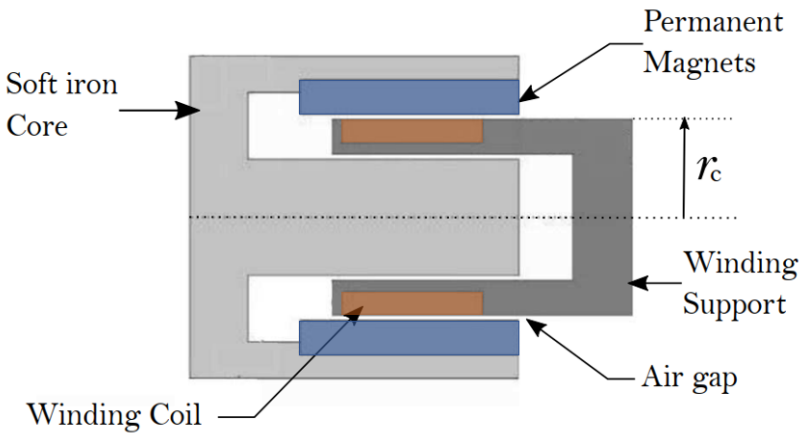

Fig. 1.4 Scheme of voice coil linear actuator.

uniform field with a flux density B in space. The coil has a cylindrical geometry with radius r_c, it carries a current flow i and consists of N turns of wires or conductors with a total resistance R. When the coil moves in the field with a speed v_c perpendicular to the field. By applying Faraday's law and Biot-Savart's Law, the induced voltage E and the magnetic force F on the conductors can be expressed by:

$$E = Blv_c \tag{1.1}$$

$$F = Bli \tag{1.2}$$

where l indicates the total length of the wire and can be expressed as:

$$l = 2\pi r_c N \tag{1.3}$$

If an external resistance R_{ext} is connected to the coil, it becomes a linear mechanical damper. The damping coefficient is varied when R_{ext} varies. Furthermore, the current is related to the induced voltage, thus:

$$E = (R + R_{ext})i \tag{1.4}$$

by combining Eq.1.1, Eq.1.2 and Eq.1.4, the force F can be rewritten as:

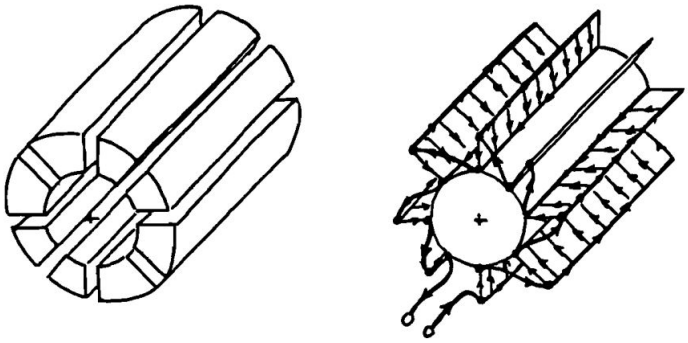

Fig. 1.5 Magnetic Circuit and Armature with Conducting Grids as Radial Fins shown in [4].

$$F = \frac{B^2 l^2}{R + R_{\text{ext}}} v_{\text{c}} \tag{1.5}$$

from Eq.1.5 we can obtain the relationship between force and speed which is coherent with the definition of damping, and the equivalent damping coefficient c_{eq} can be defined as:

$$c_{\text{eq}} = \frac{B^2 l^2}{R + R_{\text{ext}}} \tag{1.6}$$

if the external resistance varies, the damping coefficient will also vary accordingly, and the coefficient reaches its maximum value when the coil is in short circuit ($R_{\text{ext}} = 0$).

Based on the this principle, Karnopp did the improvements to the conventional linear motion actuator as shown in Fig.1.5. This configuration consists only of magnets and air gaps, a toroidal path is used for the magnetic circuit rather than the electrical one, the current flows radially through the grids which are placed in the air gaps.

Compared with previous design, this configuration eliminates completely the iron core part which usually has a larger weight and therefore reduces the total mass.

There are many other research groups that continue to study this topic and during the first decade of this century, Gysen *et al.* [5] developed an active electromagnetic suspension that employs a brushless tubular permanent-magnet actuator to control the roll and pitch of the vehicle.

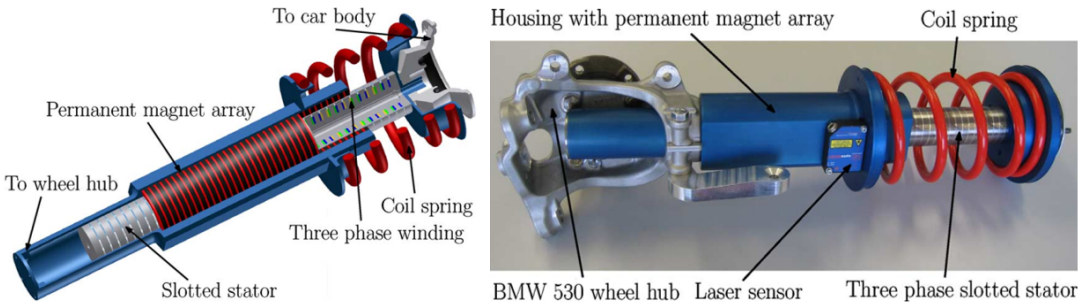

Fig. 1.6 Direct-drive electromagnetic active suspension system developed in [5]

The prototype they built can be seen in Fig.1.6, which is based on a conventional McPherson suspension, it consists of a passive coil spring that is used to support the sprung mass and a passive oil-filled damper which can still provide the damping features when needed. A direct-drive brushless tubular permanent-magnet actuator is placed in parallel with the damper to deliver active forces.

Suda *et al.* [63] developed an energy harvesting system with a linear DC motor based on an active suspension to achieve a good compromise between riding comfort performance and energy consumption. Zuo *et al.* [6] prototyped a linear motor based regenerative damper to convert the vibrational kinetic energy of the vehicle into electricity. Fig.1.7 shows the main structure of the proposed linear electromagnetic harvester with magnet assembly and the coil assembly separately. In the study conducted by Sapinski and Krupa [7], two linear motor structures were proposed as shown in Fig.1.8. Both structures were constructed with neodymium-boron magnet assemblies, ferromagnetic spacers and suitable coil windings.

Linear electromagnetic regenerative dampers are commonly used for active and semi-active suspensions due to their good controllability properties. Furthermore, the simple and reliable integration into most existing suspension layouts and lack of a transmission system makes the linear motors seem to be a straightforward choice for automotive industry. However, their limited force density make them work inefficiently and a substantial weight cannot be avoided and need to be added to the vehicle chassis, high production cost, and due to the relatively low vibration velocity, their size is still large. These shortcomings lead the research towards other solutions.

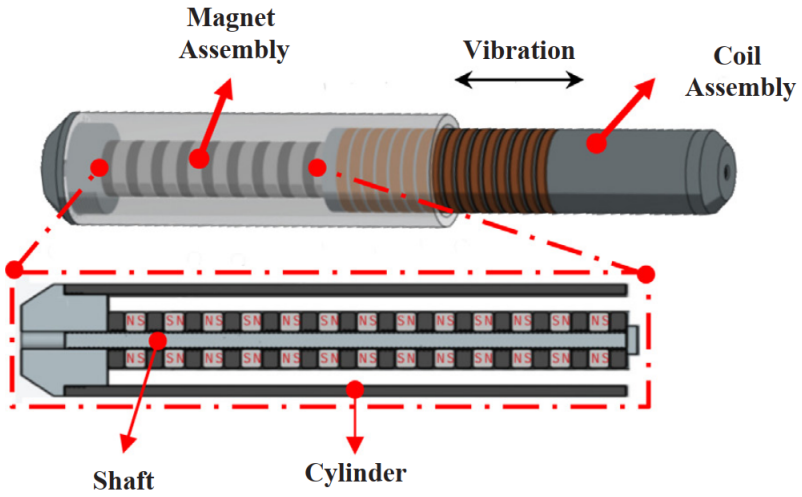

Fig. 1.7 Linear electromagnetic based energy harvesting shock absorber proposed in [6]

1.3.2 Rotary Regenerative Shock Absorber

In the work [64], the authors demonstrate that the power density of linear actuators, referred in literature as the damping-to-weight ratio, is limited and definitely outperformed by rotary electric motors.

When a rotary electric machine is going to be integrated into a conventional suspension, transmission systems are required in order to convert the linear motion coming from the ground into an angular displacement. There are mainly two common linear-to-rotary motion transmissions which are the electro-mechanical transmission based solution and the electro-hydraulic transmission based solution. and hydraulic method [16, 65, 17, 66, 67]. Different efforts have been devoted in order to find an optimal solution.

Electro-mechanical Solution

Because of its simple structure and high conversion efficiency, the electro-mechanical based rotary regenerative damper becomes one of the most common solutions among different energy harvesting structures. Furthermore,it can be categorized as rack-pinion [8, 9, 68–70], ball-screw [10, 11, 71–75], algebraic screw mechanism [76], pullies-cables assembly and other mechanical based systems [77]. Whereas, the rotating inertia of the transmission mechanism affected the suspension system, a

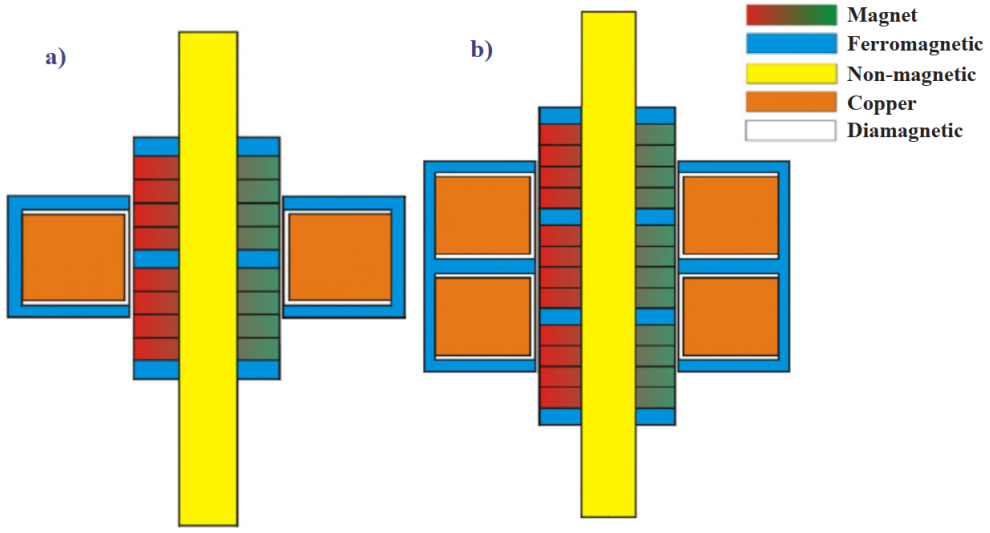

Fig. 1.8 Section view for two linear motor constructions proposed in [7]; (a) Structure with two neodymium-boron magnets and three ferromagnetic spacers assembly; (b) Structure with three neodymium-boron magnet systems and four ferromagnetic spacers assembly.

solution to this problem was proposed by adding extra dynamic elements in series with the rotating damper.

Zuo *et al.* [78] proposed a prototype of a harvesting damper which is based on rack and pinion mechanism that showed a relatively high energy density.

Li *et al.*[8] developed an energy harvesting shock absorber with both laboratory testing analysis and real road field test. As shown in Fig.1.9, when the damper is under compression or rebound, the linear motion on it will be translated into the rotation of the pinion gear due to rack-pinion coupling which can be further used to drive the electrical generator through a small differential with two perpendicular bevel gears. In [79], a total power conversion efficiency of about 56% for an excitation of 30 mm amplitude and 0.5 Hz vibration frequency was attained for a retrofit harvester based on the same rack-pinion mechanism.

In recent works [9, 70], Li *et al.* [9] proposed a mechanical motion rectifier attached with a rack-pinion damper as shown in Fig.1.10, this rectifier stage is introduced to attenuate inertial effects caused by the oscillatory vibration. The motion rectifier can be regarded as a mechanical diode, therefore, a regular unidirectional an-

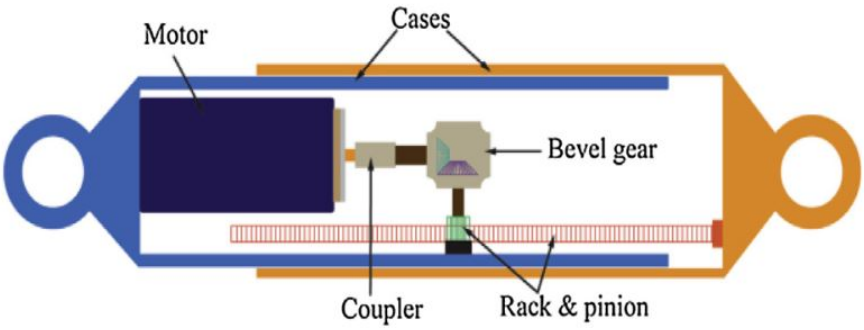

Fig. 1.9 Rack pinion mechanism layout in [8].

gular motion is guaranteed to enhance the system reliability and harvesting efficiency by decreasing the friction effectiveness.

Furthermore, this type of harvester is not only limited in automotive sector but also can be extended to other industry field. For example, based on the mechanical transmission of rack-pinion converter, Zhang *et al.* [80] developed a portable track vibration-based energy harvesting unit which can be considered as an alternative power source of a railway. Specifically, the motion is rectified using one-way bearings and an efficiency of about 55.5% was obtained.

Another common solution for this motion conversion is to implement ball-screw mechanism. Based on the rotating part which is attached to the rotor of the electric machine, this system can have different configurations: rotating screw [10] or rotating nut [11] as shown in Fig. 1.11. Compared with rack-pinion coupling, this alternative solution is able to reduce backlash [11]. Similarly, the motion rectifier has been also implemented in some works [74, 75] to allow the unidirectional rotary motion.

Fig.1.12 shows the structure of the harvester prototype developed in [12], the input torque for the motor is created through a ball-screw assembled with a small ball nut and coupler.

Fig.1.13 shows an ball-screw based energy harvesting absorber which was proposed by Xie *et al.* [13, 81] to recover the kinetic energy dissipated and adjust the damping coefficient according to road conditions continuously.

Zhang *et al.* [82] proposed and validated experimentally a regenerative damper using a ball-screw transmission system. Due to the effect of high inertia moment of the ball-screw parts, the ride performance of the vehicle is related with the frequency excitations. A high frequencies excitation gave a poor ride behavior, while a good

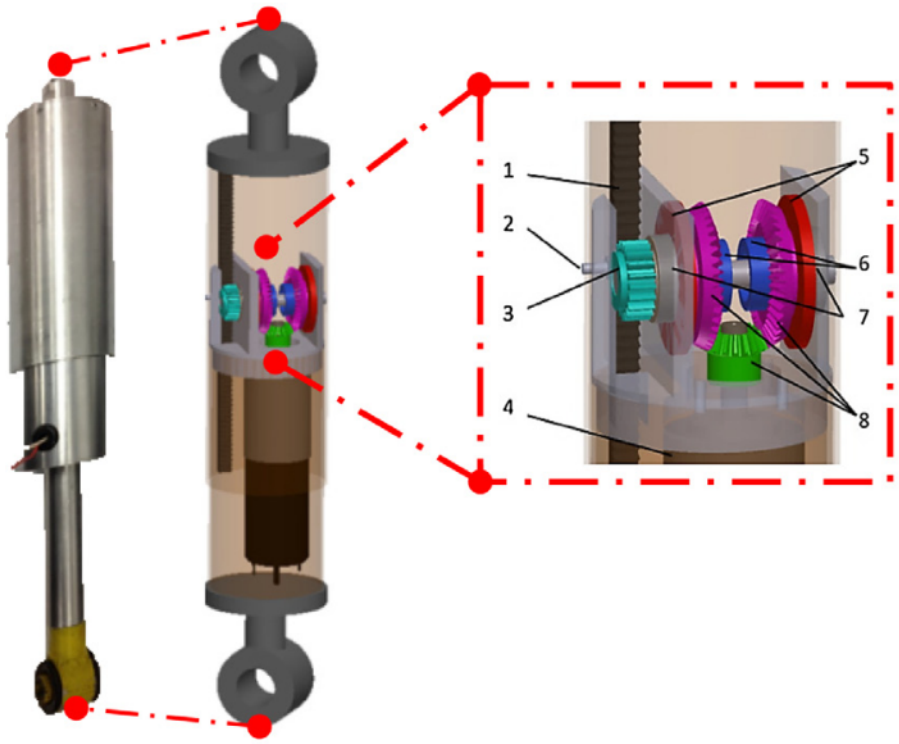

Fig. 1.10 Regenerative shock absorber based on rack-pinion mechanism with MMR proposed in [9]. Rack (1), Roller (2), Pinion (3), Ball bearings (4), Planetary gears and motor (5), Thrust bearing (6), Roller clutches (7), Bevel gears (8).

ride performance was achieved for low frequencies excitation. Similarly, in the work [83, 84], the authors patented a regenerative shock absorber with ball-screw mechanisms. However, bad ride comfort was found at high frequencies bandwidth.

To realize the linear-to-rotary transmission, apart from the common rack-pinion and ball-screw mechanism mentioned above, there are other possible alternatives. Fig.1.14 shows another regenerative damper which was based on a two-leg mechanism concept proposed by Maravandi and Moallem [14]. Although this prototype is capable of recovering energy with an average mechanical efficiency of 78%. However, from practical point of view, it is difficult to apply such solution in vehicle suspension to achieve the damping properties.

In [15], engineers from Audi AG. prototyped an electromechanical rotary damper called “eROT” based on a high-output 48-volt electrical system to replace the conventional hydraulic dampers in order to achieve a more comfortable ride. As shown in Fig. 1.15, the geometry of this new damper system is also well designed.

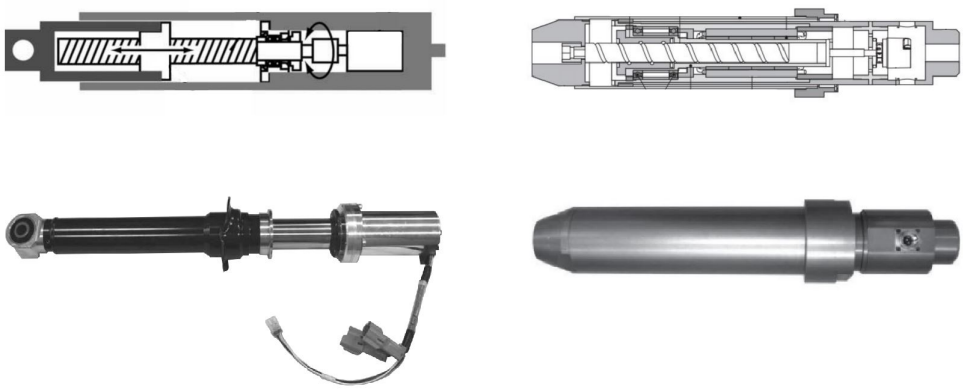

Fig. 1.11 Ball screw mechanism layout: rotating screw (left) in [10] and rotating nut (right) in [11].

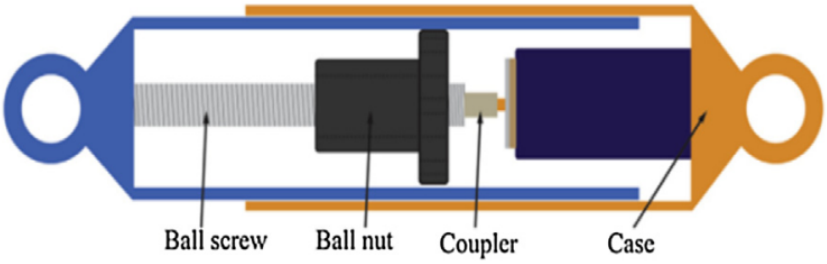

Fig. 1.12 Ball-screw energy regeneration mechanism proposed in [12].

The upright telescopic shock absorbers are replaced by the horizontally arranged electric motors in the rear axle area to save more space in the luggage compartment. As an actively suspension, eROT adapts ideally to irregularities in the road surface and eliminates the mutual dependence of the rebound and compression strokes that limits conventional hydraulic dampers. Besides the freely programmable damping characteristic, eROT can convert the kinetic energy during compression and rebound into electricity by using a lever arm. The force coming from the motion of the wheel carrier is transmitted by this lever arm to an electric motor through a series of gears.

Although the mechanical based harvesting system is promising, in a high-cycle task like vehicle damping, component wear and fatigue are more critical aspects compared to hydraulic based system. Another drawback is the poor controllability of the mechanical parts in the case of active or semi-active systems. In the further

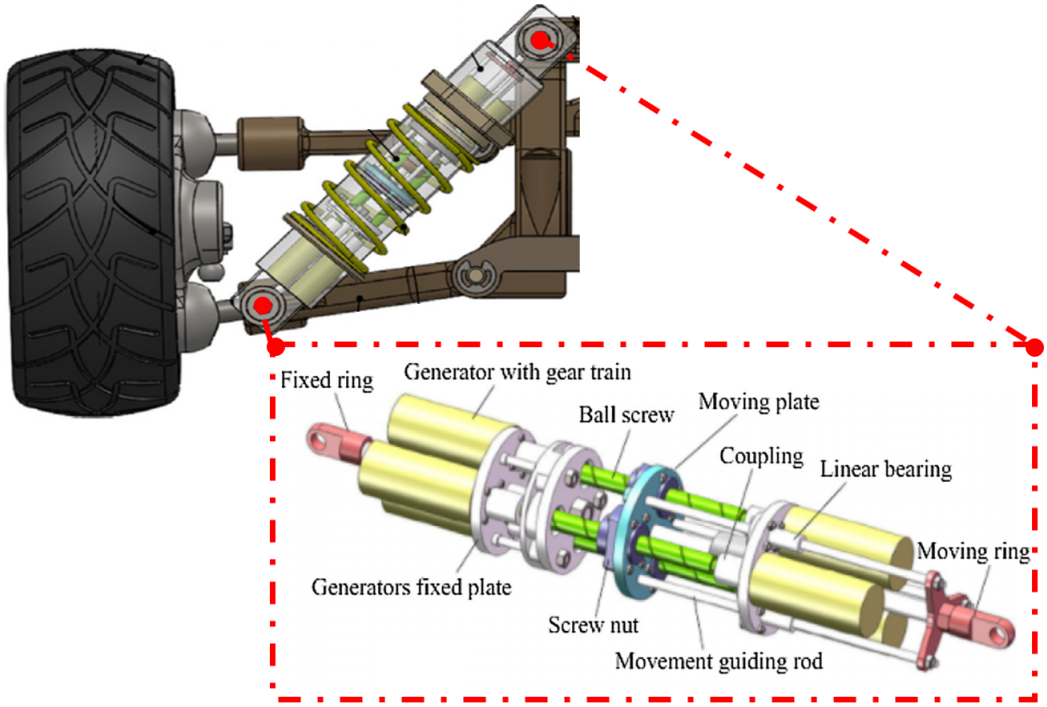

Fig. 1.13 3D model of the ball-screw transmission-based energy harvesting damper in suspension proposed in [13].

progress, possible solutions should be developed to overcome these drawbacks to achieve good durability, compactness and enhanced dynamics behavior.

Electro-hydrostatic Solution

Energy harvester based on hydraulic transmission or electro-hydrostatic actuation (EHA) system can be considered as one of the promising energy harvesting suspension systems. This type of damper depends mainly on the hydraulic fluid to transfer the linear displacement inside the cylinder to a rotational motion of an electric machine through a hydraulic pump/motor. Some other components such as gas accumulators and hydraulic check valves as motion rectifiers [85–87] are also present to achieve stability in the system.

Fig.1.16 shows the structure of a hydraulic based regenerative shock absorber with EHA system which is able to transform the motion from linear to rotary domain. Specifically, the system is directly interfaced with a motor-pump unit by means of a hydrostatic circuit. When there is a linear displacement, it produces a mechanical

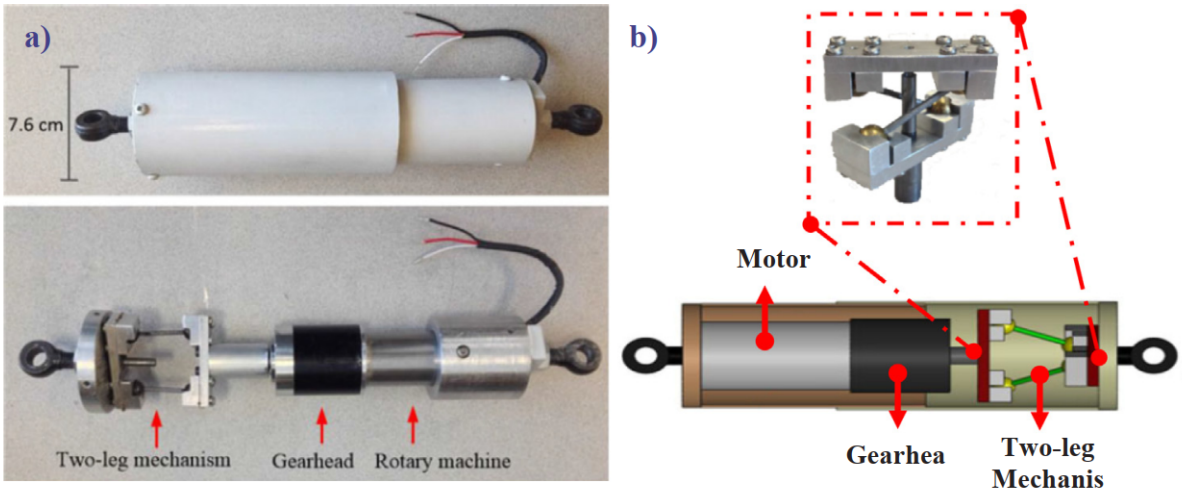

Fig. 1.14 Regenerative shock absorber based on the two-leg mechanism proposed in [14]; (a) prototype of the two-leg mechanism-based damper; (b) CAD assembly of the proposed prototype.

power which will be transformed by fluid into hydraulic power, and if the generated flow passes through a hydraulic pump, the power will be converted to mechanical domain in the form of rotary motion and then drives the electric machine.

Many recent works have addressed the design and implementation of this kind of dampers. Fang *et al.* [16] prototyped a hydraulic electromagnetic shock absorber with rectifier and internal accumulator in which the regeneration efficiency of the proposed system was 16% as shown in Fig.1.17. Li *et al.* [17] developed a hydraulic-based regenerative damper (Fig.1.18) and assessed its damping and regenerative capabilities with a hydraulic motion rectifier (HMR) depending on four sets of check valves to rectify the hydraulic motor direction of rotation. According to the experimental investigation in [17], the hydraulic regenerative suspension based on HMR offered a maximum conversion efficiency of 39% approximately for a defined harmonic excitation.

Zhang *et al.* [66] exploited the intrinsic fluid rectification of twin-tube shock absorbers to yield and validate a prototype and used the genetic algorithm (GA) optimization method to detect optimal regeneration power trends of a hydraulic pumping regenerative suspension with HMR, as a result, the obtained theoretical hydraulic efficiency was between 70 and 73%.

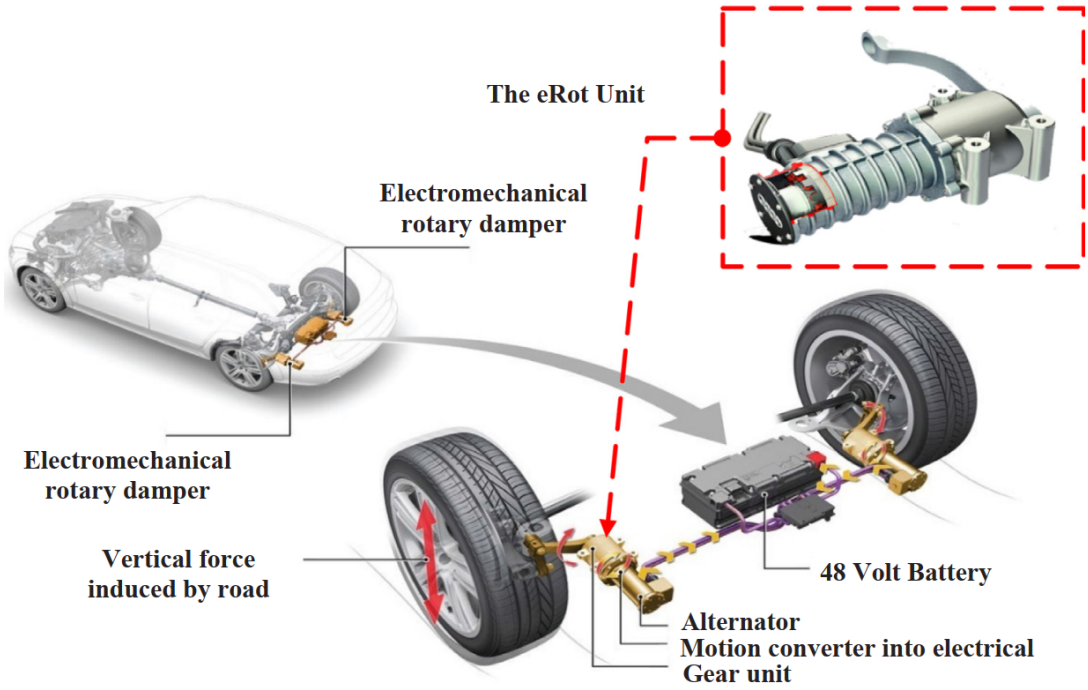

Fig. 1.15 The innovative eROT based on a horizontally arranged electromechanical rotary damper proposed by Audi in [15].

In the study [88], Demetgul *et al.* proposed a hybrid energy harvesting solution containing hydraulic and electromagnetic damper mechanisms to produce electricity from the linear motion. The concept of developing a hybrid energy harvesting suspension, combination of both direct and indirect drive energy harvesters, is a promising direction that can achieve the balance among all the energy harvesting mechanisms [89, 90].

According to [91], it has been conclusively shown that the hydraulic transmission based rotary electromagnetic harvesting damper could practically harvest a power of 310 W out of an input power of 840 W with a conversion ratio of 37% approximately. In [92], the authors prototyped a hydraulic electromagnetic shock absorber (HESA) combined with a horizontal linear generator which operated by a mechanical linkage mechanism. At last, the proposed system achieved a conversion ratio of about 20%. As the authors provided in [18], Fig.1.19 shows the expectations of the harvested energy based on a specific HESA prototype. It is obvious that such a harvesting function-based damper provides a high capacity of the regenerative power per damper

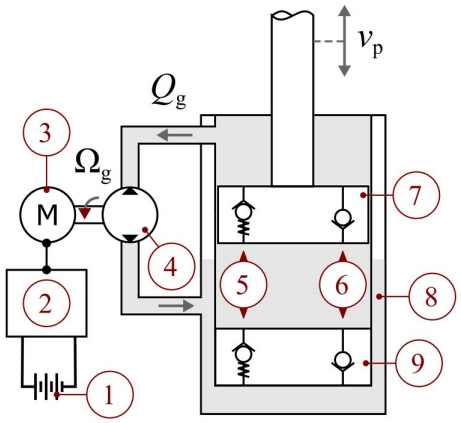

Fig. 1.16 EHA concept scheme: battery (1), power stage (2), electric motor (3), hydraulic pump (4), pressure-relief valves (5), check valves (6), piston (7), gas accumulator (8), base (9)

in the case of overloaded trucks and military vehicles owing to their bad driving circumstances.

However, ClearMotion Corp. (former Levant Power Corp.) has lead the development in this field with their fully controllable active energy-harvesting suspension called GenShock as shown in Fig.1.20. It is a commercial active suspension with vibration energy harvesting function considering a hydraulic-based transmission [93, 94]. The heart of the GenShock device is called Activalve which consists of a hydraulic pump and an electrical generator driven by an integrated electronic control unit. The Activalve is utilized to route and regulate the fluid inside a standard hydraulic absorber. Besides the energy harvesting purpose, the GenShock was proposed as a fully active suspension where an active force can be applied to push and pull the wheels leading to significantly enhanced ride comfort, handling and driving experience [95]. From the scientific point of view, they have also provided useful guidelines to optimize the hydraulic pump for constructing a regenerative damper [65].

Noticed that among the literature reviews, the research works usually focused on a single or few aspects, for instance, the improvement of efficiency from a specific point of view (either mechanical, hydraulic, or electrical), the implementation of control strategies, or the integration of components such as motion rectifiers.

As demonstrated in the following chapters for the hydraulic regenerative shock absorbers, the performance of the motor-pump unit directly influences the kinetic to

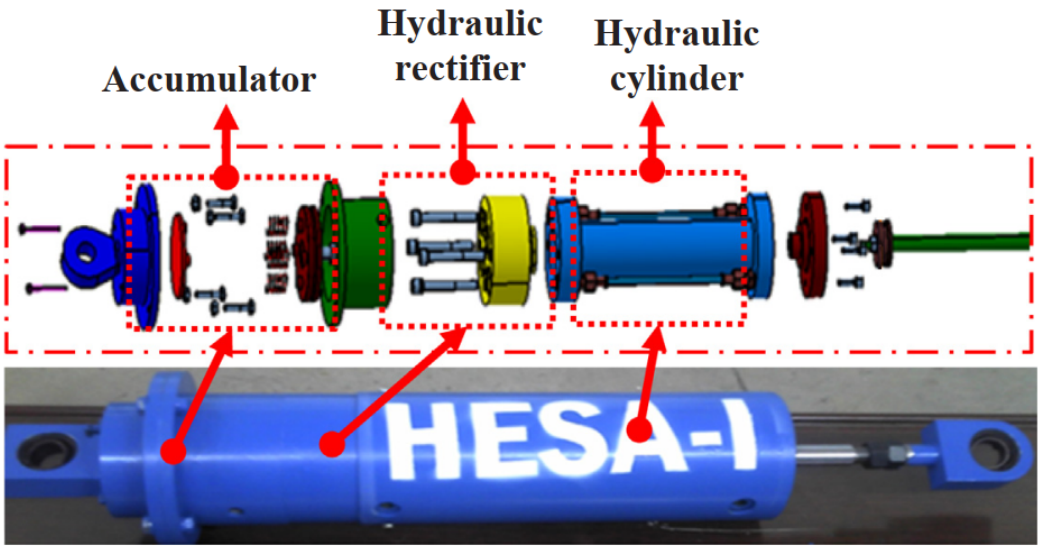

Fig. 1.17 Hydraulic harvesting absorber (HESA prototype) with HMR in [16]

electric energy conversion while there is very few works available in the previous literatures focused on the overall conversion efficiency and thus, this is the main target and topic of this dissertation.

Considering the advantages of hydraulic based regenerative dampers, since the fluid is used for the purpose of power transmission, the intrinsic lubrication of fluid-based solutions overcomes the main tribology concerns of electromechanical systems and offers better flexibility within the suspension. Furthermore, the studies [96, 97] have demonstrated that EHA systems are able to yield elevated actuation power without penalizing compactness and robustness. All these advantages motivate the choice of adopting EHA system for designing the regenerative shock absorber in the present thesis work. A complete comparison among different types of regenerative shock absorbers including their advantages and limitations will be summarized in next section.

1.3.3 Comparison of different energy conversion mechanisms

Comparison of the most popular energy harvesting systems in automotive suspension with their advantages and limitations are summarized below.

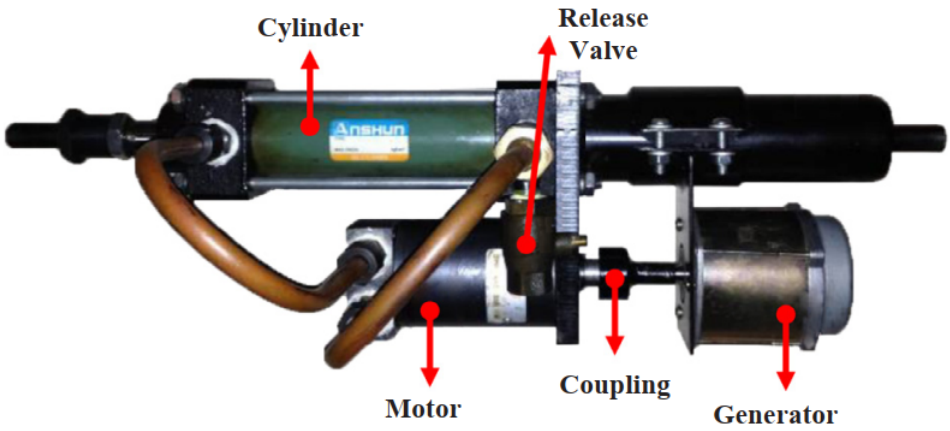

Fig. 1.18 Prototype of a hydraulic regenerative based shock absorber without HMR proposed in [17].

- **Linear regenerative shock absorber**
  Linear regenerative damper is used as a self-power controllable system which shows a simple structure and good reliability. It is easy to be fabricated, and more applicable to a real vehicle (easily integrated into most existing automotive suspensions) without any transmission mechanism, and it can get the power even for the small velocities. Therefore, this kind of harvesting damper is considered as the suitable choice for achieving good vehicle dynamics behavior as a semi-active or active suspension.

  However, because of the relatively low vibration velocity, the size of this type of damper is still large, and suffers from its low power density by using a linear motor. Moreover, to produce this harvesting damper, accurate system design and high production cost are also required. Furthermore, due to the continuous changing direction of the motor,a high inertia power loss is unavoidable and leading to a low conversion efficiency.

- **Rotary regenerative shock absorber based on rack-pinion mechanism**
  Rack-pinion transmission based rotary harvesting damper can achieve a high assembly accuracy with the ability of motion and force magnification. The stroke depends on the rack length. This type of damper has a considerable potential energy and power density, the energy conversion efficiency is high.

  However, by using rack-pinion transmission mechanism, the input and output axis are perpendicular to each other and this will lead to a large space designs

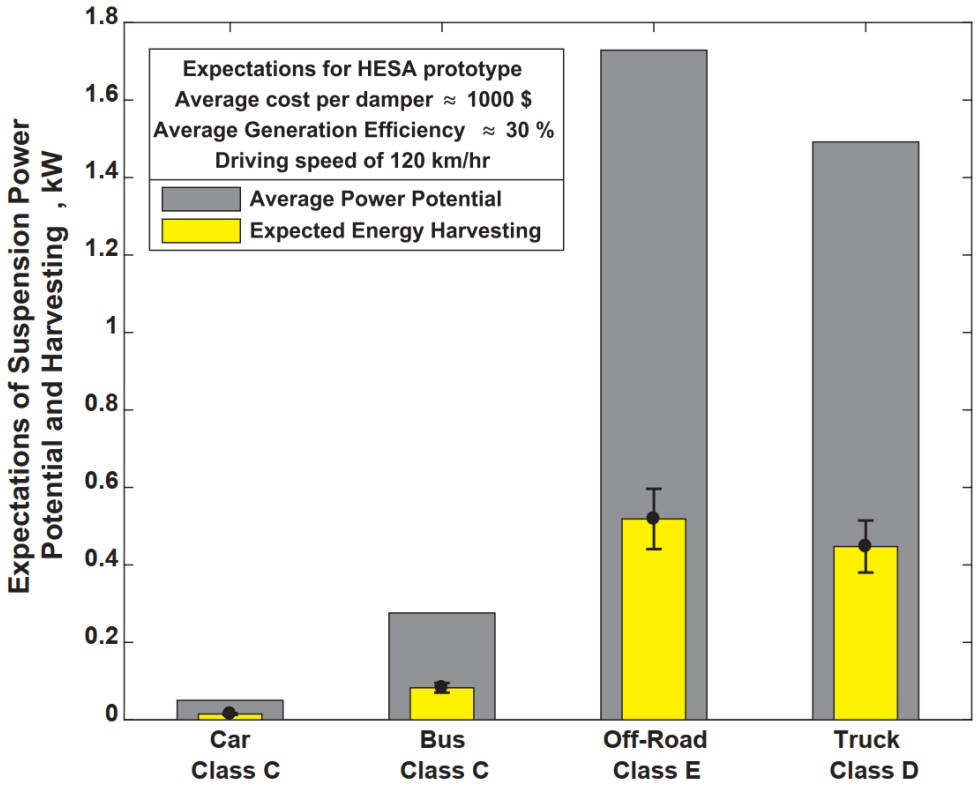

Fig. 1.19 Expectations of the energy harvesting with respect to the HESA prototype in [18].

and the torque transmission capability is limited by the gear module. Furthermore, due to the lubrication issue for the mechanical parts which could be also damaged easily, this kind of damper has a shorter operation life cycle while accurate system design is still required.

- **Rotary regenerative shock absorber based on ball-screw mechanism**
  Ball-screw transmission based rotary harvesting damper has a simple construction, it can operate smoothly with high positional accuracy and good durability comparing to rack-pinion solution. Moreover, it has a high mechanical efficiency with lower power consumption and losses, it could be also used for large-scale systems.

  Compared to the rack-pinion mechanism, ball-screw gives a relatively lower conversion efficiency but higher cost, there is also the risk of buckling in the region between supports and requires more parts for ball recirculating system.

Fig. 1.20 Old version (above) and latest version (below) of Genshock developed by ClearMotion Corp.

- **Rotary regenerative shock absorber based on hydraulic transmission**
  Hydraulic transmission based rotary harvesting damper adopts fluid as the media to achieve torque transmission purpose and leads to a high potential power and high-power density with high sensitivity for even small stroke changes, the system can be implemented for all the four suspensions of the vehicle with only one common power generation modulator, good controllability and durability properties makes it very effective in motion and force control. Comparing to other systems, due to the intrinsic lubrication properties of the fluid, this type of damper has the longest operation life cycle without any mechanical damage. Moreover, hydraulic based system can hold a large force and absorb impacts effectively, therefore, it can be used for large-scale energy harvesting systems, such as heavy duty vehicles.

  However, due to the presence of hydraulic loop, this system has a relatively higher power losses, oil leakage issues and usually the production cost is higher and the manufacturing process is complex.

From the comparison, it can be observed that the hydraulic-based system can satisfactorily provide an acceptable energy conversion performance for a full vehicle despite its high-power losses especially in case of heavy duty vehicles. The total power losses for an implemented hydraulic based harvesting system for a full vehicle (4-sets of suspension) can be suppressed in which one common power generation circuit could be recognized for all vehicle suspensions. In addition, using a controlled hydraulic suspension can improve significantly the vehicle dynamics due to its good controllability which facilitates the control of the displacement and the force using the hydraulic suspension. Therefore, the hydraulic transmission based electromagnetic rotary energy-harvesting suspension should be more investigated as a promising direction in terms of vibration energy-harvesting and vehicle dynamic behavior.

1.4 Thesis Outline

This thesis is divided into six chapters:

- **Chapter 1** briefly motivates and delimits the present work, includes a state-of-the-art research that covers available technology for regenerative shock absorbers.
- **Chapter 2** formally introduces the working principle of the system and provides the preliminary assessment of the suspension.
- **Chapter 3** describes the hydraulic pump design of prototypes.
- **Chapter 4** describes the electric motor design of prototypes.
- **Chapter 5** describes the integration of prototypes and explains the implemented control strategies.
- **Chapter 6** contains the experimental results of different tests that assess the performance of the prototypes.
- **Chapter 7** discusses the obtained results, states the conclusions and indicates possible future developments.

Chapter 2

Working Principle

2.1 Kinetic Energy to Electric Energy Conversion

In this Chapter, the conversion of kinetic energy to electricity by using shock absorbers is explained. As shown in Fig.2.1, the conventional damper of the suspension system is replaced by an energy harvester through which the electricity is produced and used for charging the battery.

In the last Chapter, we have already seen several types of regenerative shock absorbers by which the kinetic energy can be transferred into electricity. Here we can make a short and brief review:

- **Linear regenerative shock absorbers**

  This electromagnetic solution allows to produce Alternating Current (AC). The prototypes exhibited in [5] and [98] are made based on this concept.

- **Rotary regenerative shock absorbers based on mechanical transmission mechanism**

  The electromechanical solution usually adopts rack-pinion or ball-screw mechanism to transfer the kinetic energy to a bidirectional rotation and powers a generator to produces AC. In recent studies[9], a motion rectifier is also integrated to reach unidirectional movement. Furthermore, if a Direct Current (DC) generator is employed the output will be DC as well.

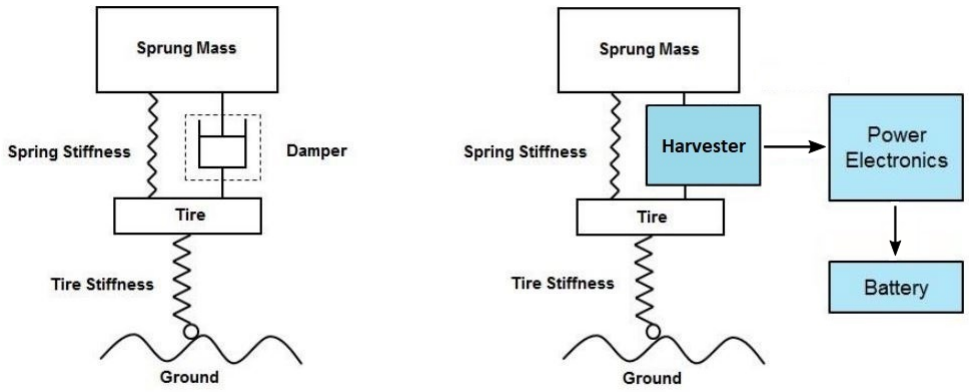

Fig. 2.1 Quarter car model for conventional vehicle suspension(left) and regenerative damper(right).

- **Rotary regenerative shock absorbers based on hydraulic transmission mechanism**

  For this type of solution, an hydraulic motion rectifier is used to convert the oscillatory vibration of the shock absorber into a unidirectional rotation and powers an electrical generator, which produces DC directly. For example, ClearMotion Corp. exploited this concept and developed their GenShock.

2.1.1 Road Profile Excitation

When a vehicle is running, there are several excitations which will be introduced to its suspension system. For example, the road irregularities, load transfers in longitudinal and lateral directions due to different maneuvers. Among which the road irregularities are considered to be the most critical disturbance for the driving comfort and handling because they continuously excite the vehicle suspension even if the car is moving straightly with a constant speed.

The purpose of vehicle shock absorber system is to filter the road irregularities and perform a good balance between ride comfort and road holding properties. To do this, the conventional dampers usually dissipate the kinetic energy coming from the uneven road as wasted heat.

Since our target is to harvest energy from the dissipation, it is important to figure out the amount of kinetic energy that can be dissipated or in other words regenerated by the shock absorber. It is straight forward that the vehicle suspension will dissipate more energy if passing through a rougher surface. Vehicle speed is considered as another factor which will affect the amount of dissipated energy, a higher vehicle speed makes the shock absorber dissipate more energy. Therefore, the unevenness of the road together with the speed represent the source of the excitation for the vehicle.

As the only interface between the road and vehicle, the behavior of tires can also affect the kinetic energy dissipation, they determine the entity of dynamic vertical forces which are transmitted by the road to the vehicle body, the stiffer the tires, the more the energy dissipated by the shock absorbers.

Other parameters like masses (both sprung mass and unsprung mass) and suspension characteristics (spring stiffness and damping coefficient) can be neglected in determining the energy dissipated by the shock absorbers. However, this assumption will be used in the following sections to calculate the CO_2 saving.

2.1.2 Regenerated Energy Storage

Once the harvested energy is obtained, one possible usage of the produced electricity is to charge the car battery. In this way, in theory the alternator does not have to produce that amount of electricity as it does for conventional vehicles equipped with Internal Combustion Engines (ICEs). For hybrid and pure electrical vehicles, this produced electricity could be used either to charge the low voltage battery (12V) or the high voltage traction batteries, the former condition is more common while the high voltage usage is quite rare.

For conventional ICE application, the harvested electricity will be used mainly for accessories and engine control unit, while in the case of hybrid or pure electric vehicles, it could be used for both accessories (usually through a DC/DC converter) and powertrain system. Furthermore, the current produced can be either alternate (AC) or direct (DC) depending on the particular conversion strategy adopted.

In the content of State of the Art (Section 1.3), it is shown that the linear harvesting dampers will generate less power and lower damping curves with respect to the other solutions, therefore, the linear type will not be further investigated in the following parts.

Whereas, for the rotary harvesting dampers, a further distinction can be made:

- Directly coupled with the electric machine (usually a reverse operated DC motor or an AC rectified generator).
- Connected with the electric machine (again a reverse operated DC motor or an AC rectified generator) through motion rectification (mechanical or hydraulic).

In the first condition, the regenerated electricity is AC type and therefore, the output current needs to be rectified, a relevant rectification efficiency must be taken into account considering the associated power losses, while in the second condition, by means of the mechanical or hydraulic motion rectifier, the electric machine is forced to perform unidirectional rotation and thus, the electrical rectification can be avoided. Furthermore, in [9], the authors also pointed out that this configuration is more efficient due to the unidirectional rotation can lead to a higher efficiency of the electric machine. For this reason, configuration with motion rectification is chosen to construct the prototype in present dissertation.

In any case, even if the output current is DC, a dedicated DC/DC converter is still needed to adapt the voltage level between the harvester output and the battery input. For example, a 92% efficiency is considered for this electrical-to-electrical conversion in [99].

Since the regenerative shock absorber is an electromechanical system, its damping effect can be obtained by setting the equivalent load resistance. As the system input, the mechanical power which can be regenerated by the shock absorber does not depend on its particular damping characteristic. Therefore, the mechanical power and the damping curve can be decoupled from each other. On the other hand, the overall conversion efficiency is needed in order to obtain the output electrical power recovered from the mechanical power, and the overall conversion efficiency generally depends on the equivalent load resistance, as a result, the choice of a particular damping characteristic of the shock absorber determines the value of the overall conversion efficiency and, thus, influences the amount of electrical power that can be produced.

Being the equivalent load resistance determined by the desired damping characteristic of the shock absorber, it is not possible to rely on it to maximize the overall conversion efficiency. This equivalent resistance is modulated in order to obtain

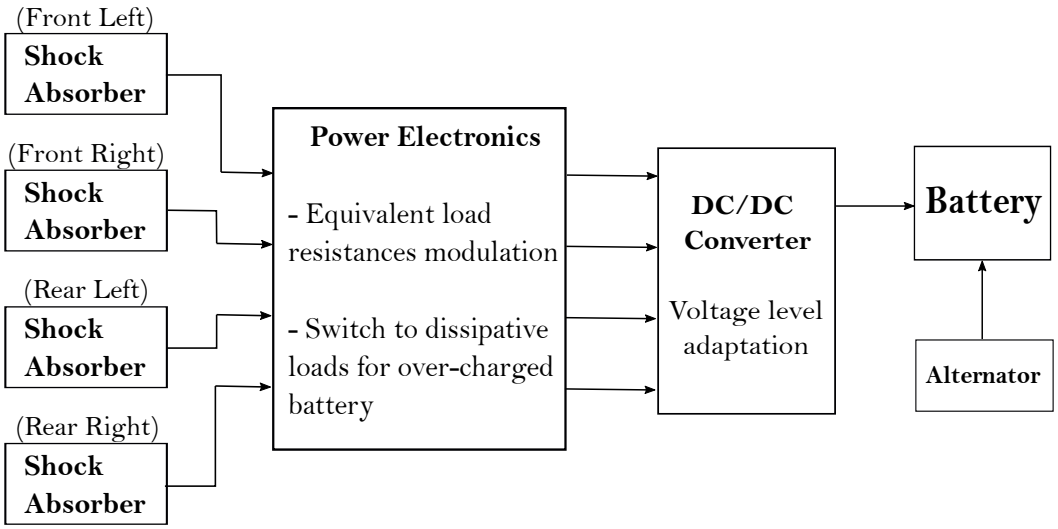

Fig. 2.2 Integration of the current from shock absorbers in the electric grid of the vehicle.

the required damping characteristic and the overall conversion efficiency must be calculated for each possible operating point.

The integration of the current from the shock absorbers to the electric grid of the vehicle is represented in Fig.2.2. During the charging phase of the battery, priority is always given to the power coming from the shock absorbers. This is possible due to the fact that when the charge level of the battery exceeds a certain threshold, the alternator which has a voltage regulator stops charging the battery and only the power coming from the shock absorbers remains.

In case of the battery is over-charged, a resistive load (dissipative) which is driven by the power electronics will perform the damping action when there is still an extra amount of energy from the shock absorbers. Obviously this is a very particular condition and no energy will be harvested in this rare situation.

2.2 System Overview

2.2.1 Hydraulic RSA modeling

Figure 2.3 represents a complete model of the hydraulic regenerative shock absorber system. It exploits an electro-hydrostatic transmission to transfer the mechanical power between the linear and rotary domains. As shown in the figure, the system

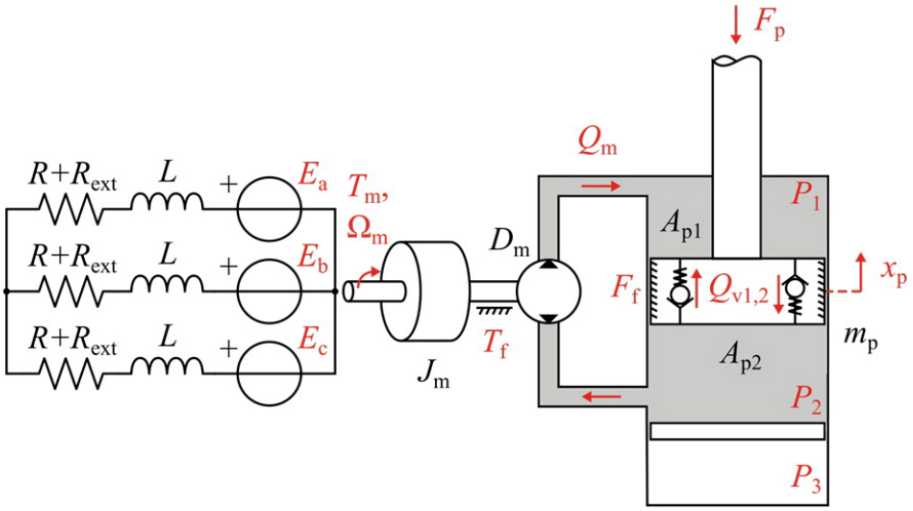

Fig. 2.3 Hydraulic regenerative shock absorber model scheme.

consists of three parts: an electric machine, a hydraulic pump, and a linear hydraulic actuator. The electric machine is rigidly coupled with the fixed displacement hydraulic pump, the pump and the linear hydraulic actuator are connected by means of two pipelines. Hence, when the piston makes a linear movement, it will generate a fluid flow inside the hydraulic circuit and subsequently, it will be converted to a rotation on the shaft of the electric machine to generate electricity that stored in the battery.

Specifically, the electric machine is a three-phase brushless permanent-magnet motor, since its elevated power-to-weight ratio favors design compactness. Assuming a perfectly balanced winding layout, the phase impedance is characterized by the winding resistance R, shunt or load resistance R_{ext}, and winding inductance L. Mutual inductance contributions between phases are also present. The motor back electromotive force (EMF) constant K_m is given by

$$K_m = \frac{|E_{a,b,c}|}{\Omega_m} \tag{2.1}$$

where $E_{a,b,c}$ represents any of the phase back EMF waveform, and Ω_m indicates the mechanical angular speed of the rotor.

The dynamic behavior of the motor can be represented in a two-phase rotating reference frame. This transformation simplifies mutual inductance terms and reduces the order of the resulting differential equation system.

$$(R+R_{\text{ext}})i_{\text{q}}+L_{\text{q}}\frac{\text{d}i_{\text{q}}}{\text{d}t}+p\Omega_{\text{m}}L_{\text{d}}i_{\text{d}}+K_{\text{m}}\Omega_{\text{m}}=0 \tag{2.2}$$

$$(R+R_{\text{ext}})i_{\text{d}}+L_{\text{d}}\frac{\text{d}i_{d}}{\text{d}t}-p\Omega_{\text{m}}L_{\text{q}}i_{\text{q}}=0 \tag{2.3}$$

$$T_{\text{m}}=\frac{3}{2}[K_{\text{m}}i_{\text{q}}+p(L_{\text{d}}-L_{\text{q}})i_{\text{d}}i_{\text{q}}] \tag{2.4}$$

Here, d and q subscripts denote direct and quadrature axis variables. Currents are indicated with the letter i, T_{m} represents the motor torque and p is the number of pole pairs of the electric machine. If the rotor is ideally isotropic, the inductances in both axes are equivalent:

$$L_{\text{d}}=L_{\text{q}}=\frac{3}{2}L \tag{2.5}$$

By substituting L_{d} and L_{q} in Eq.2.4, the reluctance torque term vanishes, thus, yielding a torque that depends only on the quadrature component of the current (i_{q}).

The implementation of Eq.2.2 to 2.4 is necessary to introduce the nonlinear dynamic behavior of the machine, which is highly dependent on its impedance terms [100]. From the mechanical point of view, the electric machine is rigidly coupled to the hydraulic pump gears, yielding a total moment of inertia J_{m}. Dissipative phenomena of both devices are represented as:

$$T_{\text{f}}=c_{\text{m}}\Omega_{\text{m}}+T_{\text{st}}\text{sign}(\Omega_{\text{m}}) \tag{2.6}$$

where c_{m} is a rotary viscous damping coefficient and T_{st} is the startup torque due to Coulomb friction.

The hydraulic pump is assumed as an ideal transformer between the mechanical and hydraulic domains:

$$T_{\mathrm{m}} = D_{\mathrm{m}} \Delta P_{\mathrm{m}} \tag{2.7}$$

$$Q_{\mathrm{m}} = D_{\mathrm{m}} \Omega_{\mathrm{m}} \tag{2.8}$$

where ΔP_{m} is the pressure differential across the pump with a fixed displacement D_{m}, and Q_{m} indicates the flow rate that is produced.

The hydraulic actuator is a two-chamber asymmetric cylinder with a gas-loaded accumulator for compensation. The evolution of the pressure in a generic hydraulic chamber is governed by a first-order differential equation:

$$\frac{\mathrm{d}}{\mathrm{d}t} P_{\mathrm{ch}} = \frac{\beta_{\mathrm{f}}}{V_{\mathrm{ch}}(x_{\mathrm{p}})} \sum_{j} Q_j \tag{2.9}$$

where β_{f} is the fluid bulk modulus, V_{ch} is the volume of the chamber and Q_j is the generic flow rate entering the chamber. Note that the volume V_{ch} and a flow rate component depend on the position of the piston x_{p} and its cross sections: A_{p1} during rebound and A_{p2} during compression.

The accumulator pressure can be found by solving:

$$P_{\mathrm{acc}} V_{\mathrm{acc}}^{\gamma} = P_0 V_0^{\gamma} \tag{2.10}$$

being P_{acc} and V_{acc} the pressure and volume of the accumulator at a given time, and P_0 and V_0 its preload pressure and the initial volume, respectively. The adiabatic constant γ is a property of the accumulator gas.

In the layout shown in Fig.2.3, the pressure P_1 can be approximated using Eq.2.10. Pressures P_2 and P_3 can be assumed equal and governed by the behavior of the accumulator (Eq.2.10), as its compliance dominates that of the oil. The stiffness of the hydraulic lines can be lumped into the stiffness of the hydraulic chambers. Furthermore, fluid inertial contributions are negligible due to the geometric dimensions of the hydraulic circuit.

The piston body is equipped with two check valves and two hydraulic orifices that limit pressure shocks during rebound and compression. The flow rate through the orifice element is defined as:

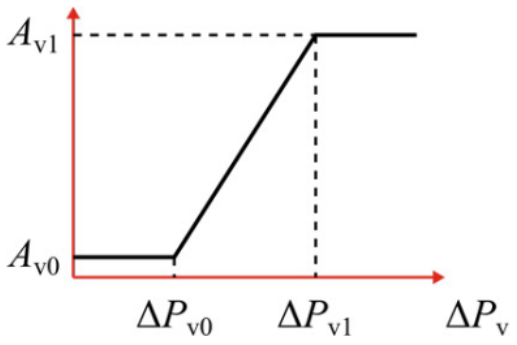

Fig. 2.4 Check valve aperture behavior. The valve cross section A_v depends on its pressure drop ΔP_v

$$Q_{or} = C_d A_{or} \sqrt{\frac{2}{\rho_f}} \frac{\Delta P_{or}}{(\Delta P_{or}^2 + \Delta P_{cr}^2)^{\frac{1}{4}}} \tag{2.11}$$

where C_d is the orifice discharge coefficient, A_{or} its cross section, ΔP_{or} its pressure drop and ρ_f the fluid density. Assuming circular orifices, the critical pressure drop ΔP_{cr} is given by

$$\Delta P_{cr} = \frac{\rho_f}{2} \left(\frac{\mathrm{Re}_{cr} \nu_f}{C_d d_h}\right)^2 \tag{2.12}$$

being Re_{cr} the critical Reynolds number that establishes the transition between laminar and turbulent flows, ν_f the fluid kinematic viscosity, and d_h the hydraulic diameter:

$$d_h = \sqrt{\frac{4A}{\pi}} \tag{2.13}$$

In a similar fashion, check valves present an orifice-like behavior with a variable cross section A_v that depends on the pressure drop across the valve ΔP_v (Fig.2.4). In particular, low pressure values lead to a negligible (leakage) cross section A_{v0}. A transition between the cracking pressure ΔP_{v0} and the maximum pressure ΔP_{v1} yields a linear growth of the valve cross section up to its maximum aperture area A_{v1}.

Finally, in the linear mechanical domain, the piston and rod are lumped into a mass m_p. Dissipative phenomena are described in a similar way to those in the rotary domain:

$$F_f = c_p v_p + F_{st} \mathrm{sign}(v_p) \tag{2.14}$$

where c_p is the linear viscous damping coefficient, F_{st} is the startup force due to Coulomb friction, and v_p represents the piston speed.

$$v_p = \frac{dx_p}{dt} \tag{2.15}$$

2.2.2 System Layout

Fig. 2.5 shows the configuration of the regenerated shock absorber proposed in present dissertation, the system exploits a conventional twin-tube shock absorber architecture connected to the hydraulic ports of a pump. During vehicle cruise, the piston of the shock absorber oscillates inside the tube at a speed v_p due to the ground irregularities. This motion leads to an oil flow rate Q_g that drives the hydraulic pump and therefore, the linear movement is transformed into a rotary motion Ω_g. Since the pump is mechanically coupled to an electric machine, a suitable control strategy of the latter device allows to modify the damping characteristic of the shock absorber. Furthermore, the electric motor acts as a generator in a portion of the damping quadrants. Hence, the system is also able to convert the kinetic energy of the suspension into electricity which can be stored in the battery.

In addition, the twin-tube architecture provides unidirectional motion of the motor-pump group. The fluid flow is rectified with the aperture of the base check valve during rebound and the piston check valve during compression. This working principle is already covered by previous research works [101, 102].

Considering its application, first of all, the designed regenerative device must act as a fully functional shock absorber, which means it must exhibit the required force-velocity characteristic to perform the desired damping action in order to achieve optimum comfort and vehicle dynamics. Moreover, the system must be easily adaptable to the activity of tuning on the road.

As shown in Fig. 2.5 (b), the prototype is fixed onto the shock absorber tube with a manifold. This approach yields a compact system and minimizes the introduction of losses due to hydraulic lines. Furthermore, it provides modularity because the motor-pump group unit can be installed on any shock absorber tube. For this reason, the optimization process of this single unit will be investigated in the following chapters disregarding the selected shock absorber architecture.

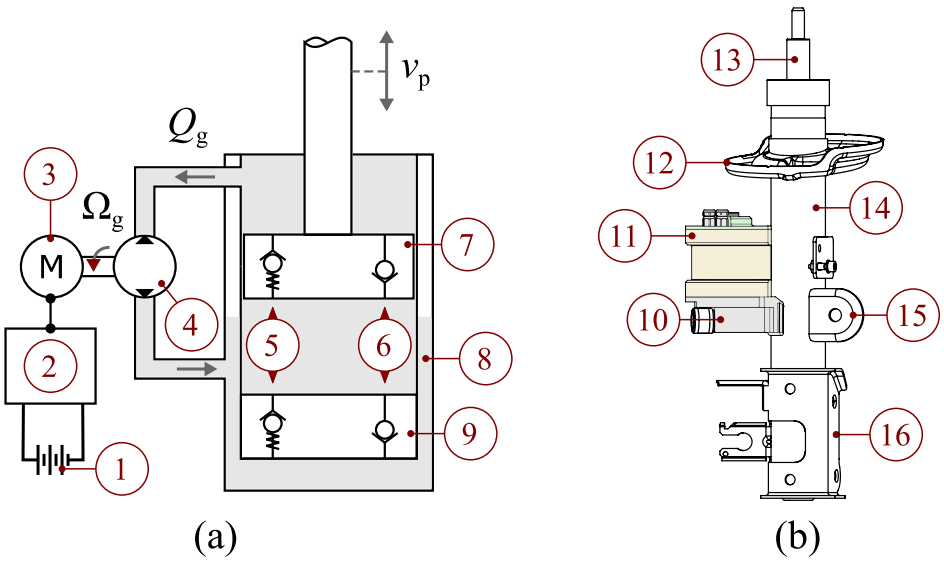

Fig. 2.5 Layout of a hydraulic regenerative shock absorber. *Concept scheme (a):* battery (1), power stage (2), electric motor (3), hydraulic pump (4), pressure-relief valves (5), check valves (6), piston (7), gas accumulator (8), base (9). *Prototype side view (b):* manifold (10), regenerative device (11), spring holder (12), rod (13), external tube (14), anti-roll bar bracket (15), wheel hub bracket (16).

In general, the power conversion from the hydraulic domain of the pump to the electrical domain of the battery is inevitably affected by a number of loss terms.

The hydraulic power applied to the pump is initially reduced by a volumetric loss due to internal leakages. The *volumetric efficiency* is given by

$$\eta_v = \frac{V_g \Omega_g}{Q_g}, \tag{2.16}$$

where Q_g is the flow rate across the pump, Ω_g its angular speed and V_g its fixed volumetric displacement.

Subsequently, a hydro-mechanical loss term considers the pressure/torque drop due to hydraulic minor losses and mechanical friction affecting the rotating elements. The *hydro-mechanical efficiency* associated to these phenomena is

$$\eta_{hm} = \frac{T_m}{V_g \Delta P_g}. \tag{2.17}$$

Here, T_m is the electromagnetic torque of the motor and ΔP_g the pump pressure drop.

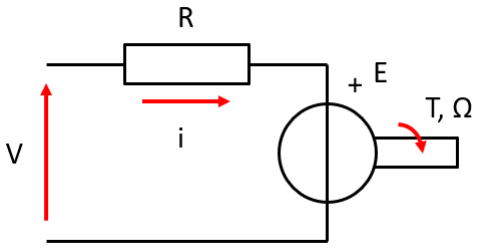

Fig. 2.6 Simplified motor model

Finally, a third loss term considers the conversion from the mechanical domain of the motor to the electrical domain of the battery, i.e.

$$\eta_{\mathrm{e}} = \frac{V_{\mathrm{dc}} I_{\mathrm{dc}}}{T_{\mathrm{m}} \Omega_{\mathrm{g}}}, \tag{2.18}$$

in which V_{dc} and I_{dc} define the voltage and current of the power stage DC bus, respectively. This *electrical efficiency* can be attributed to motor and power-stage losses.

The product of the three aforementioned terms yields the total conversion efficiency of the motor-pump unit:

$$\eta_{\mathrm{t}} = \eta_{\mathrm{v}} \eta_{\mathrm{hm}} \eta_{\mathrm{e}} = \frac{V_{\mathrm{dc}} I_{\mathrm{dc}}}{\Delta P_{\mathrm{g}} Q_{\mathrm{g}}}. \tag{2.19}$$

2.2.3 Controlled Damping Theory

In this section, the working principle of the electromagnetic damping control is demonstrated through a simplified motor model.

Fig.2.6 shows a simplified motor model, the sign convention of the model indicates that a positive current i rises when $V > E$, and this positive current will lead to a positive torque T, while the speed Ω is imposed externally.

Before going to detail, several assumptions are made:

- The motor is a DC motor.
- The system is in static conditions which means no inductances, and rotate with constant speed.

- Only the motor model is considered disregarding other mechanical parameters.
- An ideal power supply that can vary from $-V_{\mathrm{dc}}$ to V_{dc} is considered.

It is known that the DC motor can be represented in Bond Graph as a gyrator, therefore, the back electromotive force (BEMF) E can be written as:

$$E = K_{\mathrm{m}}\Omega \tag{2.20}$$

and the torque T is represented as:

$$T = K_{\mathrm{m}}i \tag{2.21}$$

where K_m is the motor constant.

According to Kirchhoff's voltage law (KVL), we can obtain that:

$$V = Ri + E \tag{2.22}$$

Eq.2.21 and Eq.2.22 yields:

$$T = \frac{K_{\mathrm{m}}}{R}(V - E) \tag{2.23}$$

furthermore, E can be substituted by Eq.2.20, thus we can obtain the torque-speed characteristic:

$$T = -\frac{K_{\mathrm{m}}^2}{R}\Omega + \frac{K_{\mathrm{m}}V}{R} \tag{2.24}$$

noticed here, by giving a command V, we can obtain the torque T as an output, while speed Ω is imposed externally as a disturbance.

Once we obtain the torque-speed characteristic, it can be represented in the four quadrants as shown in Fig.2.7.

When the speed and torque have the same sign, we consider it as a *Motor*, as shown in Fig.2.7 the light gray regions; while when the speed and torque have the opposite sign, we consider it as a *Damper*, as shown in Fig.2.7 the dark gray regions.

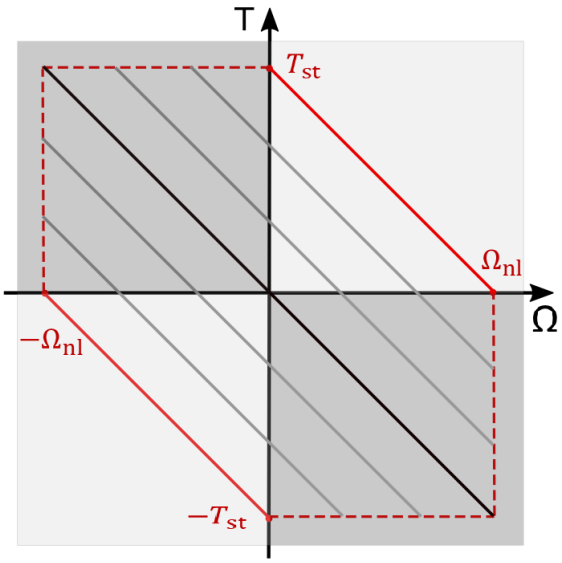

Fig. 2.7 Torque speed map

The maximum stall torque T_{st} is obtained at null speed when the motor is fed at maximum voltage V_{dc}:

$$T_{st} = \frac{K_m V_{dc}}{R} \tag{2.25}$$

and the no-load speed Ω_{nl} is calculated at null torque:

$$\Omega_{nl} = \frac{V_{dc}}{K_m} \tag{2.26}$$

therefore, the working envelope is constrained by the area limited by the stall torque and no-load speed, as shown in Fig.2.7 the red lines.

Considering one special case, when the motor phases are in short circuit, which means $V = 0$, we obtain the short-circuit damping as indicated by the black line in Fig.2.7. In this case, the torque is represented by:

$$T = -\frac{K_m^2}{R}\Omega \tag{2.27}$$

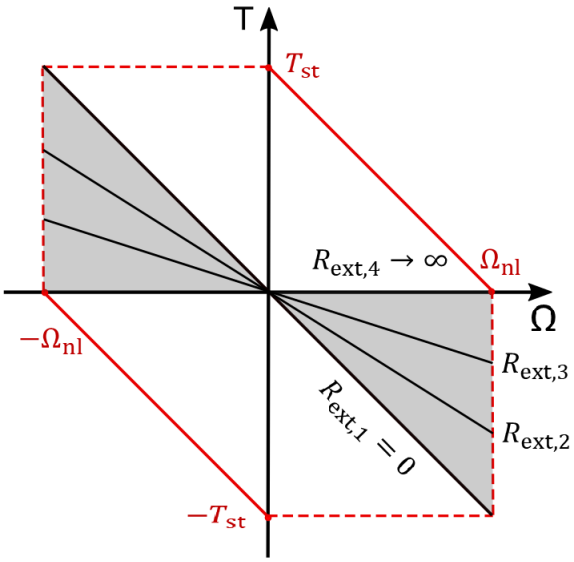

Fig. 2.8 Torque speed map for power recovery

As we mentioned before in the assumptions, the supply voltage can vary from $-V_{dc}$ to V_{dc}, varying the supply voltage will yield a group of parallel lines with the same slope but different offsets as shown in Fig.2.7 the gray lines.

After defining our working envelope, next step is to define the power recovery region.

According to the sign convention, power is regenerated only if $Vi < 0$. In other words, the torque and the supply voltage must have the opposite signs. This is shown in the gray regions in Fig.2.8.

The recovery region is bounded between the open-circuit response which means $T = 0$ and the short-circuit response. Every other torque speed combination outlying from this region will require a certain amount of power.

Alternatively, the same behavior can be obtained by shunting the stator with an external resistance. In this case, the damping slope changes as shown in Fig.2.8, R_{ext} can vary from 0 to infinity:

$$T = -\frac{K_m^2}{R + R_{ext}}\Omega \tag{2.28}$$

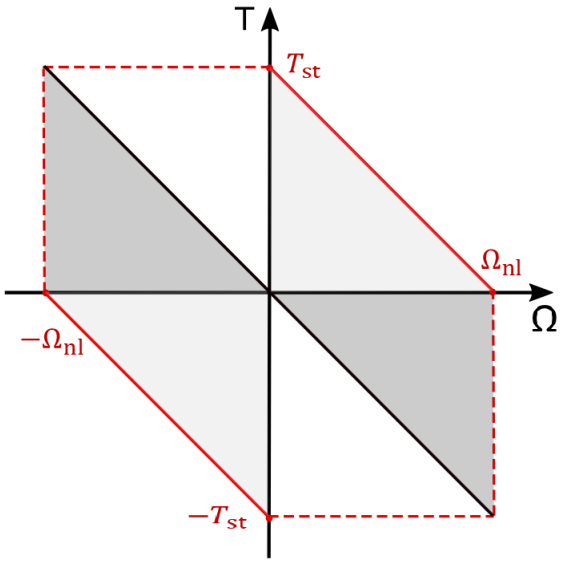

Fig. 2.9 Torque speed map working regions

Fig.2.9 summaries what we have discussed before, the working envelope can be divided into 3 different regions:

- *Regenerative damping (dark gray)* The torque (hence current) and the voltage present opposite signs, power flows into the battery. The machine behaves as a damper because torque and speed are opposite;
- *Active motor (light gray)* The torque (hence current) and voltage have the same sign: the device behaves as a motor because the speed and the torque have the same sign;
- *Active damper (white)* The torque (hence current) and supply voltage have the same signs. However, the torque and speed oppose each other. This configuration is a damper helped by an external supply to fulfill the required behavior.

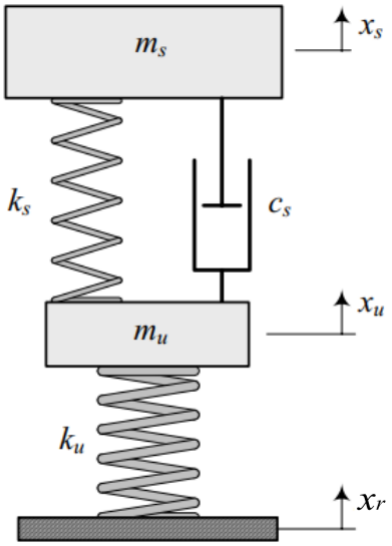

Fig. 2.10 An example scheme of quarter car model.

2.3 Preliminary Analysis

2.3.1 Quarter Car Model

Quarter car model is the most employed and common model that used for studying the vehicle suspension system [103], as shown in Fig.2.10.

The model is basically made of two masses, sprung mass m_s and unsprung mass m_u. The sprung mass represents one quarter of the vehicle body weight, and the unsprung mass represents one wheel of the vehicle. The sprung mass is supported by a spring with stiffness k_s, and a shock absorber with viscous damping coefficient c_s, while the unsprung mass is in contact with the ground through the tire, which can be represented with a stiffness k_u, noticed here, the damping of the tire is ignored due to its small value compared with c_s to simplify the model. Variables x_s, x_u, and x_r represent the vertical displacements at different levels.

The differential equations of the motion for quarter car model can be written as:

$$m_s\ddot{x_s} + c_s(\dot{x_s} - \dot{x_u}) + k_s(x_s - x_u) = 0 \tag{2.29}$$

$$m_{\mathrm{u}}\ddot{x}_{\mathrm{u}} + c_{\mathrm{s}}(\dot{x}_{\mathrm{u}} - \dot{x}_{\mathrm{s}}) + (k_{\mathrm{u}} + k_{\mathrm{s}})x_{\mathrm{u}} - k_{\mathrm{s}}x_{\mathrm{s}} = k_{\mathrm{u}}x_{\mathrm{r}} \tag{2.30}$$

which is commonly expressed with the state space form:

$$\begin{cases} \dot{\mathbf{x}} = \mathbf{A}\mathbf{x} + \mathbf{B}\mathbf{u} \\ \mathbf{y} = \mathbf{C}\mathbf{x} + \mathbf{D}\mathbf{u} \end{cases} \tag{2.31}$$

in which, the state vector **x** and the control input **u** are given below as an example:

$$\mathbf{x} = \begin{bmatrix} x_{\mathrm{s}} \\ x_{\mathrm{u}} \\ \dot{x}_{\mathrm{s}} \\ \dot{x}_{\mathrm{u}} \end{bmatrix}, \qquad \mathbf{u} = \begin{bmatrix} \dot{x}_{\mathrm{r}} \\ x_{\mathrm{r}} \end{bmatrix}. \tag{2.32}$$

However, depends on the requirement, the output vector **y** can be defined freely by the user, and in this way, the matrix **A**, **B**, **C**, and **D** (usually contains the information about system mass, stiffness and damping properties) will be calculated accordingly.

This simple linear quarter-vehicle model has several advantages: due to its simple structure and low dynamic order it offers an intuitive understanding of the vertical dynamic behavior of the vehicle.

Furthermore, after making suitable modifications on the original quarter car model, it can be also used to assess the behavior of the suspension which equipped with regenerative shock absorber.The modified model will be fed with a certain road profile, based on the simulation results, several performance indicators (for example, the potential harvested power, conversion efficiency, vehicle comfort and road holding properties) are evaluated and this will be discussed in the following sections.

2.3.2 Suspension Assessment

To assess the performance of vehicle suspension and study the behavior of the system excited by the road irregularities, a quarter car model is commonly adopted. To feed this model, a particular road profile will be first generated and used later as an input.

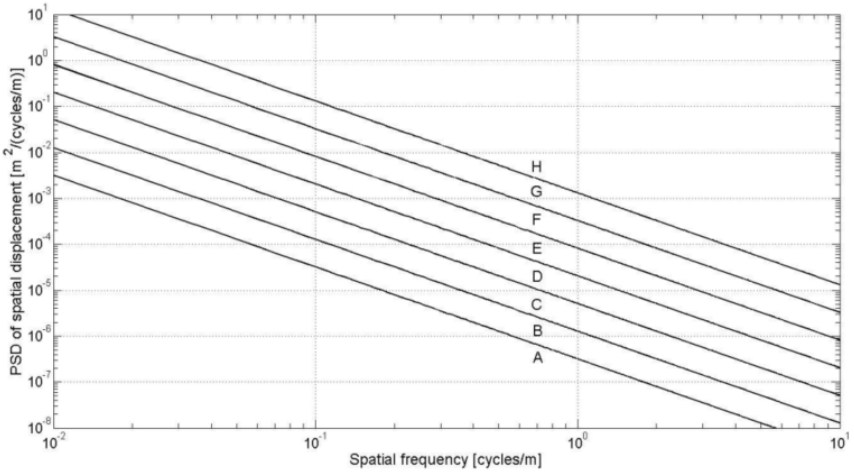

Fig. 2.11 Power Spectral Densities of different road profiles according to [19].

It is known that a random profile can be indicated by superimposing a number of sine waves. For a certain road, if the Power Spectral Density (PSD) of the profile is known, it is possible to reconstruct the road condition by using the relationship between the road height and the position.

Furthermore, the road roughness is usually represented as a stationary Gaussian stochastic process and thus, the road profile PSD can be expressed by:

$$S_{\mathrm{PSD}}(n) = G_r n^{\beta} \tag{2.33}$$

where n is the spatial frequency, G_r is the road roughness coefficient, and the exponent β is commonly approximated as -2.

According to International Organization for Standardization (ISO), the road profiles can be divided into eight classes, indicated by letters from A to H [19]. Their relative PSDs can be found in Fig.2.11. Class A refers to very good roads for example, the newly paved highways; class B indicates good road condition, class C refers to an average road, class D a poor road and so on. However, in general, most of the roads in our daily lives can be considered in the range from class A to D.

The road profile used in our application was generated based on ISO 8608 standard [19]. Specifically, these road profiles with different PSDs $S(n)$ and road roughness coefficients G_r are listed in Tab.2.1, where the spatial frequency $n_0 = 0.1 cycle/m$.

Table 2.1 ISO Road Profiles

Road class	**Description**	$\mathbf{S(n_0)[m^3/cycle]}$	$\mathbf{G_r[m/cycle]}$
A	Very good	1.60e-5	1.60e-7
B	Good	6.40e-5	6.40e-7
C	Average	2.56e-4	2.56e-6
D	Poor	1.02e-3	1.02e-5
E	Very poor	4.10e-3	4.10e-5

Eq.2.33 shows the relationship between $S(n)$ and G_r in space frequency domain. By taking into account the vehicle velocity v_{car}, now it can be converted in the time domain.

$$\begin{cases} f = v_{\text{car}} n \\ S(f) = S(n)/v_{\text{car}} \end{cases} \tag{2.34}$$

by substituting Eq.2.33, $S(f)$ can be expressed as:

$$S(f) = \frac{G_r v_{\text{car}}}{f^2} \tag{2.35}$$

Note that the road profile generation can be done by using white noise, and $S(f)$ is expressed in the unit of m^2/Hz, thus, $S(f)$ can be rewritten as:

$$S(f) = |H(f)|^2 S_{\text{in}}(f) \tag{2.36}$$

By setting $S_{\text{in}} = 1$, $|H(f)|$ is expressed as:

$$|H(f)| = \frac{2\pi\sqrt{G_r v_{\text{car}}}}{2\pi f} \tag{2.37}$$

and knowing that $s = j2\pi f$, therefore, we can obtain:

$$H(s) = \frac{2\pi\sqrt{G_r v_{\text{car}}}}{s} \tag{2.38}$$

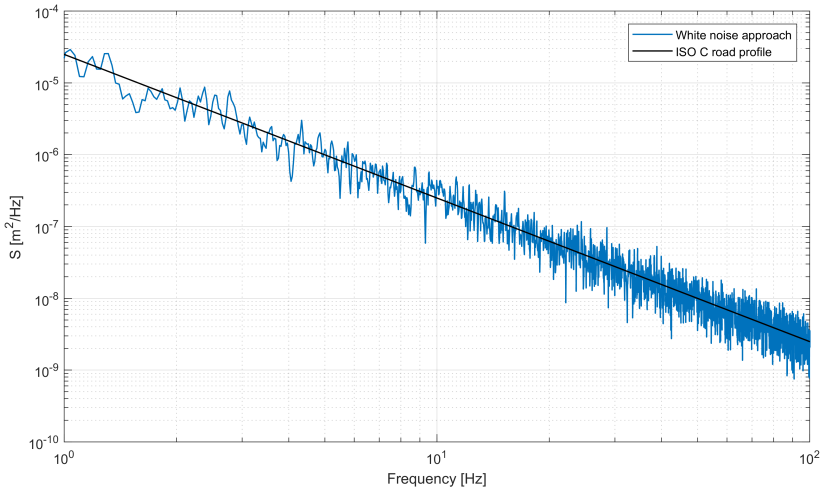

Fig. 2.12 Road Profile Class C

Furthermore, by adding a cutoff pole at low frequency to avoid drifts, the PSD white noise signal can be expressed as:

$$H_{\mathrm{r}}(s) = \frac{2\pi\sqrt{G_r v_{\mathrm{car}}}}{s + 2\pi f_0} \tag{2.39}$$

the filter cutoff frequency is indicated by f_0 and can be represented as :

$$f_0 = \frac{v_{\mathrm{car}}}{\lambda_0} \tag{2.40}$$

where $\lambda_0 = 100\ m$

If a class C (average) road with $G_r = 2.56 \cdot 10^{-6} m/cycle$ and $v_{\mathrm{car}} = 35 km/h$ is considered. In particular, this value is the average vehicle speed of the New European Driving Cycle (NEDC). The simulation result can be seen in Fig.2.12.

Once the road profile is obtained, it is time to feed the quarter car model as shown in Fig.2.13. In this modified version, the original damper c_{s} is replaced by a generic dissipative device that can impose a damping force F_{damp} as a function of piston speed v_{p}. Particularly, an off-road passenger vehicle (Jeep Renegade) is taken as a reference. All the parameters which are considered in the model are listed in Table 2.2.

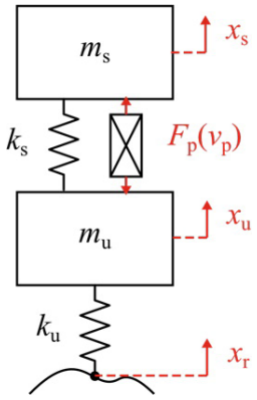

Fig. 2.13 Modified quarter car model

Table 2.2 Quarter car model parameters

Parameters	**Symbol**	**Front**	**Rear**
Sprung mass	m_s	416.5 kg	256 kg
Unsprung mass	m_u	40 kg	30 kg
Suspension stiffness	k_s	23.26 kN/m	21.74 kN/m
Tire stiffness	k_u	226 kN/m	206 kN/m

To evaluate correctly the performance of the shock absorber within the quarter car model, the useful metrics presented by Zuo and Zhang[104] are employed.

Since the shock absorber is assumed to use a brushless permanent-magnet electric machine, its regenerated power can be calculated through the formula below , :

$$P_g = \frac{3}{2} R_{ext}(i_d^2 + i_q^2) \tag{2.41}$$

where R_{ext} is the external resistance of the electric machine, i_d and i_q represent the current of direct and quadrature axis respectively.

Instead, the damping power can be represented by the product of damping force and piston speed:

$$P_{\mathrm{d}} = F_{\mathrm{damp}} v_{\mathrm{p}} = F_{\mathrm{damp}} (\dot{x_{\mathrm{s}}} - \dot{x_{\mathrm{u}}}) \tag{2.42}$$

as suggested in literature [104], the damping power in the suspension is heavily influenced by the road profile, the vehicle speed and the tire stiffness. Its dependence on the other quarter car model parameters is negligible, thus, it can be approximated by:

$$P_{\mathrm{d}} = \pi^2 G_r v_{\mathrm{car}} k_{\mathrm{u}} \tag{2.43}$$

therefore, the conversion efficiency can be determined by the ratio between regenerated and dissipated power:

$$\eta_{\mathrm{g}} = \frac{P_{\mathrm{g}}}{P_{\mathrm{d}}} \tag{2.44}$$

Comfort property can be assessed by filtering the sprung mass acceleration with

$$H_{2631}(s) = \frac{80.03s^2 + 989s + 0.02108}{s^3 + 78.92s^2 + 2412s + 5614} \tag{2.45}$$

which yields a weighted acceleration a_w that takes into account the human sensitivity indicated by the ISO 2631 standard [105]

Whereas, road holding behavior can be evaluated through index η_{rh} which is defined as:

$$\eta_{\mathrm{rh}} = \frac{k_{\mathrm{u}}(x_{\mathrm{u}} - x_{\mathrm{r}})}{(m_{\mathrm{s}} + m_{\mathrm{u}})g} \tag{2.46}$$

this index represents the ratio between dynamic forces due to tire deflection and static forces due to the vehicle weight. Indexes larger than unity indicate the loss of ground contact.

To yield characteristic numbers for these four indicators, the mean values of harvested power and conversion efficiency were calculated. Instead, for weighted acceleration and road holding index, their RMS values were obtained. These parameters were assessed in a sensitivity analysis with respect to the shunt resistance, as illustrated in Fig.2.14

From the sensitivity analysis results, it is shown that when the shunt resistance R_{ext} equals to 0.14 Ω will lead to a maximum harvested power and conversion

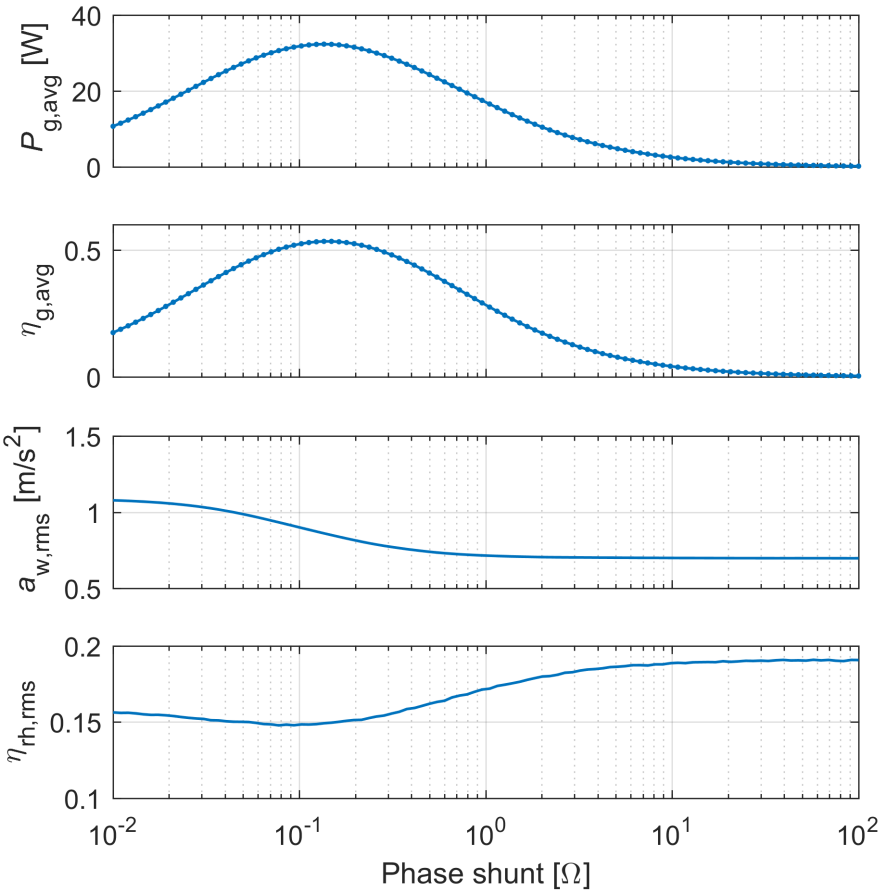

Fig. 2.14 Sensitivity analysis of evaluation parameters to shunt resistance for regenerative shock absorbers

efficiency for the target regenerated shock absorber with specific pump and electric motor characteristics. Meanwhile, from the results of weighted acceleration a_w and road holding index η_{rh}, when the shunt resistance is chosen, a relative good compromise between the ride comfort and vehicle road holding capabilities is also guaranteed.

It is also possible to obtain a rough estimation of the emission savings in terms of grams of CO_2 per kilometer according to the European technical guidelines for eco-innovation [99].

$$S_{\text{CO}_2} = \frac{\eta_{\text{conv}} P_{\text{g}} V_{\text{pe}} C_{\text{f}}}{\eta_{\text{a}} v_{\text{car}}} \tag{2.47}$$

Table 2.3 Estimated CO_2 emission reduction with different road profiles

Road class	Description	$\mathbf{G_r}[\mathbf{m/cycle}]$	$\mathbf{S_{CO_2}}[\mathbf{gCO_2/km}]$
A	Very good	1.60e-7	0.16
B	Good	6.40e-7	0.64
C	Average	2.56e-6	2.6
D	Poor	1.02e-5	10
E	Very poor	4.10e-5	41

where η_{conv} is the total conversion efficiency of the power stage and its value is assumed as 0.9, V_{pe} is the fuel consumption of effective power for a reference diesel engine with a value of 0.22 l/kWh, $C_{\text{f}} = 2640g/l$ is a factor that considers the fuel conversion into CO_2 and $\eta_{\text{a}} = 0.67$ is the alternator efficiency.

Quick estimation can be done by substituting the regenerated power for all the four dampers, and as a result, Eq. 2.47 can be rewritten as:

$$S_{\text{CO}_2} = \frac{\eta_{\text{conv}}\eta_{\text{g}}}{\eta_{\text{alt}}}\pi^2 G_r \cdot \sum_{i=1}^{4} k_{\text{u},i} \cdot V_{\text{pe}} C_{\text{f}} \tag{2.48}$$

From Eq.2.48, it is observed that the emission reduction is directly proportional to the road roughness coefficient G_r, while showing no dependence on the vehicle velocity v_{car}. Furthermore, if a class C (average) road profile is considered, together with a conversion efficiency η_{g} of 0.54 is assumed, Eq.2.48 can yield a 2.6 g/km of CO_2 savings for all the four regenerated shock absorbers. More simulation results considering different road roughness coefficients can be seen in Tab.2.3 and these approximations proved that the regenerative device could be advantageous for vehicle emission reduction.

Chapter 3

Hydraulic Pump Design

From this chapter, a detailed design and optimization process of the proposed regenerative shock absorber will be explained. To do this, a system level design approach as shown in Fig. 3.1 is adopted to comply with different requirements in all the domains of interest. Particularly, three different specification sets are considered here:

1. *Damping requirements.*
   The proposed device must act as a fully functional shock absorber to exhibit the required force-speed characteristic to perform desired damping actions.

2. *Target envelope requirements.*
   Since the proposed device will be integrated to the vehicle suspension, any interference with other components in that region must be avoided either under static or dynamic conditions (such as suspension deflection and vehicle steering maneuvers).

3. *Power supply requirements.*
   Assuming the power stage of the proposed device is connected with the vehicle battery which is shared among different accessories. Therefore, some intrinsic limitations like DC voltage, State of Charge (SOC) and charge-discharge rates need to be taken into account during the design phase to guarantee the system reliability.

The first requirement about damping can be used to establish the design specifications for the hydraulic part of the proposed device (pump), for example, defining

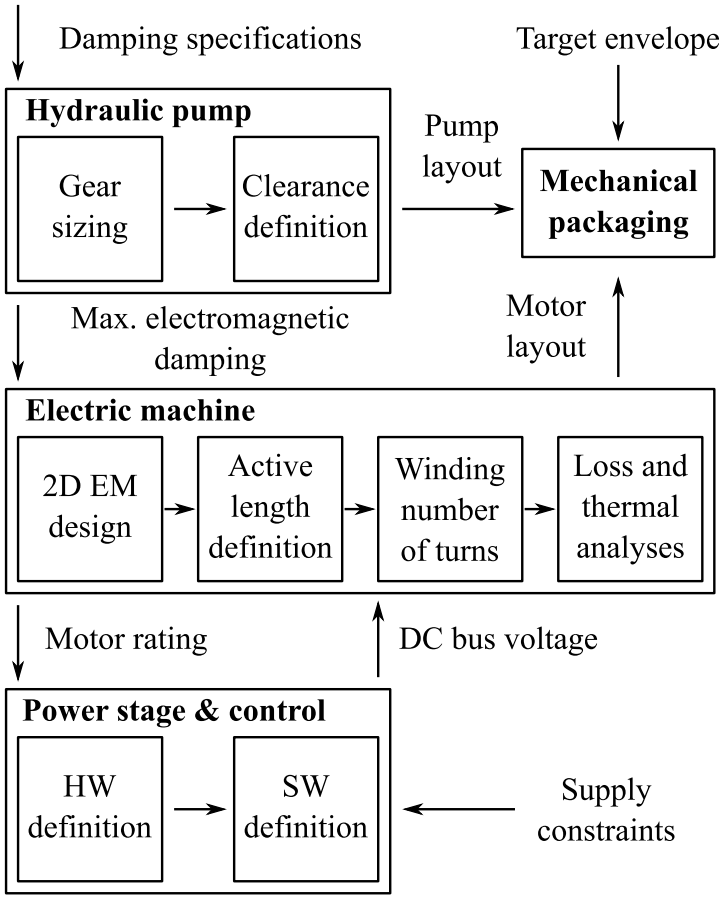

Fig. 3.1 Design method for the motor-pump unit

the gear geometry and clearance. Once the characteristics of hydraulic pump is fully defined, the electromagnetic design of the electric machine can be carried out such as stator and rotor configurations (slotted or slotless), pole pair numbers, and active length, while the winding layout, size and number of turns, instead, are selected to meet the limitation of DC supply voltage. After the whole design process of pump and electric machine, the proposed motor-pump group will be validated with a thermal analysis in the worst-case working condition.

To meet the second requirement about the envelope space, it would be helpful to minimize the bulk and mass of the final prototype to comply with the established geometry constraints. Therefore, the proposed device can be easily integrated to the vehicle suspension system without any interference, to achieve this target, multiple iteration processes are needed.

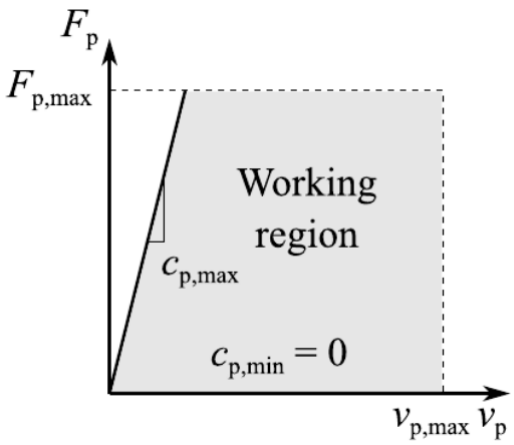

Fig. 3.2 Ideal Force-speed maps of the regenerative shock absorber limited by damping, force and speed values.

Considering the third requirement about the power stage and control, both hardware and software components used to construct the power stage system are selected based on the electric machine characteristics and power supply constraints. A suitable control strategy is also implemented taking into account the damping requirements and other physical limitations of the system.

Fig.3.2 shows the first quadrant of the force-speed map, the x axis represents the piston speed v_{p} while the y axis represents the damping force F_{damp}. It is known that the damping coefficient c_{p} can be defined by the ratio between force and speed (shown as the slope in the figure), therefore, one feasible choice to define the working region is to constrain this working area as purely regenerative which means the battery can only absorb power from the system. Specifically, this working region is bounded by maximum damping $c_{\mathrm{p,max}}$, maximum force $F_{\mathrm{damp,max}}$ and speed $v_{\mathrm{p,max}}$ that the suspension can achieve.

Due to the linear-to-rotary conversion is not perfectly efficient, this working envelope will be inevitably reshaped, as shown in Fig. 3.3, mainly the following two phenomena are taken into account:

1. *Pump leakages*

   Pump leakage paths will speed up the effective damping inside the system, in this way, for any attainable damping behavior, a lower damping coefficient or a smaller slope of the damping curve is expected, and this correspond to the volumetric efficiency η_{v} defined in Eq.2.16.

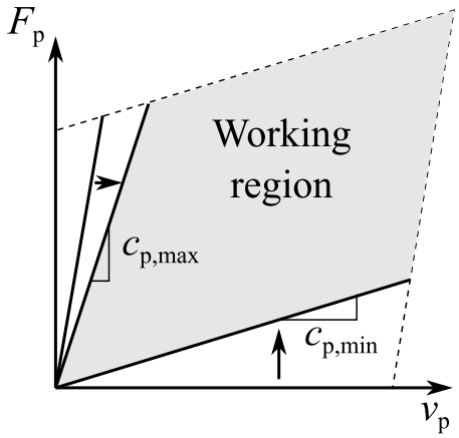

Fig. 3.3 Expected Force-speed maps of the regenerative shock absorber limited by damping, force and speed values

2. *Hydro-mechanical losses*

   Since the hydraulic pump and the electric machine are both mechanical components, in reality the hydro-mechanical losses (for example the pressure drop and mechanical friction) for the pump and electric machine are not avoidable, as a result, this will increase the output force and hence the output damping behavior which is equivalent to increase the slop of the damping curve and these losses correspond to the hydro-mechanical efficiency η_{hm} defined in Eq.2.17.

It is worth to note that at low speed region, the pump leakage phenomenon has more influence, therefore, due to volumetric efficiency the actual maximum damping value will be lower than that in the ideal case. As the speed increases, the hydro-mechanical loss becomes dominant, and due to the inherent efficiency η_{hm}, the real minimum damping will be greater than zero. Although this non-null value of $c_{p,min}$ will penalize the final conversion efficiency of the device, it also provides a passive damping action to the vehicle in case of system failure.

Specifically, the proposed hydraulic pump is going to adopt a gerotor layout as shown in Fig.3.4. This fixed displacement device consists of only two elements: one inner gear and one outer gear. Both gears have conjugate tooth profiles, the outer gear presents one additional tooth with respect to the inner gear and generate a number of chambers in between. The inner gear is usually fixed on a rotating shaft

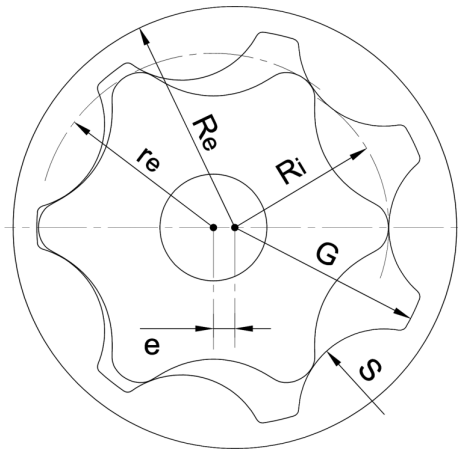

Fig. 3.4 Layout of a generic gerotor pump

while the outer gear is positioned at a fixed eccentricity from the center of inner gear and shaft.

As mentioned in the design guidelines [20], despite of a variety of geometries and materials, all the gerotor sets share the same basic working principle as shown in the Fig.3.5, when the pump is working, the inner gear is driven by the shaft, the fluid will be drawn into one chamber and starts to enlarge its volume until reaching the maximum value, as the rotation continuous, the volume of the chamber will decrease and therefore, the inside fluid will be forced to flow out of the original chamber and start to fill in the next chamber. This process will take place continuously and as a result, a smooth pumping action is provided.

Furthermore, in the gerotor pump, the movement between inner and outer gears is a pure relative rolling, and compared to other systems with sliding elements, this pure rolling motion effectively reduces the wear and shows a larger mechanical efficiency. If the shaft moves with a speed of Ω_{g}, while this relative rolling motion takes place at rather low speed as shown below:

$$\Omega_{\mathrm{g,rel}} = \Omega_{\mathrm{g}} \left(1 - \frac{N_{\mathrm{g}}}{N_{\mathrm{g}} + 1} \right) = \frac{\Omega_{\mathrm{g}}}{N_{\mathrm{g}} + 1} \tag{3.1}$$

where N_{g} is the number of teeth on the inner gear.

In summary, compared with other pump types, the advantages of such gerotor pump can be seen from:

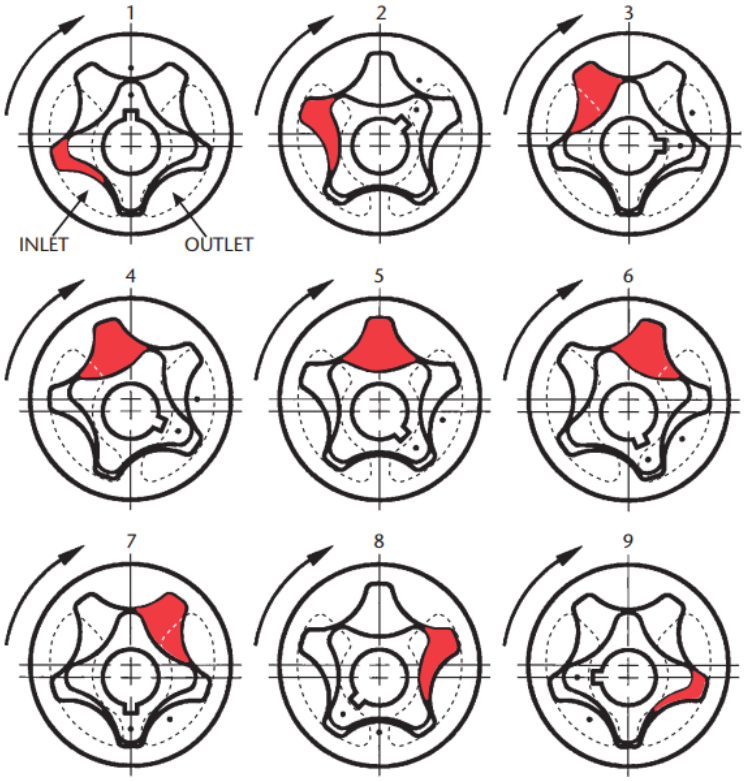

Fig. 3.5 Working principle of a generic gerotor pump in [20].

- The *simplicity* of the gerotor pump requires the least amount of components to machine, for example, compared with spur gears, gerotor can eliminate a shaft and two bearings.
- The *versatility* of the gerotor pump gives the greatest advantages, it can be mounted directly on the shaft or driven by the outer gear, it is suitable for a large variety of fluids from air to hot melt liquid.
- The size and geometry of the gerotor pump can be adjusted accordingly to meet specific requirements. In general, the inner gear diameter, outer gear diameter and the active length can be optimized to be coherent with the designed overall size and weight.
- Since the relative velocity between the inner and outer gears is very low and this leads to a reduced tooth wear compared with other types, therefore gerotor pumps usually can have a longer service life.

- The gerotor pumps are suitable for the low-mid pressure range (up to 150 bar) which is coherent with our applications for shock absorbers in automotive field.

In general, the gerotor pump can be characterized by its volumetric displacement V_g. Based on the analysis made in the EHA modeling part, it is known that when the ideal transmission ratio τ is given, the electromechanical torque T_m as well as the rotational speed Ω_g can be defined as:

$$\begin{cases} T_m = \tau F_p \\ \Omega_g = v_p/\tau \end{cases} \tag{3.2}$$

Therefore, the maximum angular speed $\Omega_{g,max}$ under low pressure condition (when the pump internal leakages are small) can be approximated as

$$\Omega_{g,max} \cong \frac{v_{p,max}}{\tau}. \tag{3.3}$$

From Eq.3.3, the ideal transmission ratio can be computed as the ratio between maximum angular and linear speeds. For example, in the proposed design condition, a 12 krpm rotating speed versus a linear speed of 1.5m/s is considered.

Once τ is defined, the volumetric displacement can be represented as:

$$V_g = \tau A_p = \frac{v_{p,max}}{\Omega_{g,max}} A_p \tag{3.4}$$

In this case, the average piston cross section A_p is calculated through:

$$A_p = \frac{\frac{\pi}{4}[(d_p^2 - d_r^2) + d_r^2]}{2} \tag{3.5}$$

where d_p and d_r represent the diameter of piston and rod inside the cylinder respectively.

Noticed that V_g is limited by the maximum angular speed that the system can achieve, and this maximum speed constraint has to be pushed as high as possible in order to lower the required damping torque and hence, minimize the envelope of the

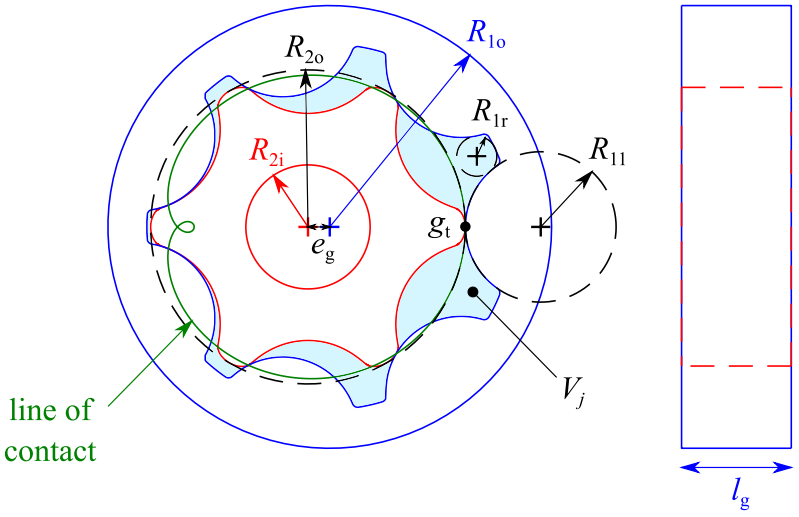

Fig. 3.6 Gear profile of the gerotor pump

electric motor. Nevertheless, the design must also account for the limitations in the filling capability of the gerotor pump at high speed [106].

3.1 Gear Geometry

Fig.3.6 shows the section and side view of a gerotor gear set with its geometric features, the main parameters for the pump design are listed in Tab.3.1. The inner gear has a number of teeth equals to N_g (in this case N_g is equal to 6) while the outer gear has $N_g + 1$ teeth, and thus, the pump preserves $N_g + 1$ fluid chambers sealed by the teeth tips of both gears. Angle θ_g is used to represent the angular position of the shaft, furthermore, the volume of a generic chamber V_j can be described with a generalized periodic function with appropriate angular offset:

$$V_j = f_v\left(\theta_g + \frac{2\pi j}{N_g + 1}\right) \quad \forall j \in [0, N_g]\,. \tag{3.6}$$

Noticed that the function f_v depends on the geometric features of both gears. In turn, the kinematic flow rate of the pump is expressed as

$$Q_g(\theta_g) = \Omega_g \sum_{j=0}^{N_g} \mathscr{F}_j(\theta_g), \tag{3.7}$$

Table 3.1 Geometric parameters for gerotor pump design

Design parameter	Description
N_g	Number of inner gear teeth
$R_{1\mathrm{o}}$	Outer gear outside radius
$R_{1\mathrm{l}}$	Outer gear lobe radius
$R_{1\mathrm{r}}$	Outer gear root radius
$R_{2\mathrm{o}}$	Inner gear outside radius
$R_{2\mathrm{i}}$	Inner gear inside radius
e_g	Eccentricity
g_t	Inter-teeth clearance
l_g	Gear length
V_j	Volume of the jth chamber

where

$$\mathscr{F}_j(\theta_\mathrm{g}) = -\min\left(\frac{\mathrm{d}V_j}{\mathrm{d}\theta_\mathrm{g}}, 0\right) \tag{3.8}$$

is a nonlinear function that denotes the volumetric emptying rate of each chamber. The volumetric displacement is calculated as the ratio between the flow rate and the angular speed:

$$V_\mathrm{g}(\theta_\mathrm{g}) = \frac{Q_\mathrm{g}(\theta_\mathrm{g})}{\Omega_\mathrm{g}}, \tag{3.9}$$

in formal terms, the design target should be the average value per revolution:

$$\bar{V}_\mathrm{g} = \frac{1}{2\pi}\int_0^{2\pi} V_\mathrm{g}(\theta_\mathrm{g})\mathrm{d}\theta_\mathrm{g}. \tag{3.10}$$

The pulsation index δ_g gives an indication of the flow ripple. However, the minimization of this phenomenon is desirable in shock absorbers because it could

introduce unwanted vibrations into the suspension. Here, δ_g can be defined as:

$$\delta_g = \frac{\max\left(V_g(\theta_g)\right) - \min\left(V_g(\theta_g)\right)}{\bar{V}_g}. \tag{3.11}$$

Noticed that the pulsation index is greatly influenced by another parameter which is the tooth profile. In [65], the authors have demonstrated that the inter-teeth clearance g_t and the teeth aspect ratio

$$\alpha_t = \frac{R_{1l}}{R_{1r}} \tag{3.12}$$

are relevant for the volumetric efficiency. The minimization of g_t shrinks the inter-teeth passage cross section, while the reduction of α_t increases the passage length. The final outcome is the diminution of leakage in the tooth tip area.

The gear aspect ratio α_g is considered as another relevant design parameter and it can be defined as:

$$\begin{cases} \alpha_{g1} = R_{1o}/l_g \\ \alpha_{g2} = R_{2o}/l_g \end{cases}. \tag{3.13}$$

Their selection is driven by considerations on mechanical losses and inertial contributions. Later in the design verification part about the drag analysis, we will see that the viscous drag can be split in two main torque losses: radial and axial components. The radial drag only affects the outer gear and originates from the thin fluid film between the pocket and the gear outside diameter. Its contribution reported to the output shaft of the pump can be approximated as

$$T_{ro} \cong \left(\frac{N_g}{N_g+1}\right)^2 \frac{4\pi\mu_f l_g R_{1o}^3}{g_o}\Omega_g, \tag{3.14}$$

where μ_f is the fluid dynamic viscosity and g_o is the outside diameter clearance (defined later in the clearance design section). Equation 3.14 assumes a homogeneous distribution of the gap between the outer gear and the pocket along their circumference. However, this simplification does not affect the dependence with l_g and R_{1o}^3.

Similarly, the axial drag acts on the cross sections of both gears due to the film between gears and the casing. It yields a cumbersome analytic expression because it is predominantly influenced by the geometries of the gears and the casing (such as hydraulic ports and grooves). Nevertheless, it can be stated that the axial viscous drag is a function of R_{1o}^4 and R_{2o}^4, since their cross section depends on the squared radius and the transformation of linear variables into the rotary domain requires another squared radius term.

To analyze the inertial contribution, both gerotor gears can be simplified as hollow cylinders and the moment of inertia for a generic hollow cylinder is described as:

$$J_{\mathrm{cyl}} = \frac{\pi \rho_{\mathrm{cyl}} l_{\mathrm{cyl}}}{2} \left(R_{\mathrm{cyl,o}}^4 - R_{\mathrm{cyl,i}}^4 \right), \tag{3.15}$$

where ρ_{cyl} is its mass density, l_{cyl} its length, and $R_{\mathrm{cyl,o}}$ and $R_{\mathrm{cyl,i}}$ its outside and inside radii, respectively. Hence, it can be deduced that both gear moments of inertia depend on R_{1o}^4.

As a result, during the pump design process, it is favored to minimize α_{g1} and α_{g2} within the established envelope limits.

3.2 Hydraulic Ports

According to the guideline [20], hydraulic porting is also an important aspect for the design. Depending on the application and manufacturing considerations, there exist a number of choices.

In the proposed design, the twin-tube damper will provide an intrinsic fluid flow rectification. Therefore, a symmetric port architecture which will yield the same hydraulic behavior in both directions is adopted to simplify the applicability for bidirectional operation. Fig.3.7 shows the geometry features on the section view of a symmetric port with inside radius R_{pi}, outside radius R_{po}, opening angle γ_{p}, minimum distance d_{p} and gear eccentricity e_{g}.

Compared with other types, the chosen port structure exhibits a better filling and sealing feature, while the disadvantages mainly come from the complexity of machining. Furthermore, it is also recommended to have the so-called shadow groove

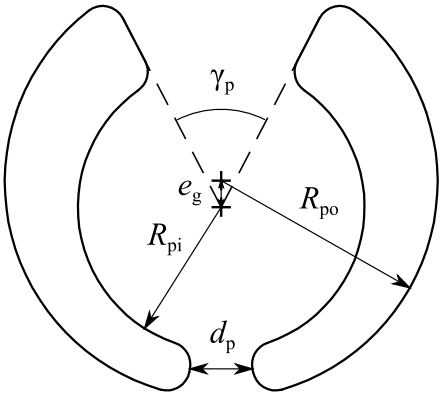

Fig. 3.7 Hydraulic port geometry.

features by replicating the same porting geometry on the bottom of the gear pocket (sometimes lubrication channels can be also found on the side wall of the casing). This operation will help (pressure) balance the pump axially and further reduce the viscous drag.

The port depth is another crucial aspect need to be considered, a proper design should not restrict the pump flow and guarantee a correct fluid fill especially on the inlet side. And it is mentioned in some design handbook that this depth must be at least equal to the length of the rotors. Just to complete our design, once the porting has been chosen, further considerations for example, the size, length and design of inlet lines also need to be taken into account in order to optimize the inlet flow.

3.3 Clearances Design

To define the clearances between the gears and the casing is considered as a challenging step in the pump design process. Furthermore, the most important clearances which will influence the pump performance are defined and listed below:

- *Inside diameter clearance* g_i

  It is defined as the difference between inner gear and shaft diameters:

$$g_i = 2R_{2i} - D_s \tag{3.16}$$

  where D_s is the shaft diameter.

- *Outside diameter clearance* g_o

  It is defined as the difference between pocket and outer gear diameters:

$$g_o = D_p - 2R_{1o} \tag{3.17}$$

  where D_p is the pocket diameter.

- *Axial clearance* g_a

  It is defined as the difference between pocket depth and gear axial length:

$$g_a = l_p - l_g \tag{3.18}$$

  where l_p is the pocket depth.

This task was accomplished with the aid of *Simerics Pumplinx*, which is a 3D Computational Fluid Dynamics (CFD) tool that can provide accurate virtual testing for the analysis and performance prediction of fluid devices such as pumps, turbines, compressors, and valves, or complete fluid systems with rotating or sliding components.

Using such software enables to obtain reliable simulation results, yet keeping a relatively low computing effort with respect to other software alternatives.

To set up the simulation, first the 3D geometry of the fluid is required and this can be done by importing the model directly from CAD files as shown in Fig.3.8, and next step is to create mesh for each fluid domain including ports, shadow ports, gerotor chambers and clearance gaps.

Here we need to pay attention on the number of cell layers within these gaps, according to [106] and [107], in order to reproduce the leakage flow accurately, at least three cell layers are needed and the generated meshes must present a gradual cell density transition as shown in Fig.3.9.

The fluid domains are interfaced with mismatched grids, which are useful to couple static and moving domains. Pumplinx implements an efficient method that first identifies the common areas between mismatched grids and then treats them like generic interfaces. Therefore, the problem solution is fully conservative, fully implicit and fast [108].

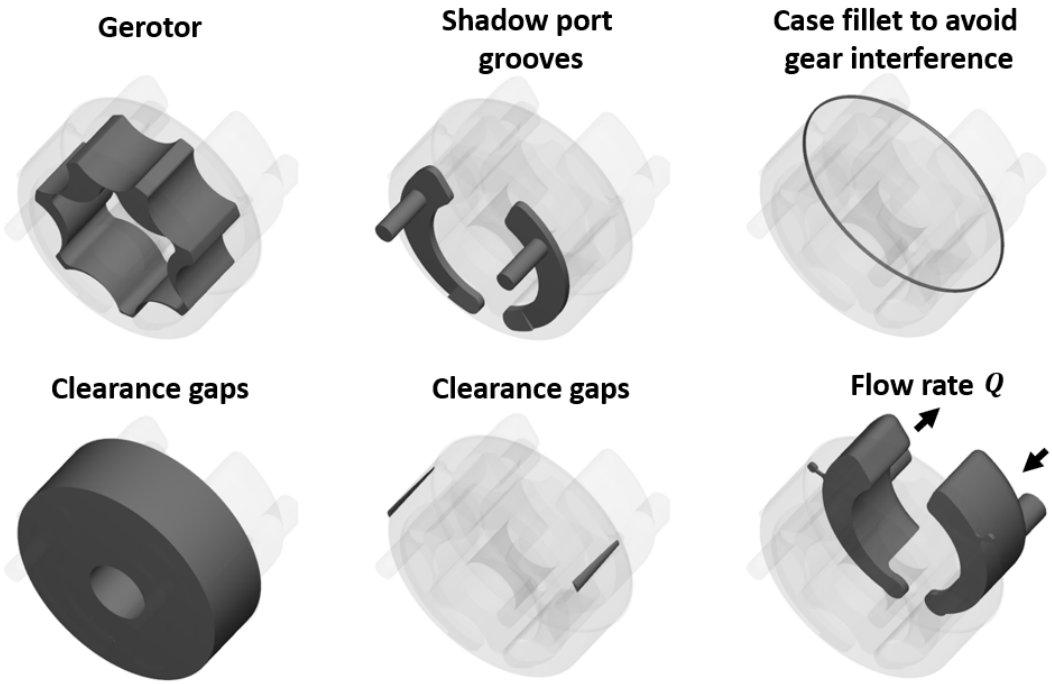

Fig. 3.8 Fluid geometry extraction and imported into Pumplinx

Another key factor for the efficiency characteristics of the pump is oil properties. It is obvious that oil with low viscosity will lead to more leakages and less viscous drag, while with high-viscosity fluids the opposite phenomenon is expected. In fact, the properties of employed fluid will be inserted to the program as an input. Furthermore, it should be noticed that viscosity is heavily affected by the temperature. Tab.3.2 shows the oil properties which are used in the proposed design.

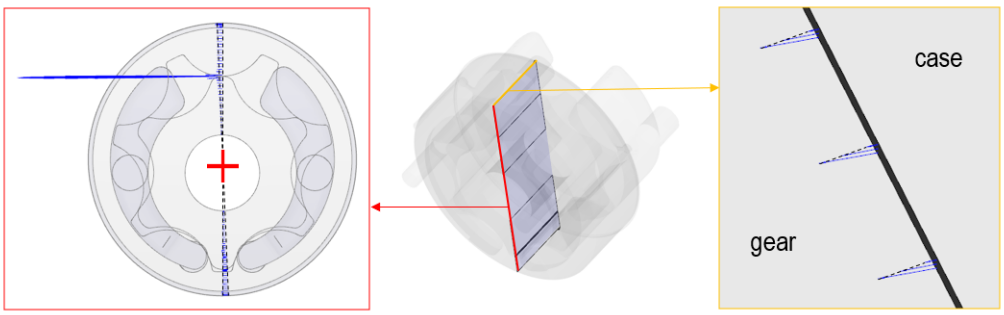

Fig. 3.9 CFD analysis of Viscous loss in Pumplinx

Table 3.2 Oil properties

Oil parameter	Values
Density	836 kg/m^3
Bulk modulus	2.15 GPa
Gas mass fraction	9e-5
Operating temperature	300 K
Kinematic viscosity	22.7 cSt

To understand the effectiveness of clearances, different models will be simulated with laminar flow and cavitation modules. The models are initialized with constant pressure drop between the pump ports (ΔP_{g}) and constant inner gear angular speeds (Ω_{g}). After the initial transient is vanished, the average values of the gerotor torque (T_{m}) and the flow rate across the ports (Q_{g}) are extracted.

The clearances, instead, are inserted in the geometry using the gerotor template mesher in Pumplinx. Since the software does not consider fluid-body interactions, the clearances will remain constant as initial value at every time step. Diameter clearances (for example g_{i} and g_{o}) are set assuming the bodies perfectly centered with respect to their rotation axes while the axial clearance (g_{a}) is defined as equally distributed among front and back sides of the gears.

In reality, this assumption is not always true because pressure unbalance in both axial and radial directions will displace the gears from their nominal position. Limitations in the representation of this phenomenon will affect the final results, especially those concerning the mechanical viscous losses.

3.4 Design verification and preliminary assessment

In the design phase of the hydraulic pump, it is useful and helpful to obtain some indications in advance from other similar products. For this purpose, a commercial Parker MGG20030 Hydraulic Motor with a displacement of 11.471 cm^3/rev is chosen and its hydro-mechanical properties are investigated.

The chosen pump together with its disassembled components are shown in Fig.3.10, from which it is clear to see that the chosen pump adopts a gerotor layout and the inner gear has 6 teeth while the outer one has 7. Other relevant parameters are measured precisely and reported in Tab.3.3. These parameters will be used to rebuild the CAD model of the hydraulic pump and used for the CFD simulations.

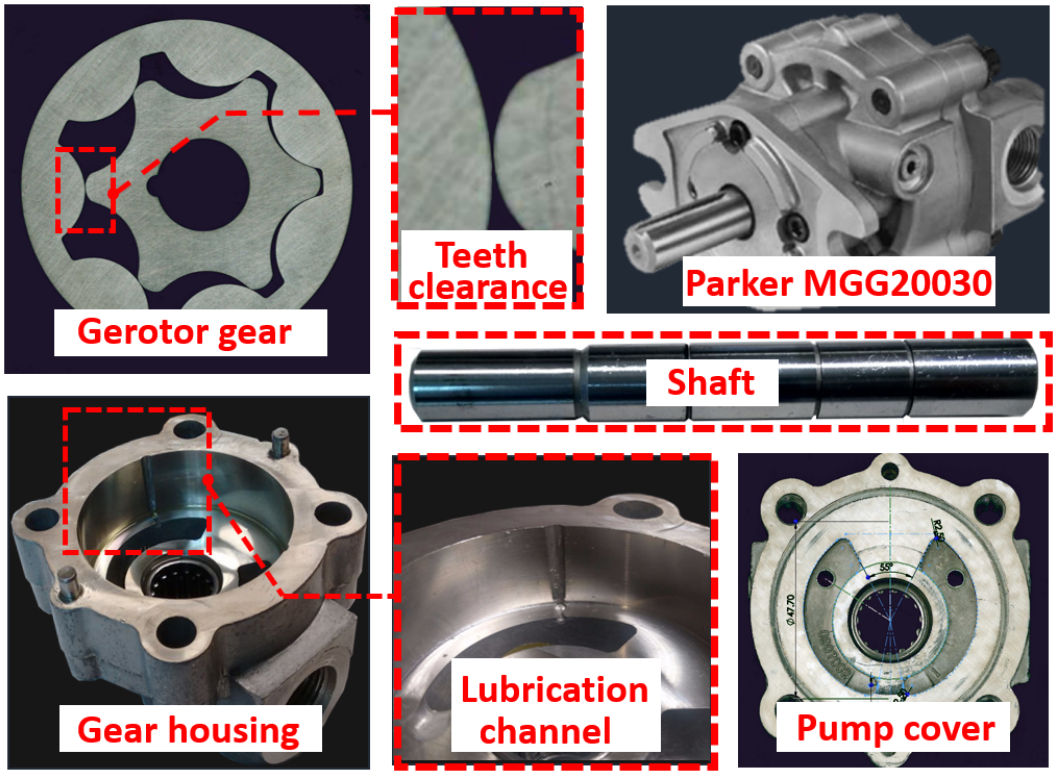

Fig. 3.10 Disassembled components of Parker Hydraulic Motor MGG20030

Fig.3.11 shows the Parker pump characterization curve from their datasheet [21], and this characterization curve will be used to compare with the simulation results from the CFD analysis. Particularly, the simulations are carried out with two kinematic viscosities indicated in the datasheet as nominal (32cSt) and minimum (13 cSt) values. The fluid density is assumed as 836 kg/m^3, while the bulk modulus is set to be 2.15 GPa.

It is worth to point out that to account for viscous losses, the outer gear ring and the gear faces were set to rotate. Since the gear faces are knitted into a single surface, the surface was set to rotate with the speed and center of rotation of the outer gear. This will lead to a small error in the estimation since the inner gear is rotating 7/6 faster and its center of rotation is eccentric. However, it is expected that the drag

Table 3.3 Design parameters of Parker Hydraulic Motor MGG20030

Design parameter	**Description**	**Value [mm]**
N_g	Number of inner gear teeth	6
R_{1o}	Outer gear outside radius	28.552
R_{1l}	Outer gear lobe radius	9.7
R_{1r}	Outer gear root radius	0.7
R_{1b}	Outer gear base radius	23.54
R_{2o}	Inner gear outside radius	20.252
R_{2i}	Inner gear inside radius	7.945
e_g	Eccentricity	2.8
g_t	Inter-teeth clearance	0.04
l_g	Gear length	19.132
R_c	Case pocket radius	28.592
l_c	Case pocket depth	19.15
R_s	Shaft radius	7.935

in the inner gear is much lower than the one in the outer gear. Hence, the initial assumption is still valid.

The comparison between the results from CFD simulation and the datasheet can be found in Fig.3.12. From the result, it is observed that within a certain range of speed (for example from 1.7 krpm to 3.2 krpm), the CFD simulation results can be assumed as accurate when compared with the datasheet value while at some other regions, the error may become more evident.

However, there are many reasons to explain this observation, for instance, the datasheet does not indicate the exact viscosity value during their characterization process. Furthermore, since viscosity may change its value with a temperature gradient, it is possible that the test starts at a viscosity higher than the nominal value and during the test, the increment of speed leads to a drop on the viscosity.

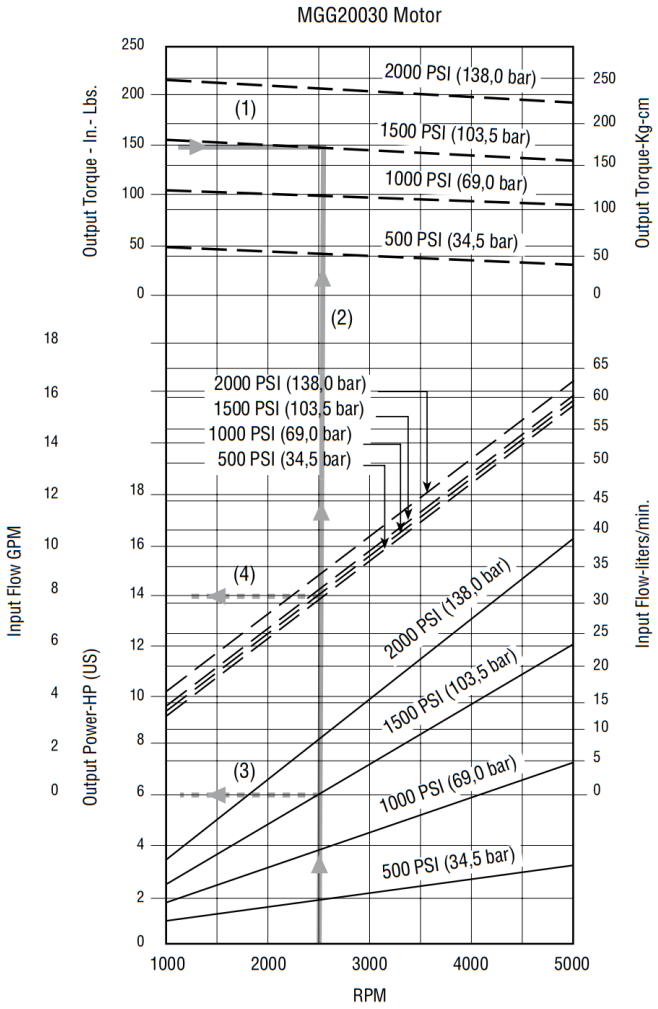

Fig. 3.11 Characterization curve of Parker Hydraulic Motor MGG20030 [21]

To solve this issue and further validate the CFD model to achieve a higher accuracy, an experimental test for characterizing the pump is designed and carried out in the lab. Fig.3.13 shows the test rig setup. Basically, the whole test rig can be separated in two functional regions which are known as driving stage and driven stage. The driving stage consists of a Kollmorgen Electric Motor which is controlled by the inverter to set different input speeds, and the motor is coupled with a MGG20030 Parker pump, while the driven stage has another identical Parker pump coupled with an PM electric machine which has its own power stage and different current commands (i_q) are given during the test. These two stages are connected with each other by means of hydraulic pipelines and since the two pumps are the

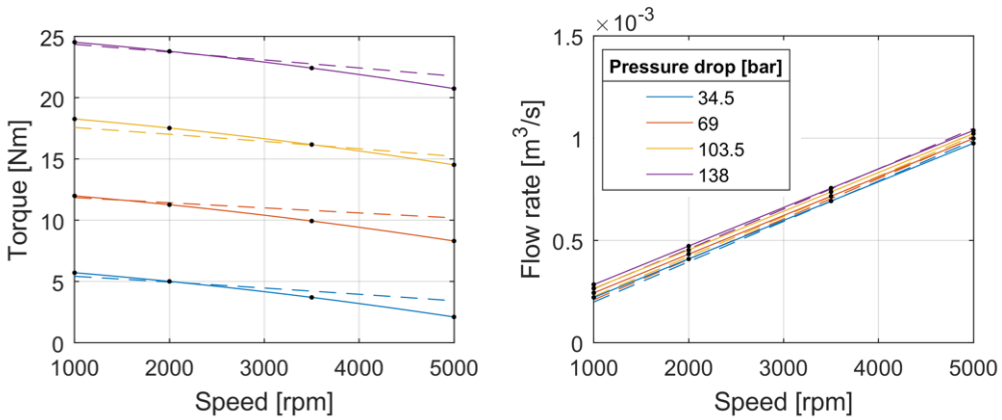

Fig. 3.12 Result comparison between CFD simulation and Parker datasheet.CFD simulations(dots) and their interpolations(solid), datasheet(dash)

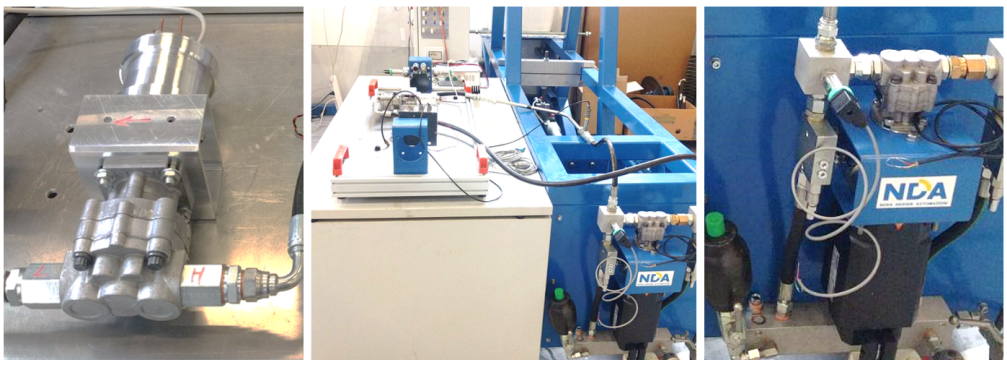

Fig. 3.13 Experimental test rig setup for Parker pump MGG20030

same, this system is assumed to present an unitary transmission ratio. Regarding the measurements, two pressure sensors are used to register the inlet and outlet port pressure, one flow meter is connected properly to read the oil flow rate and all these measurements are monitored and registered by the data acquisition system.

Unfortunately, due to some hardware issue, the measurements of the flow meter used in the test are not reliable for speeds above 2000 rpm, in this case the speed range was reduced (for example 500 rpm, 1000 rpm, 1500 rpm, 2000 rpm). And considering the power stage limitation at driven stage side, the chosen quadrature currents (i_q) are 0 A, 10 A, 20 A, 30 A, and 37 A. Then, the hydraulic (volumetric) and mechanical (hydro-mechanical) efficiencies can be calculated accordingly for each testing point and in the end, the results can be fitted afterwards to obtain a complete efficiency map.

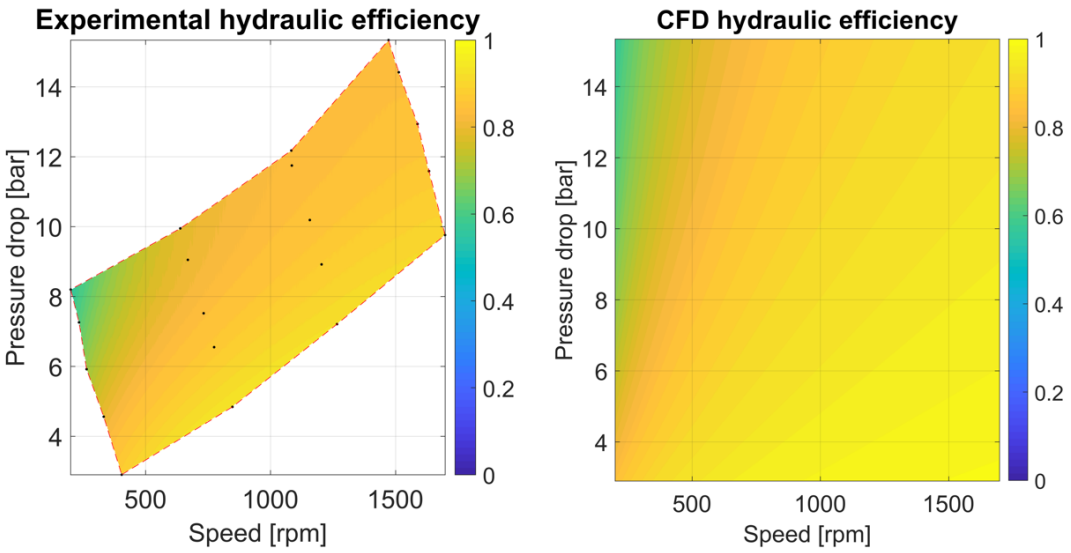

Fig. 3.14 Hydraulic efficiency comparison between experimental tests and CFD simulations

The results can be found in Fig.3.14 and Fig.3.15, from which it is observed that the error of mechanical efficiency is relatively large (with the absolute error 0.06 in hydraulic efficiency and 0.51 in mechanical efficiency) and this difference between the CFD and experiment must be related to those elements which are not modelled in the Finite Element (FE) simulator. One possible assumption could be related to the seal between the shaft and body of the pump.

To characterize this seal friction loss, first the external gear of the gerotor pump was removed and the pump was driven with the driving motor (Kollmorgen) at different speeds and pressures preloaded. The torque was estimated from the current yielded by the motor. To this torque, a (minimum) part due to the inner gear viscous drag was also subtracted. In this way, the friction loss due to the seal can be modelled by a second degree polynomial and this loss can be recovered from the mechanical losses to match the CFD simulations. The updated results are shown in Fig.3.16 and now the absolute error of mechanical efficiency has decreased from 0.51 to 0.11 which means a better coherency between the test and the model.

Noticed that when the set of quadrature currents (i_q) are applied to the electric motor, the estimated pressure drop lies in a range which is completely out of the working range of the Parker MGG20030 hydraulic motor that is claimed in the datasheet (Fig.3.11), which means this commercial system is not able to yield the efficiency we need. However, this pressure drop value fits more with the pumps which

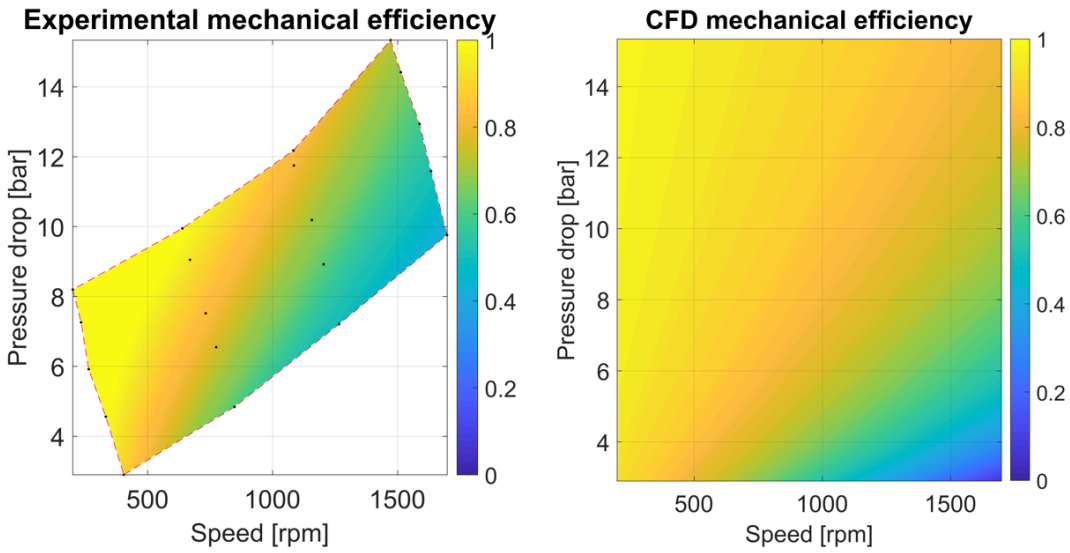

Fig. 3.15 Mechanical efficiency comparison between experimental tests and CFD simulations

have lower displacements, in this case, instead of using the commercial product, we modified the original Parker pump and developed a new system to integrate the motor and pump together inside a single case.

Based on the previous analysis, the target hydraulic pump yields a volumetric displacement of 3.6 cm^3/rev. Figure 3.17 shows the kinematic features of the designed pump. In this case, the selected profile yields a pulsation index of 4.36%.

To verify the design, the identified pump configuration was simulated at different working points and the results were interpolated to generate an efficiency map. Furthermore, if A_p is considered as the piston cross section, the map can be converted in the force-speed plane as shown in Fig. 3.18 through the equation below:

$$\begin{cases} F_p = A_p \Delta P_g \\ v_p = Q_g / A_p \end{cases} . \tag{3.19}$$

Noticed that the units in numerical and experimental plots have been normalized to protect proprietary data. However, force and speed values can be associated to the typical damping characteristics in the automotive field. The maximum force usually ranges from 1 to 4 kN, depending on the size of the vehicle, while the piston speed can reach up to 2 m/s.

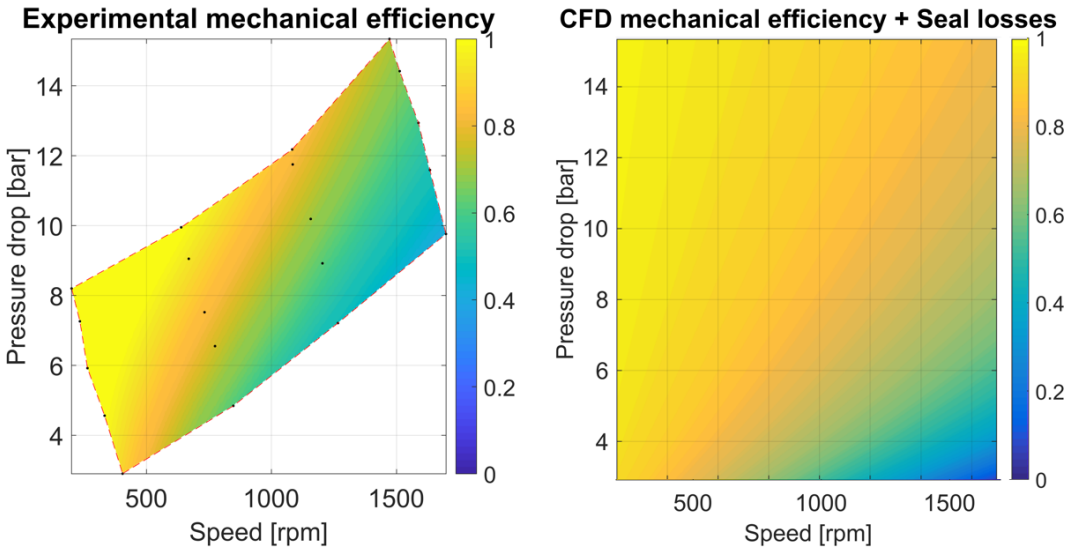

Fig. 3.16 Experimental test rig setup for Parker pump MGG20030

The behavior spans a relevant portion of the force-speed plane. Furthermore, the maximum damping coefficient specification $c_{\mathrm{p,max}}$ lies inside the obtained map, while the damping behavior due to hydro-mechanical losses can be linearized at low speed to obtain $c_{\mathrm{p,min}}$.

This result defines the design objective of the electric motor. The maximum rotary damping provided by the motor must counteract leakages and account for hydro-mechanical loss:

$$c_{\mathrm{sc}} = \frac{\tau^2}{\eta_{\mathrm{v}}} \left(c_{\mathrm{p,max}} - c_{\mathrm{p,min}} \right). \tag{3.20}$$

The selected design constraint yields a motor able to accomplish the damping task with the minimum footprint. Alternatively, it is possible to optimize the machine to match the maximum efficiency point of the pump map. However, this choice would potentially lead to a motor with larger geometric envelope.

A first set of simulations is devoted to assess the diameter clearances g_{i} and g_{o}. From the results, it is observed that the inside diameter clearance has no effect on both the volumetric and hydro-mechanical efficiency terms. Thus, g_{i} is selected to provide a tight fit without interference to minimize inner gear radial play, yet allowing its axial motion on the shaft for pressure balancing. The outside diameter

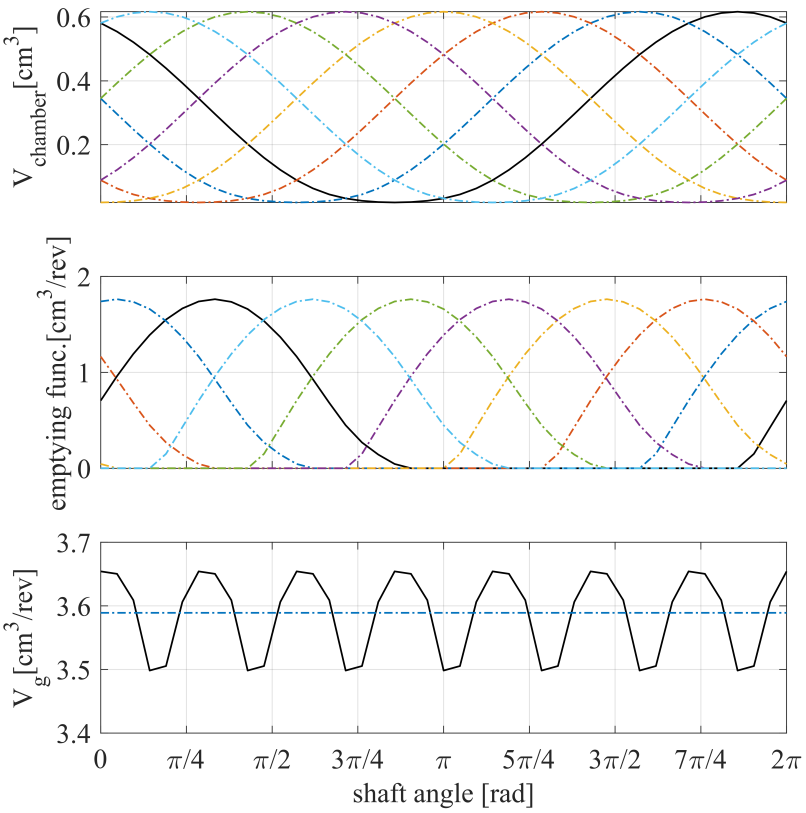

Fig. 3.17 Volumetric features of the designed pump. The volume and emptying function are plotted for chamber 0 (solid) and the remaining chambers (dash-dot). The volumetric displacement (solid) is compared to its average value (dash-dot).

clearance, instead, has a heavy influence on the hydro-mechanical losses, while volumetric ones are negligibly affected. This is expected, as the radial viscous drag torque on the outer gear is inversely proportional to g_o (Eq. 3.14). More importantly, the selection of g_o must consider the creation of a thin fluid film to lubricate and support the outer gear under pressure load.

Subsequently, a sensitivity analysis was carried out to understand the optimal axial clearance of the gerotor unit. Models with different axial clearances were simulated with two angular speeds. For each speed, three damping coefficients spanning a portion of the damping envelope were selected. Accordingly, the pressure drops were calculated following the ideal expression

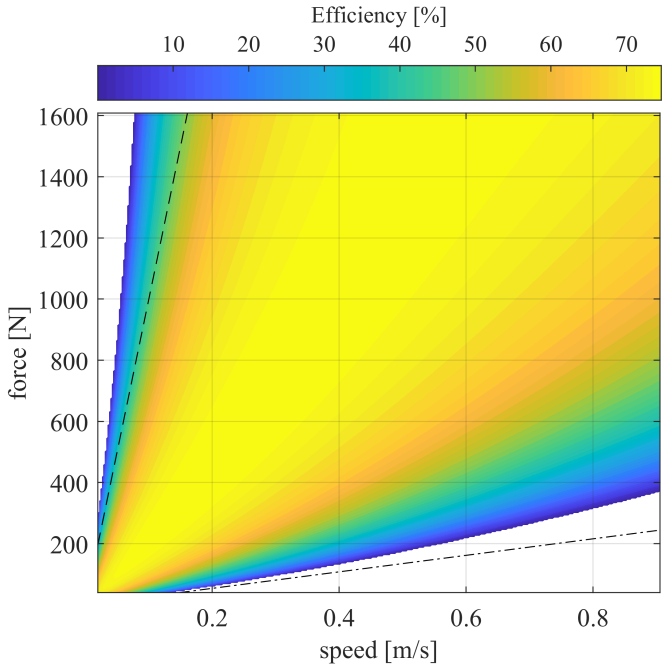

Fig. 3.18 Hydraulic pump efficiency map in the force-speed plane. Maximum damping behavior $c_{\mathrm{p,max}}$ (dashed) and damping behavior due to hydro-mechanical losses $c_{\mathrm{p,min}}$ (dash-dot) linearized for low speeds.

$$\Delta P_{\mathrm{g}} = \frac{\tau c_{\mathrm{p}} \Omega_{\mathrm{p}}}{A_{\mathrm{p}}} \tag{3.21}$$

Noticed that at high speed, the test with the highest damping yields a pressure drop that goes well beyond the design limit $\Delta P_{\mathrm{g,max}}$. Hence, this dataset was discarded.

The results are reported in Fig. 3.19 and Fig. 3.20. It is observed that the efficiency is a convex function of the axial clearance. Lower values favor volumetric over hydro-mechanical efficiency. On the contrary, large gaps reduce viscous drag at the cost of increasing internal leakages. The obtained results are helpful to define an axial clearance value in simultaneous agreement with all the selected working points.

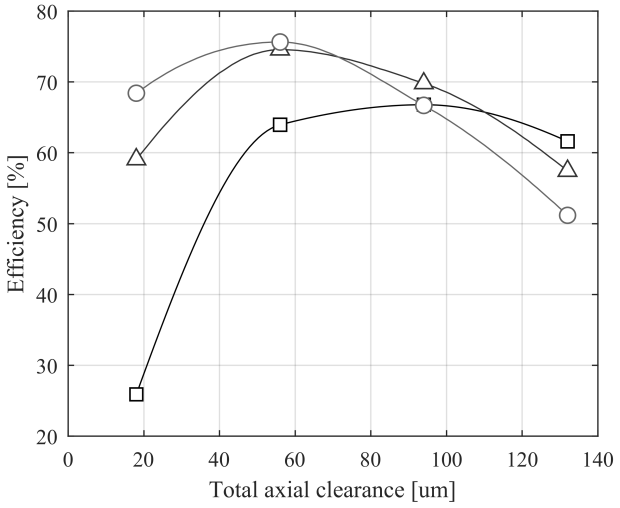

Fig. 3.19 Hydraulic pump efficiency with different total axial clearance values. Minimum angular speed, minimum (square), mild (triangle) and maximum (circle) damping coefficients. Results are interpolated with a piecewise-cubic function (solid).

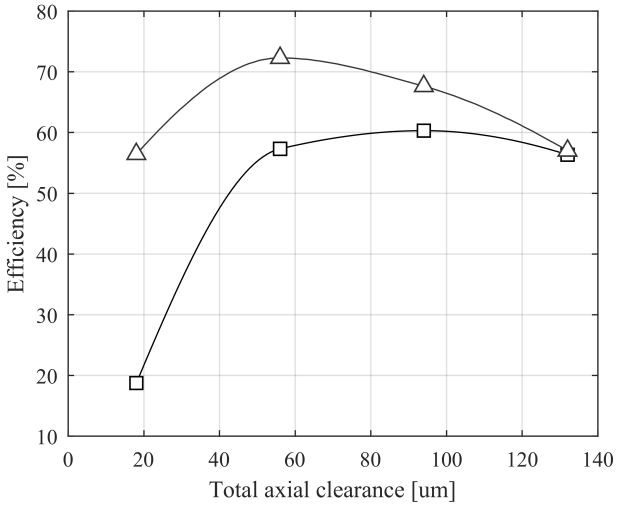

Fig. 3.20 Hydraulic pump efficiency with different total axial clearance values. Maximum angular speed, minimum (square) and mild (triangle) damping coefficients. Results are interpolated with a piecewise-cubic function (solid).

Chapter 4

Electric Machine Design

As mentioned in the end of last chapter, the electric machine should be designed to comply with the damping specification when the system is in short circuit as shown in Eq.3.20, under this condition, it means that there will be no additional active power for the electric machine to perform the damping specifications.

Fig.4.1 shows the electric machine design work-flow, basically, the process can be divided into three parts: magnetic design, winding design and design assessment. The magnetic design aims to maximize the torque delivered by the electric motor at a maximum slot current density (RMS value). The winding design aims to select a suitable coil arrangement to match the limitations of the inverter (i.e.maximum voltage). At last, the proposed design will be assessed and validated by thermal and lumped-parameter models.

Considering the layout of the electric machine, both slotted and slotless configurations are able to yield the damping requirement. However, through a preliminary analysis, the slotted configuration can exhibit a higher efficiency, which, in turn, leads to a larger power harvesting and better thermal performance than the slotless one. As a result, the slotted configuration is chosen and investigated in the following design.

Furthermore, a brushless permanent-magnet (PM) topology is advantageous to maximize the torque-to-mass ratio. Specifically, the design targets an inner rotor, radial flux, surface-mounted PM motor due to its construction simplicity. A fractional-slot profile is also adopted to reduce the Joule losses and cogging torque [109].

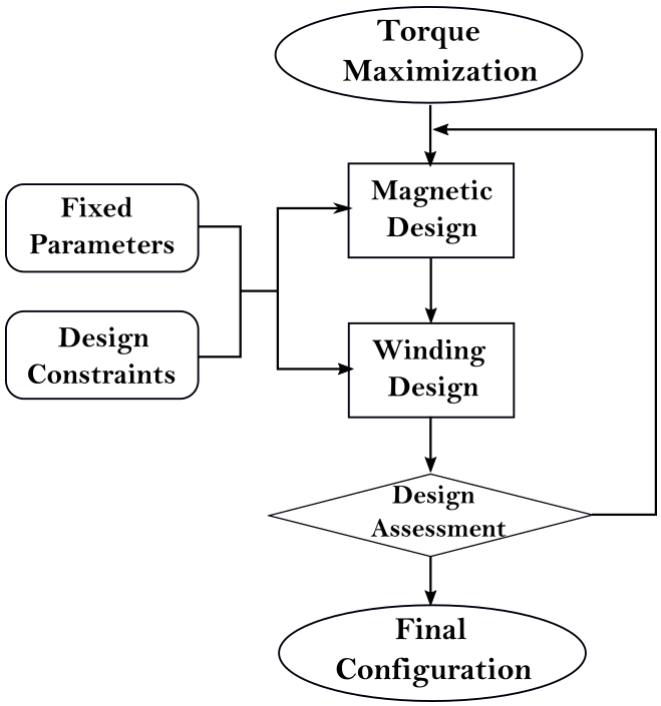

Fig. 4.1 Electric machine design work-flow

4.1 Electromagnetic Design

As shown in Fig.4.2, the electric machine adopts a slotted inner rotor configuration. Specifically, the stator is laminated and devised with M270-35A steel, it shows an outside radius R_{so}, a back iron radius R_{si}, and the width of each tooth is indicated by w_{t}. While the inner rotor can be seen as a hollow cylinder which is made of soft iron with its outer radius R_{ro} and inner radius R_{ri}. A number of permanent magnets (PM) made in NdFeB of grade N45SH are equally spaced on the circumferences of the soft iron part by means of gluing. R_{m} represents the overall radius of the rotor including magnets, the air gap g describes the distance between the tooth tip and the surface of the magnets.

Since the electric machine and hydraulic pump will be integrated together as a unit group, from the geometry point of view, the outside diameter of the stator should be constrained in order to match the cross section of the pump. Therefore, a number of design parameters which listed in Tab.4.1 which can be considered as fixed when the pump is fully designed, while other parameters that can vary their values will be defined through an optimization process afterwards.

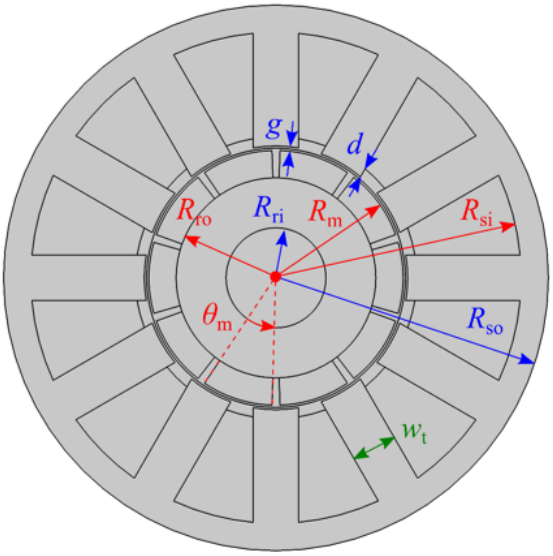

Fig. 4.2 2D geometry of the electric machine

These parameters which can vary their values can be called as independent variables such as the rotor outside radius R_{ro}, the magnet outside radius R_m, stator inside radius R_{si} and the magnet pitch α_m, which is defined as:

$$\alpha_m = \frac{N_m \theta_m}{2\pi} \tag{4.1}$$

where θ_m corresponds to the central angle of one single magnet as shown in Fig.4.2.

To achieve a feasible design, several constraints must be set to bound these variables, i.e.

- *Geometric consistency*:

$$R_{ri} < R_{ro} < R_m < R_{si} < R_{so}, \tag{4.2}$$

- *Magnet pitch bounds*:

$$0 < \alpha_m < 1, \tag{4.3}$$

- *Back iron linearity*:

$$\bar{B_{bi}} < B_{sat}, \tag{4.4}$$

where $\bar{B_{bi}}$ represents the magnetic flux density inside the stator back iron.

Table 4.1 Parameters for electric machine design

Symbol	Description	Value
B_{r}	Magnet remanent flux density	1.3 T
B_{sat}	Iron saturation flux density	1.2-1.8 T
d	Tooth tip to winding gap	1 mm
g	Air gap	0.5 mm
$J_{\mathrm{w}}^{\mathrm{RMS}}$	Maximum wire current density (RMS)	6 $\mathrm{A/mm^2}$
k_{cp}	Coil packing factor	0.3
l_{m}	Active length	22 mm
N_{m}	Number of magnets	10
N_{s}	Number of slots	12
R_{ri}	Rotor inside radius	4 mm
R_{so}	Stator outer radius	35 mm

- *Tooth overlap constraint*:

$$\frac{2\pi}{N_{\mathrm{s}}} > 2\arcsin\frac{w_{\mathrm{t}}}{2(R_{\mathrm{m}}+g)}, \tag{4.5}$$

where w_{t} indicates the tooth width and it is defined as:

$$w_{\mathrm{t}} = 2\frac{N_{\mathrm{m}}}{N_{\mathrm{s}}}(R_{\mathrm{so}} - R_{\mathrm{si}}). \tag{4.6}$$

To find the optimum values for these variables, the process may need a number of iterations. According to [110], for electric motor design procedure, the author provides a starting point in the definition of the machine's 2D geometry by optimizing the PM flux paths and the torque per unit length. To do this, the embedded AC/DC module in the software COMSOL Multiphysics is applied, and the 2D design can be refined through magnetostatic finite-element analysis (FEA) models. The obtained FEA results for the designed motor are shown in Fig.4.3.

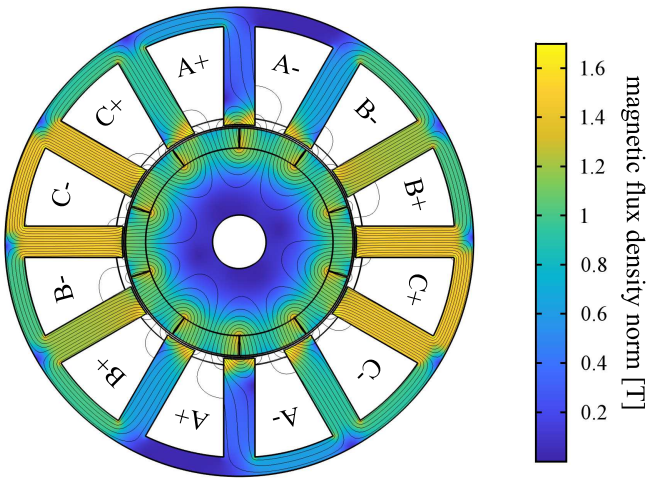

Fig. 4.3 Electric machine magnetostatic FEA results. The color map denotes the magnetic flux density norm, whereas the contours belong to the magnetic vector potential. The letters and signs indicate the winding phase and direction.

Once the motor cross section layout is obtained, the active length can be determined accordingly to match the target damping requirement. The damping coefficient imposed by the electric machine [11] is ideally expressed as:

$$c = \frac{K_\mathrm{t} K_\mathrm{e}}{\tau^2 (R + R_\mathrm{ext})} \tag{4.7}$$

where K_t is the torque constant of the electric motor, K_e is the back electromotive force (EMF) constant, R is the phase resistance and R_ext indicates the impedance imposed by the power stage output. Furthermore, the maximum attainable damping or the short-circuit rotary damping coefficient of the machine is a particular case of Eq.4.7 ($R_\mathrm{ext} = 0$ and $\tau = 1$). For a brushless PM motor, its short-circuit damping coefficient can be expressed as:

$$c_\mathrm{sc} = \frac{3 p^2 \lambda_\mathrm{p}^2}{2R}. \tag{4.8}$$

where p is the number of pole pair and λ_p is the PM flux linkage amplitude.

Assuming that each motor phase consists of N_c coils in series, each coil has N_t turns with an active length l_m, located inside slots with a cross section area A_s. The

PM flux linkage is calculated from the magnetic vector potential component $\mathscr{A}_z$ ortogonal to A_s:

$$\lambda_p = \frac{N_c N_t p l_m}{A_s} \left(\int_{A_s^+} \mathscr{A}_z dA - \int_{A_s^-} \mathscr{A}_z dA \right). \tag{4.9}$$

The superscript signs are used to denote the winding direction. Since the magnetic vector potential $\mathscr{A}_z$ does not depend on the number of turns per coil or active length, Eq. 4.9 can be rewritten as:

$$\lambda_p = K_\lambda N_t l_m, \tag{4.10}$$

where the PM flux per unit length constant K_λ depends on the established 2D geometry layout.

The phase resistance R can be calculated by:

$$R = \frac{2 N_c N_t \rho_{Cu}}{A_w} (l_m + l_{et}), \tag{4.11}$$

where ρ_{Cu} is the copper resistivity with a value of 1.6e-4 Ωm and l_{et} represents the end-turn length of the coil which remains outside of the slots. The wire cross section area A_w can be expressed in terms of the slot area and the coil packing factor k_{cp}:

$$A_w = \frac{k_{cp} A_s}{N_t} \tag{4.12}$$

Substituting Eq. 4.10 and Eq.4.11 into Eq.4.8 yields

$$c_{sc} = \frac{3 p^2 N_c k_{cp} K_\lambda^2 A_s}{4 \rho_{Cu}} \left(\frac{l_m^2}{l_m + l_{et}} \right), \tag{4.13}$$

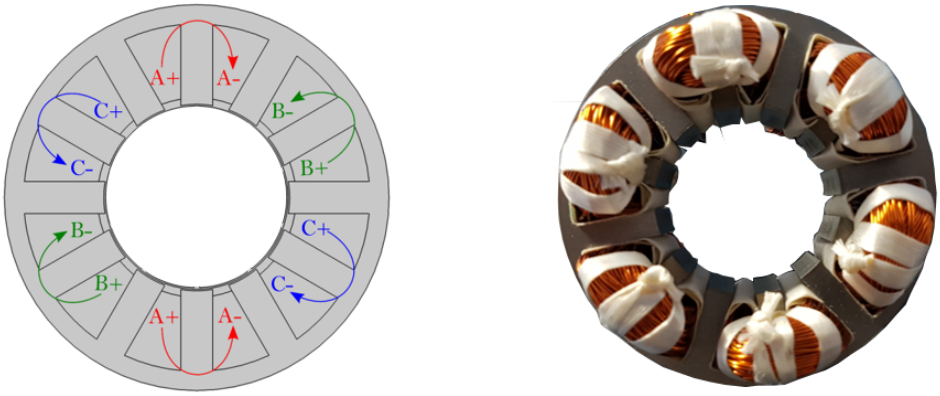

Fig. 4.4 Winding distribution layout(left) and stator winding prototype(right).

in which, it is observed that the active length of the machine l_{m} can be determined by using the constraint of c_{sc}.

4.2 Winding Design

Winding construction is another important aspect in the electric machine design, in particular, a fractional-slot winding layout is used as shown in Fig.4.4. Compared with other types of winding configurations, a fractional-slot winding can provide several advantages such as reduced mutual coupling among the phases, reduced end–turn winding lengths, lower torque ripple, and lower manufacturing cost.

Some of the winding design parameters can be extracted directly from the FEA results, for example, the coil cross section area A_{s}, and the end-turn length l_{et}. While others such as the phase flux ϕ can be described as a function of the magnetic vector potential $\mathscr{A}_{\mathrm{z}}$ to estimate the coil inductance.

$$\phi = \frac{l_{\mathrm{m}}}{A_{\mathrm{s}}}\left(\int_{A_{\mathrm{s}}^{+}} \mathscr{A}_{\mathrm{z}} dA - \int_{A_{\mathrm{s}}^{-}} \mathscr{A}_{\mathrm{z}} dA\right) \tag{4.14}$$

Furthermore, K_{J} is used to represent the motor torque to current density (RMS value) ratio which can be defined as:

$$K_{\mathrm{J}} = \frac{T_{\mathrm{mot}}}{\sqrt{2} J_{\mathrm{w}}^{\mathrm{RMS}}} \tag{4.15}$$

subsequently, the common used parameter (motor torque constant) K_t can be expressed by K_J and the wire cross section area A_w through:

$$K_t = \frac{K_J}{A_w} \tag{4.16}$$

whereas, the other parameter (back EMF constant) K_e is defined as:

$$K_e = \frac{2}{3} K_t \tag{4.17}$$

Considering the *Phase-to-Phase* voltage amplitude constraint:

$$\sqrt{3} K_e \Omega_{max} \leq V_{dc} \tag{4.18}$$

specifically, considering the limit condition and substituting Eq. 4.16 and Eq. 4.17 in Eq. 4.18, A_w can be expressed as:

$$A_w = \frac{2 K_J \Omega_{max}}{\sqrt{3} V_{dc}} \tag{4.19}$$

Furthermore, noticed that the number of turns per coil N_t should be an integer number to give a physical meaning and therefore, it can be computed by:

$$N_t = \text{int}(\frac{k_{cp} A_s}{A_w}) \tag{4.20}$$

To be more realistic and accurate, the value of A_w should be updated by the new integer number N_t using Eq.4.12, and similarly, the phase resistance R need to be recalculated accordingly in Eq.4.11.

From the power supply limitation point of view, the value of N_t should also satisfy the constraint for the battery on board, particularly, in the proposed design, the DC bus voltage is limited to 48 V which is intended to coherent with the mild hybrid standard and the electric machine EMF should not exceed this value for safety reasons. Hence, the DC bus voltage V_{dc} can be expressed by:

$$V_{dc} = \sqrt{3} p \lambda_p \Omega_{max}, \tag{4.21}$$

where λ_p is a function of N_t as shown in Eq. 4.10.

4.3 Thermal Analysis

To guarantee the proposed electric machine can work properly even in some strict working conditions, a stationary analysis was carried out to further assess the obtained design.

To accomplish this task, a worst-case-scenario was simulated with the aid of the software Motor-CAD, which is used by major motor manufacturers and universities worldwide. This software is based on lumped-parameter thermal network (LPTN) models, it provides the ability to perform electromagnetic and thermal analysis on electric machine designs. Accurate calculation results regarding the electromagnetic and thermal analysis can be obtained quickly with low-computation effort. Therefore, it is a very powerful and efficient tool in designing electromagnetic product. Moreover, the problem formulation requires the machine and winding geometry, the power losses and a working duty cycle.

The power losses are calculated when the electric machine works as a generator. Joule losses are computed through phase resistance. Iron and PM losses are obtained by implementing the discretized Berttotti equations [111] in a dedicated FEA model. Different combinations of current and speed are applied to the electric motor as input. The resulting efficiency map of the electric machine is plotted in Fig. 4.5. From the result, it is observed that Joule losses are dominative at low angular speed and high current region, whilst, iron and PM losses take place predominantly at high speed and low current area.

Considering the simulation setup, the thermal test is carried out within a quarter car model running on an ISO C road profile with a speed of 120 km/h, the system is set with the maximum damping under an initial temperature of 60 °C. The motor is rotating at a predefined speed and air is taken as the only outside fluid with natural convection and the inside fluid is the engine oil which is circulated by the rotor, its flow rate can be calculated by the volumetric displacement of the hydraulic pump and the average motor speed. Furthermore, the fluid flows exclusively through the air gap, the copper losses are calculated by the winding currents while other types of losses are neglected in this simulation.

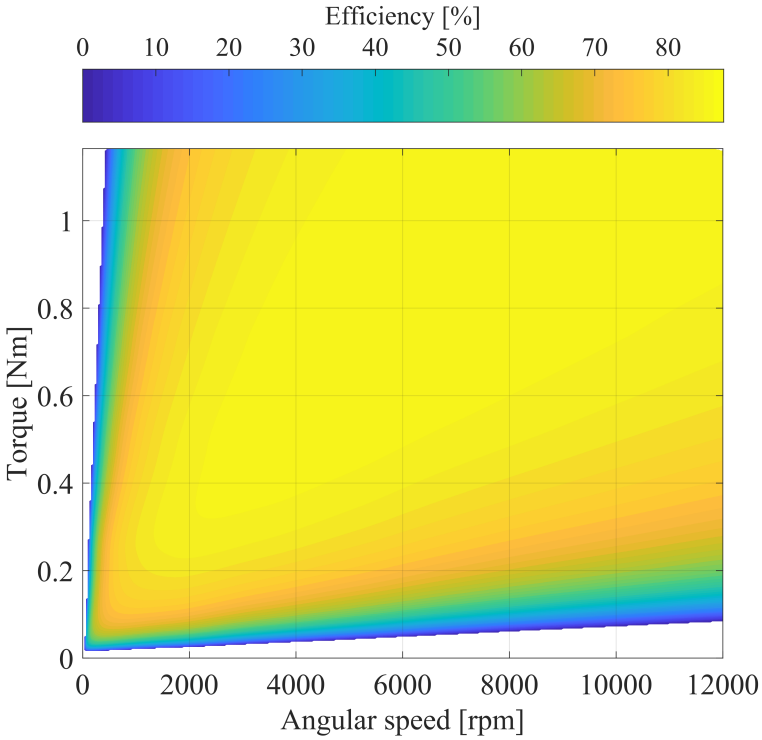

Fig. 4.5 Efficiency map of the electric machine working as a generator.

The stationary simulation result from Motor-CAD can be seen in Fig.4.6 shows the transient result of the hot spots inside the winding.

To assess the duty cycle performance of the motor-pump unit, a quarter car model is built using the parameters from the proposed design [101] in Simulink. The motor is assumed in short circuit to have maximum dissipation in the stator winding. Furthermore, suitable vehicle speed and road roughness are selected to reproduce a worst-case-scenario.

In the end, the average power dissipation and angular speed of the electric machine are extracted from Simulink. Motor-CAD is initialized with these data and the initial system temperature. The simulation result shows that the tested configuration is able to withstand the described working conditions because the two most critical points, i.e. the winding hotspot and the PM stay well below their temperature thresholds (see Table 4.2).

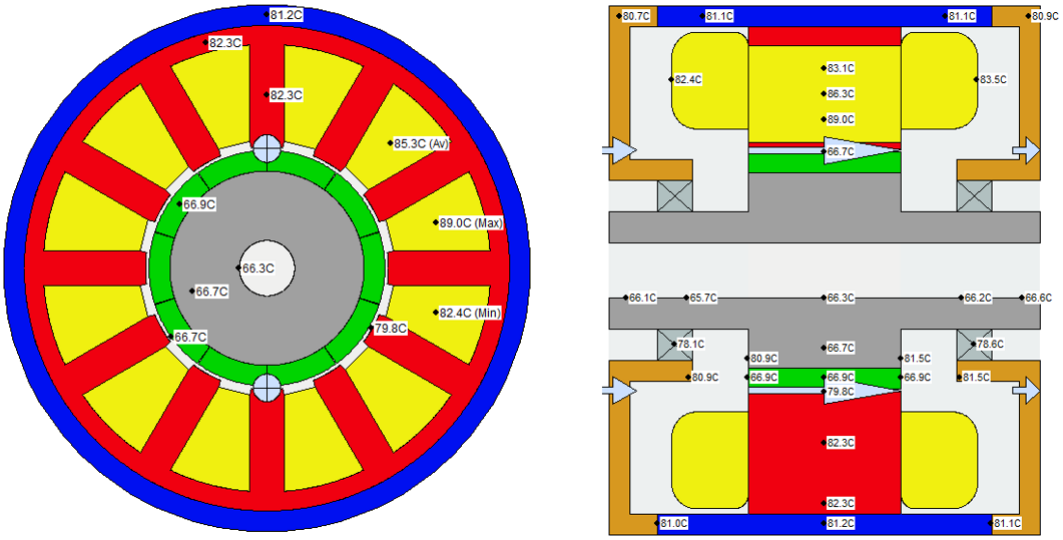

Fig. 4.6 Stationary thermal analysis result of the electric motor.

Table 4.2 Thermal simulation data.

Description	Symbol	Value	Unit
Initial system temperature	Θ_0	50	°C
Final winding hotspot temperature	Θ_c	137.7	°C
Winding temperature limit	$\Theta_{c,max}$	180	°C
Final PM temperature	Θ_p	123.5	°C
PM temperature limit	$\Theta_{p,max}$	150	°C

4.4 Mechanical Packaging

Fig.4.7 shows the structure layout of the motor-pump group, the casing separates hydraulic part (pump gears) and electric machine, the inner rotor of the gerotor is fixed on the same shaft of the electric machine and the torque can be transmitted from the pump gears to the latter component through a rectangular key. As we have discussed before, ten permanent magnets (thus five pole pairs) are glued onto the surface of the shaft which is supported by two ball bearings and one of them is axially preloaded by a wave spring and the stator of the electric machine is locked by a spacer between the casing and motor cover. A position sensor array is fixed on this cover and the sensor and phase wirings are brought outside through four sealing cable glands. The whole motor-pump group is oil-filled and the friction losses are minimized due to in this case the seal element between shaft and case is omitted and

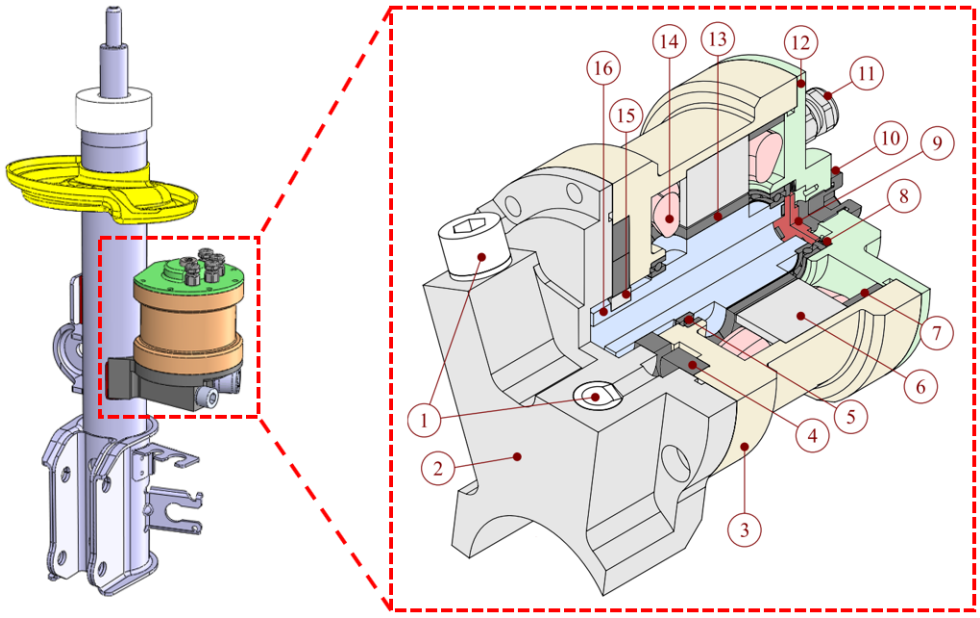

Fig. 4.7 Isometric cut view of the motor-pump unit. Pump port plugs (1), pump cover manifold (2), casing (3), gerotor gears (4), ball bearings [×2] (5), stator (6), motor spacer (7), wave spring (8), position sensor (9), drain cap (10), cable gland [×4] (11), motor cover (12), permanent magnet [×10] (13), winding coil [×6] (14), key (15), rotor shaft (16).

the final design of the prototype yielded a compact unit with a total length of 90 mm, maximum diameter of 88 mm and total mass of 3.5 kg. The main components of the prototype are shown in the Fig.4.8.

Table 4.3 Wall thickness calculation og the casing body

Parameters	**Values (100 bar)**	**Values (50 bar)**
Outside diameter D_o	76 mm	76 mm
Allowable stress S	51.7 MPa	51.7 MPa
Wall thickness t	7.3 mm	3.6 mm

The geometry of the design is affected by several constraints. On one hand, a compact designed with smaller size and less mass is always favored, on the other hand, the proposed design should provide desired performance and functionalities even under some critical working conditions. For example, the oil-filled device

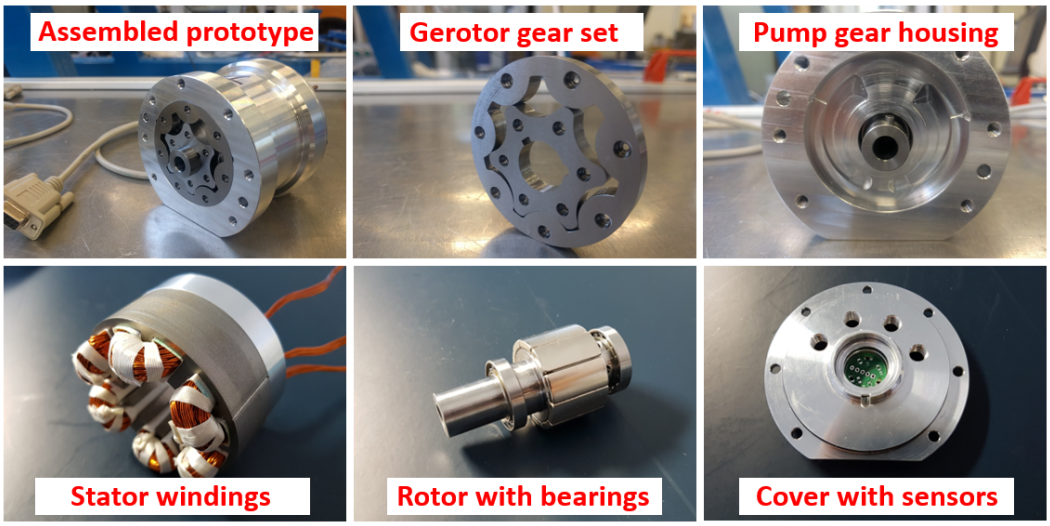

Fig. 4.8 Prototype assembly with main components in the proposed design.

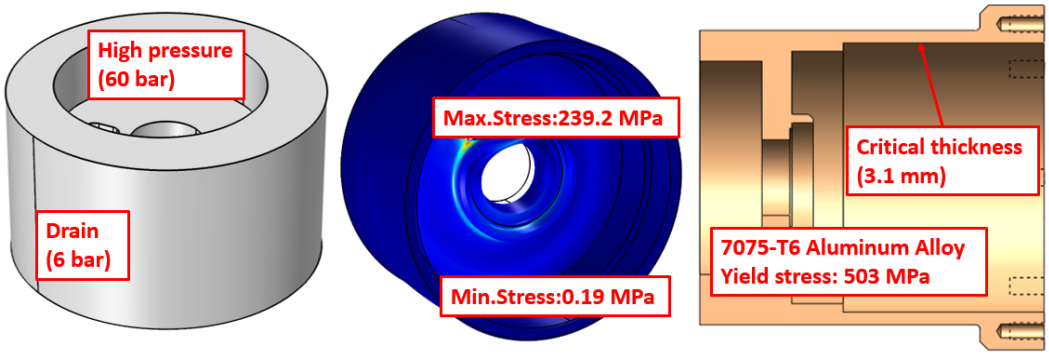

Fig. 4.9 Analysis for the prototype casing wall thickness.

should always be able to resist the internal pressure to guarantee a proper work, therefore, a wall thickness analysis is performed at this stage.

The wall thickness of a tube or pipe structure can be calculated by using *Barlow's formula*:

$$t = \frac{P_{\mathrm{i}} D_{\mathrm{o}}}{2S} \tag{4.22}$$

where P_{i} is the internal pressure, D_{o} indicates the tube outside diameter, and S represents the allowable stress. Tab.4.3 shows the results of thickness which are calculated based on the pressure rating values of 100 bars and 50 bars.

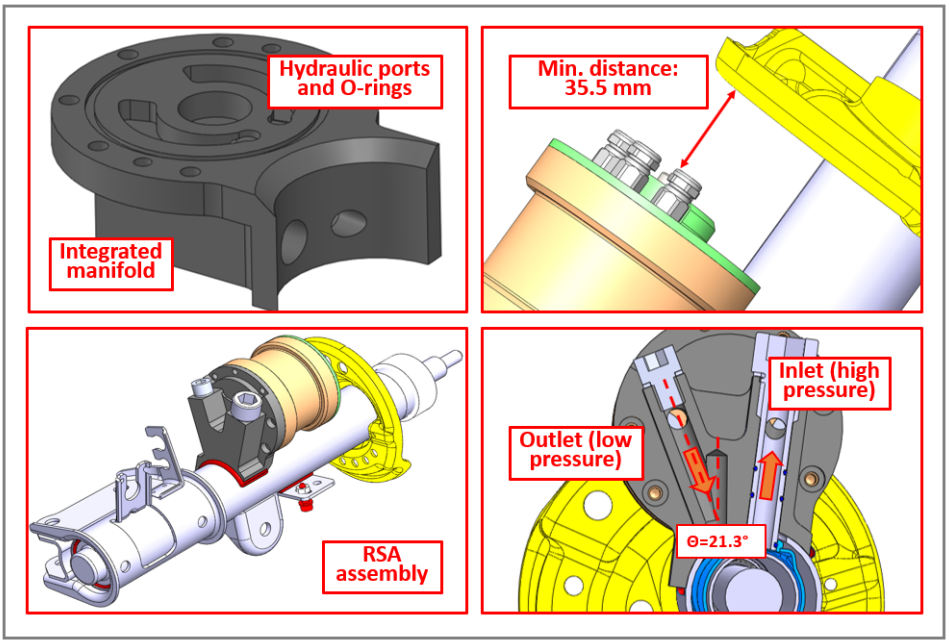

Fig. 4.10 Integrated shock absorber with motor-pump unit using manifold.

Specifically, in our proposed design, the casing body is made of 7075-T6 aluminum alloy which shows a yielding stress of 503 MPa. However, inside the motor-pump unit, the pressure will increase and reach a maximum value about 60 bars at the gerotor region. Then the pressure drops along the casing body and finally yields around 6 bars at the drain. In the end, the casing body shows a minimum wall thickness of 3.1 mm (corresponding to a pressure of 43 bar) which is sufficient to hold the pressure in that region. A FEM analysis is also performed to verify the design as shown in Fig.4.9.(No critical thickness values were found in the pump cover, hence, here only shows the FEM results of the casing part.)

To install the motor-pump unit on the shock absorber, a special designed manifold as shown in Fig.4.10 is used. Such manifold also has the function to close the system as a pump cover, therefore, the designed hydraulic ports are directly "duplicated" to the manifold (on the surface which contacted with the gears). And then, the closed device will be fixed to the damper body through welding. Furthermore, the motor-pump unit is placed in such a position that the axis of the unit is parallel with the axis of the shock absorber body. Axial and radial o-rings on the pump and motor side are also present to guarantee the fluid seal towards the exterior.

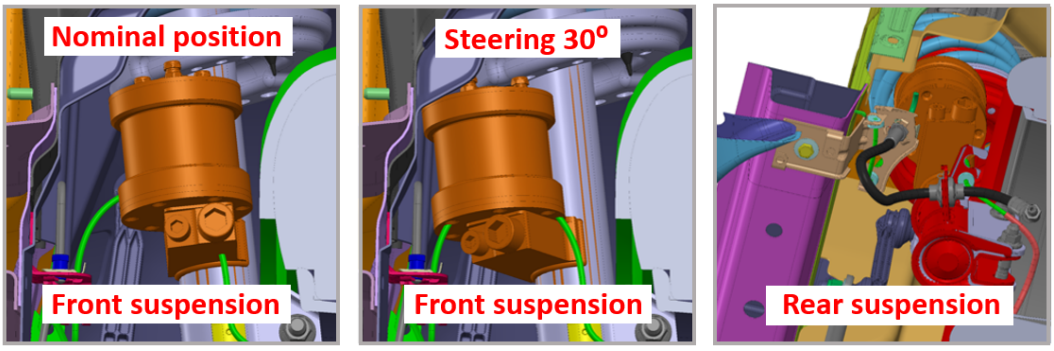

Fig. 4.11 Packaging check for the regenerative shock absorbers on the vehicle.

Depend on different states of the vehicle (in standstill or perform maneuvering such as steering), the position of the vehicle body is also different. Thus, it is necessary to have a packaging check before installing the complete regenerative shock absorber assembly on the vehicle. To do this, a Jeep Renegade SUV vehicle is taken as a reference. Specifically, the car is equipped with a R17 tire plus the snow chain (in worst-case scenario) as shown in Fig.4.11. The result from CAD analysis shows that with such arrangement, under each condition (front, rear, nominal, steering) there is no interference between the prototype and any other mechanical component in that region.

Chapter 5

Control strategy

To provide full-active functionality to the proposed design, a power stage with a three-phase bridge is adopted, the deigned electric machine will be controlled by the Field Oriented Control (FOC) algorithm, which can be considered as the most efficient and common control strategy for AC machines. Basicaly, FOC is based on three major points: the machine current and voltage space vectors, the transformation of a three phase speed and time dependent system into a two co-ordinate (dq co-ordinates) time invariant system and effective Pulse Width Modulation (PWM) pattern generation. Furthermore, two input references are needed for field orientated controlled machines: the torque component (aligned with the q co-ordinate) and the flux component (aligned with d co-ordinate).

5.1 Field Oriented Control for PMSM

5.1.1 Introduction to FOC algorithm

Fig.5.1 shows the conceptual layout of our control target, a brushless PMSM. In general, this type of motor has a wound stator, a permanent magnet rotor assembly together with some sensing devices (sensors) to detect the rotor position. Since the rotor excitation is given by the permanent magnets mounted onto the shaft, the produced flux and torque will depend on each other and stator current will be the only source that can be controlled.

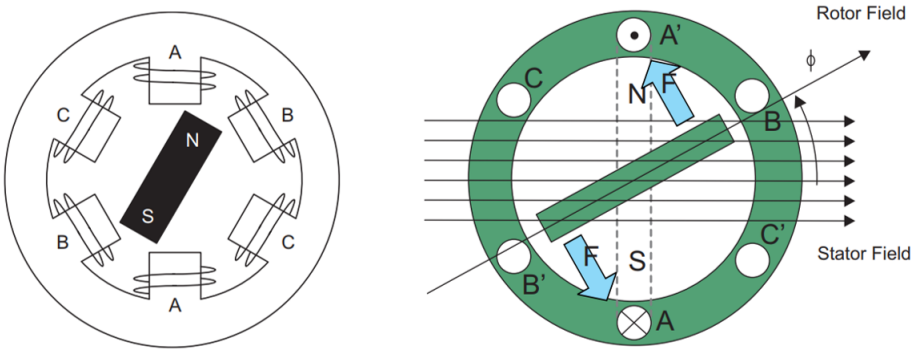

Fig. 5.1 Layout of PMSM with one pole pair illustrated in [22]

One of the common methods to control this type of machine is the so-called Field Oriented Control (FOC), a digital implementation which demonstrates the capability of performing direct torque control. Basically, by implementing such algorithm, microcontrollers will engage several mathematical transformations (Clarke, Park) to decouple the torque generation and the magnetization functions in PM motors.

According to the electromagnetic laws, the torque produced in the synchronous machine is equal to the vector cross product of the two existing magnetic fields:

$$\mathbf{T_{em}} = \tilde{\mathbf{B}}_{\mathbf{stator}} \times \tilde{\mathbf{B}}_{\mathbf{rotor}} \tag{5.1}$$

From the equation, it is obvious that the maximum torque is obtained when the stator and rotor magnetic fields are orthogonal. Therefore, the control target is to maintain the rotor and stator flux in quadrature.

Fig.5.2 summarizes the basic scheme of torque control with FOC algorithm. In particular, two motor phase currents are measured. These measurements feed the Clarke transformation module. The outputs of this projection are designated $i_{S\alpha}$ and $i_{S\beta}$ which are also the inputs of the Park transformation that provide the current in dq rotating reference frame. The i_{Sd} and i_{Sq} components are compared to the references i_{Sdref} (the flux reference) and i_{Sqref} (the torque reference). As in synchronous permanent magnet a motor, the rotor flux is fixed determined by the magnets; there is no need to create one. Hence, when controlling a PMSM, i_{Sdref} should be set to zero. The torque command i_{Sqref} could be the output of the speed regulator when using a speed FOC. The outputs of the current regulators are V_{Sdref} and V_{Sqref}; they are applied to the inverse Park transformation. The outputs of this

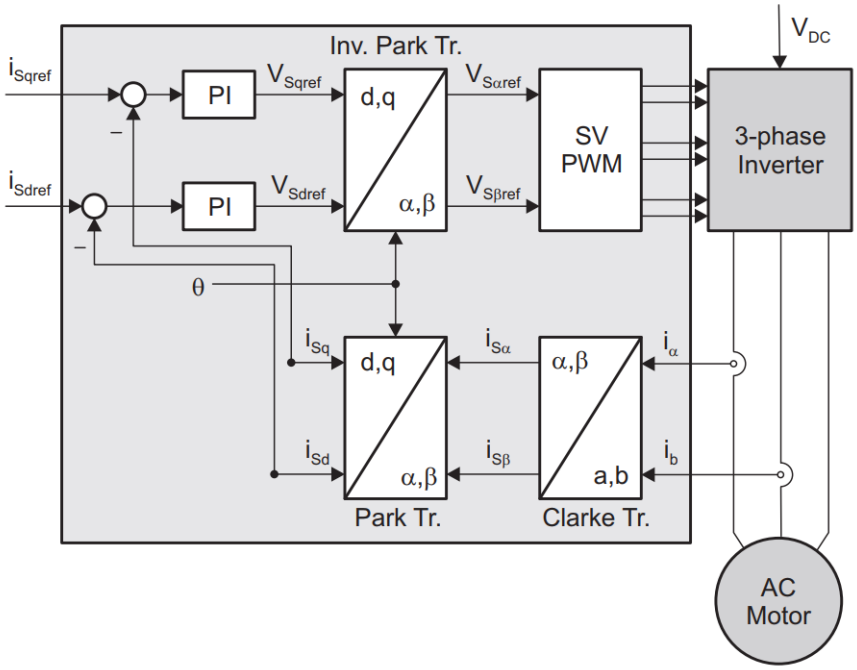

Fig. 5.2 Basic scheme of FOC illustrated in [22]

projection are $V_{S\alpha ref}$ and $V_{S\beta ref}$, which are the components of the stator vector voltage in the (α, β) stationary orthogonal reference frame. These are the inputs of the space vector PWM. The outputs of this block are the signals that drive the inverter.

Since FOC is simply based on projections, the control structure handles instantaneous electrical quantities. This makes the control accurate in every working operation (steady state and transient), leads to high dynamic performance in terms of response times and power conversion. While the mathematical transformations (Clarke, Park) will be described in detail in the next section.

5.1.2 Phase transformation in PMSM model

Fig.5.3 shows the layout of a single pole pair surface-mounted permanent-magnetic (SPM) motor with three phases a, b and c, and θ_e represents the electric angle of the rotating machine. Such motor yields the following dynamic equation:

$$\mathbf{v}_{abc} = \frac{\mathrm{d}}{\mathrm{d}t}\lambda_{abc} + \mathbf{R}_{abc}\mathbf{i}_{abc} \tag{5.2}$$

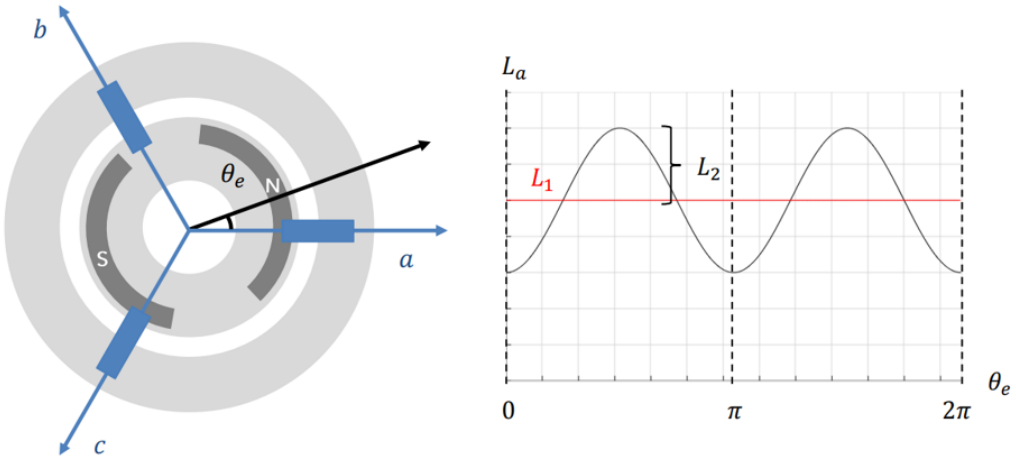

Fig. 5.3 Three-phase model of SPM motor and its inductance behavior

where $\mathbf{v}_{abc}$ and $\mathbf{i}_{abc}$ represent the voltage and current vectors. $\mathbf{R}_{abc}$ is the resistance matrix, λ_{abc} indicates the flux linkage vectors and it can be further defined as:

$$\lambda_{abc} = \mathbf{L}_{abc}\mathbf{i}_{abc} + \lambda_{p,abc} \tag{5.3}$$

in which, $\mathbf{L}_{abc}$ indicate the inductance matrix which contains the information of both auto inductance and mutual inductance (indicated by M, noticed that due to machine symmetry, the two mutual inductances between two phases should be equal $M_{ij} = M_{ji}$). while $\lambda_{p,abc}$ is the permanent-magnetic (PM) flux linkage vector.

In general, the auto inductance (i.e. L_a) of each phase shows a relationship with the angle θ_e as shown in Fig.5.3, the shape of the waveform is mainly due to the variable reluctance of the rotor along the circumferential direction. For example, when the angle is zero, the inductance path will go in the same direction which means the flux will go across the PM, since the permeability of PM is very low, the reluctance of the magnetic circuit is larger (inductance will be lower) and therefore, minimum inductance is obtained at zero degree. When the angle reaches 90 degrees, the inductance will go into a direction which the circuit shows minimum reluctance and maximum inductance. At 180 degrees, from the magnetic point of view, the machine is in the same condition as for zero degree and as a result, a repetition

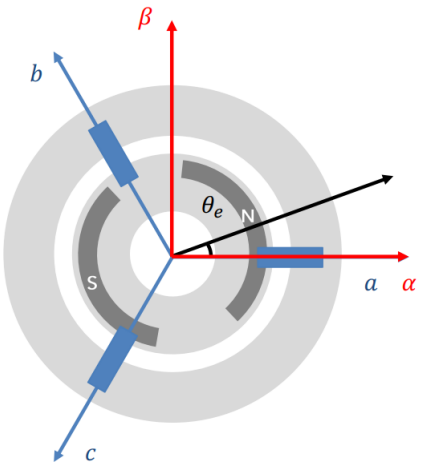

Fig. 5.4 Clarke transformation

pattern will be obtained, and the auto inductance can be expressed into a constant term L_1 plus a sinusoidal term L_2 that varies with two times the electric angle:

$$L_a = L_1 - L_2 \cos(2\theta_e) \tag{5.4}$$

In the case of SPM motors, the rotor can be considered as a perfectly cylindrical object. Since there is no anisotropy of the machine, the motor always shows the same reluctance and therefore, L_2 term will be vanished and yield a constant inductance value.

Clarke transformation

As mentioned before, the FOC is the control strategy that based on several mathematical transformations (Clarke and Park). These transforms will simplify the solution of the model equations and the control task.

The first transformation can convert any variables in the original three-phase system (abc) to the two-phase representation ($\alpha\beta 0$) which is fixed on the stator by implementing the Clarke transformation matrix $\mathbf{T}_c$.

$$\mathbf{v}_{\alpha\beta 0} = \mathbf{T}_c \mathbf{v}_{abc} \tag{5.5}$$

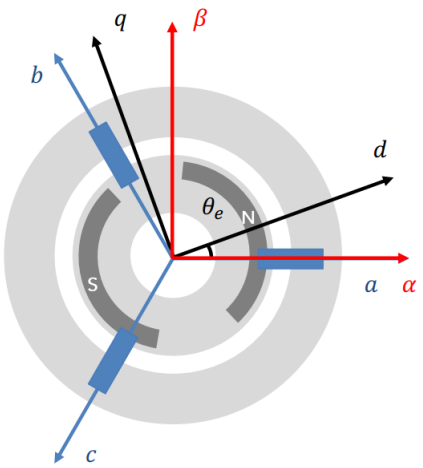

Fig. 5.5 Park transformation

$$\mathbf{T}_c = \frac{2}{3}\begin{bmatrix} 1 & -1/2 & -1/2 \\ 0 & \sqrt{3}/2 & -\sqrt{3}/2 \\ 1/2 & 1/2 & 1/2 \end{bmatrix} \tag{5.6}$$

As shown in Fig.5.4, the obtained phase α is in line with phase a, while there is a phase lag of $\pi/2$ between the phase α and β, and the third phase 0 will be null.

$$\mathbf{v}_{abc} = \begin{Bmatrix} V\cos\theta_e \\ V\cos(\theta_e - 2\pi/3) \\ V\cos(\theta_e + 2\pi/3) \end{Bmatrix} \leftrightarrow \mathbf{v}_{\alpha\beta 0} = \begin{Bmatrix} V\cos\theta_e \\ V\sin\theta_e \\ 0 \end{Bmatrix} \tag{5.7}$$

Furthermore, the resulting system shows that this transformation can preserve the magnitude of the signals (i.e.voltage,current,flux linkage), while to match the power terms, an additional factor 3/2 is needed.

$$P_{abc} = \frac{3}{2}P_{\alpha\beta 0} \tag{5.8}$$

Park transformation

As shown in Fig.5.5, the obtained two-phase system ($\alpha\beta 0$) can be further transformed to another reference frame system ($dq0$) which is fixed on the rotor and rotate

at the speed of the motor. This can be done by applying a simple rotation matrix or Park transformation matrix $\mathbf{T}_p$.

$$\mathbf{v}_{dq0} = \mathbf{T}_p \mathbf{v}_{\alpha\beta0} \tag{5.9}$$

$$\mathbf{T}_p = \begin{bmatrix} \cos\theta_e & \sin\theta_e & 0 \\ -\sin\theta_e & \cos\theta_e & 0 \\ 0 & 0 & 1 \end{bmatrix} \tag{5.10}$$

The resulting system will be easier to understand. Compared with the two-phase system fixed on the stator, after applying the Park transformation, the sinusoidal function of the angle becomes a constant meanwhile preserves the signal amplitude.(Eq.5.12 takes into account when there is a lag φ between the phases.)

$$\mathbf{v}_{\alpha\beta0} = \begin{Bmatrix} V\cos\theta_e \\ V\sin\theta_e \\ 0 \end{Bmatrix} \leftrightarrow \mathbf{v}_{dq0} = \begin{Bmatrix} V \\ 0 \\ 0 \end{Bmatrix} \tag{5.11}$$

$$\mathbf{v}_{\alpha\beta0} = \begin{Bmatrix} V\cos(\theta_e+\varphi) \\ V\sin(\theta_e+\varphi) \\ 0 \end{Bmatrix} \leftrightarrow \mathbf{v}_{dq0} = \begin{Bmatrix} V\cos\varphi \\ V\sin\varphi \\ 0 \end{Bmatrix} \tag{5.12}$$

abc-dq0 transformation

As shown in Fig.5.6, at this stage, a complete transformation matrix $\mathbf{T}_{pc}$ can be created by multiplying those two matrices $\mathbf{T}_c$ and $\mathbf{T}_p$ to transform from three-phase system (abc) to two-phase system ($dq0$).

$$\begin{cases} \mathbf{v}_{dq0} = \mathbf{T}_{pc}\mathbf{v}_{abc} \\ \mathbf{T}_{pc} = \mathbf{T}_p\mathbf{T}_c \end{cases} \tag{5.13}$$

$$\mathbf{T}_{pc} = \frac{2}{3}\begin{bmatrix} \cos\theta_e & \cos(\theta_e-2\pi/3) & \cos(\theta_e+2\pi/3) \\ -\sin\theta_e & -\sin(\theta_e-2\pi/3) & -\sin(\theta_e+2\pi/3) \\ 1/2 & 1/2 & 1/2 \end{bmatrix} \tag{5.14}$$

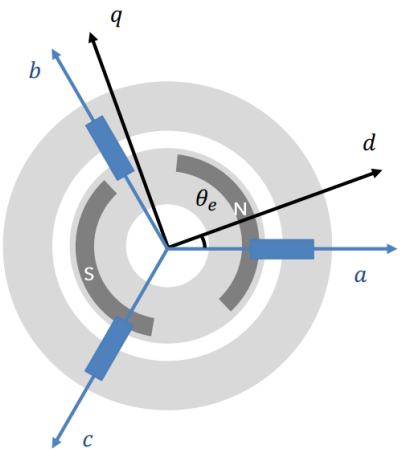

Fig. 5.6 **abc** – **dq0** transformation

If apply this transformation matrix to the machine dynamic equations (Eq.5.2 and Eq.5.3) in three-phase domain, the two-phase representation of equations will be obtained accordingly.

$$\mathbf{v}_{dq0} = \mathbf{T}_{pc}\frac{\mathrm{d}}{\mathrm{d}t}(\mathbf{L}_{abc}\mathbf{T}_{pc}^{-1}\mathbf{i}_{dq0} + \lambda_{p,abc}) + \mathbf{T}_{pc}\mathbf{R}_{abc}\mathbf{T}_{pc}^{-1}\mathbf{i}_{dq0} \tag{5.15}$$

$$\begin{aligned}\begin{Bmatrix} v_d \\ v_q \end{Bmatrix} = &\begin{bmatrix} \frac{3}{2}(L_1 - L_2) & 0 \\ 0 & \frac{3}{2}(L_1 - L_2) \end{bmatrix} \frac{\mathrm{d}}{\mathrm{d}t} \begin{Bmatrix} i_d \\ i_q \end{Bmatrix} \\ &+ \begin{bmatrix} 0 & -\frac{3}{2}(L_1 + L_2) \\ \frac{3}{2}(L_1 - L_2) & 0 \end{bmatrix} \Omega_e \begin{Bmatrix} i_d \\ i_q \end{Bmatrix} + \begin{Bmatrix} 0 \\ \lambda_p \end{Bmatrix} \Omega_e + R \begin{Bmatrix} i_d \\ i_q \end{Bmatrix}\end{aligned} \tag{5.16}$$

As shown in the model, the final voltage terms can be expressed by using two inductance terms which affect the derivative and value of currents together with the speed, the PM flux linkage term (back-EMF of the motor) and finally, the Joule losses.

$$\begin{cases} L_d = \frac{3}{2}(L_1 - L_2) \\ L_q = \frac{3}{2}(L_1 + L_2) \end{cases} \tag{5.17}$$

Furthermore, Eq.5.17 defines the inductances in the d and q axes respectively. L_d depends on the minimum inductance (the difference between the constant term

L_1 and the amplitude of the sinusoidal term L_2) while L_q depends on the maximum inductance (or the sum of L_1 and L_2).

By substituting L_d and L_q, the representation can be simplified as:

$$\begin{cases} v_d = L_d \frac{\mathrm{d}i_d}{\mathrm{d}t} - L_q \Omega_e i_q + R i_d \\ v_q = L_q \frac{\mathrm{d}i_q}{\mathrm{d}t} + L_d \Omega_e i_d + \lambda_p \Omega_e + R i_q \end{cases} \tag{5.18}$$

So far, the analysis is made for a single pole machine model, for a p pole pairs machine, the equation can be rewritten by just substituting θ_e with $p\Omega$:

$$\begin{cases} v_d = L_d \frac{\mathrm{d}i_d}{\mathrm{d}t} - p L_q \Omega i_q + R i_d \\ v_q = L_q \frac{\mathrm{d}i_q}{\mathrm{d}t} + p L_d \Omega i_d + p \lambda_p \Omega + R i_q \end{cases} \tag{5.19}$$

Remember that for SPM motors, the sinusoidal term L_2 vanishes due to the isotropic property of the rotor and thus, the inductance L_d and L_q are equal.

Power balance analysis

Next step is to make the power balance of the machine by performing the sum of products of the voltages and currents in both d and q axes with the introduced matching factor 3/2, and yield the result:

$$P = \frac{3}{2}(v_d i_d + v_q i_q) = \frac{3}{2}\left[L_d i_d \frac{\mathrm{d}i_d}{\mathrm{d}t} + L_q i_q \frac{\mathrm{d}i_q}{\mathrm{d}t} + p(L_d - L_q)\Omega i_d i_q + p\lambda_p \Omega i_q + R(i_d^2 + i_q^2) \right] \tag{5.20}$$

It is worth to note that the first part of the equation ($[L_d i_d \frac{\mathrm{d}i_d}{\mathrm{d}t} + L_q i_q \frac{\mathrm{d}i_q}{\mathrm{d}t}]$) is related to the variation of the magnetic energy, then there is the term ($[R(i_d^2 + i_q^2)]$) related to the Joule losses and finally, the remaining part which is proportional to the speed is related to the mechanical power P_m (or the air gap power). The torque therefore can be obtained by diving this mechanical power by the speed.

$$T = \frac{P_\mathrm{m}}{\Omega} = \frac{3}{2} p \lambda_p i_q + \frac{3}{2} p (L_d - L_q) i_d i_q \tag{5.21}$$

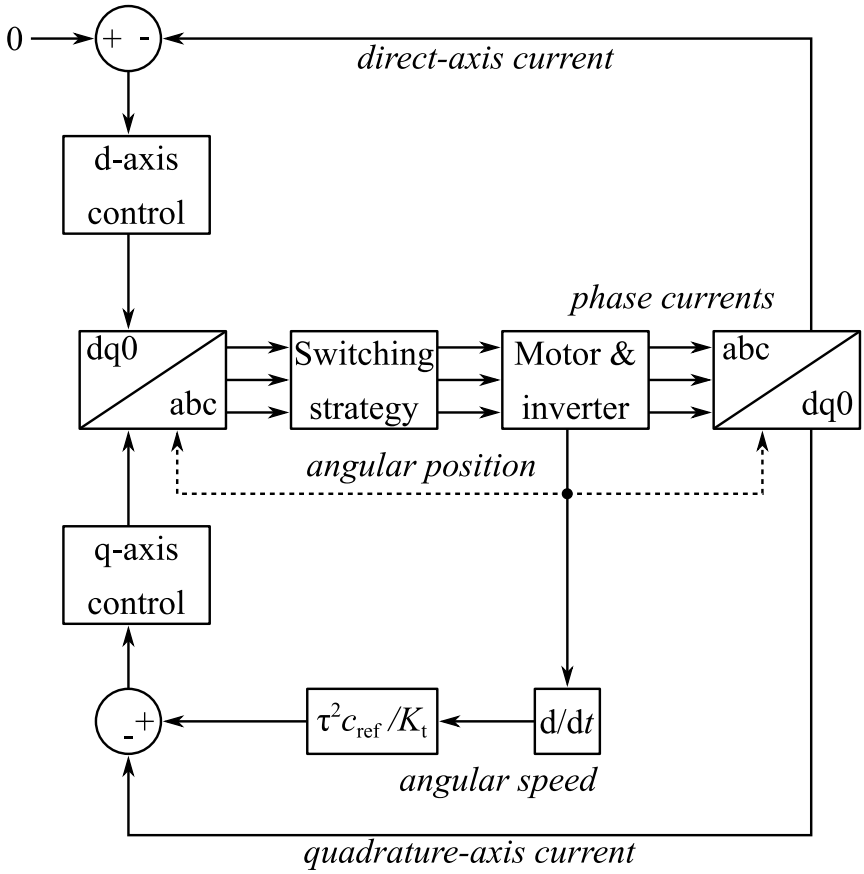

Fig. 5.7 Block diagram of the control strategy for the motor-pump unit.

It is observed that the first term ($\frac{3}{2}p\lambda_p i_q$) which is exclusively dependent on i_q and it is defined as the PM alignment torque, while the other term which depends on both currents and the inductance is called the reluctance torque. When a machine is generating torque, these two terms interact with each other and in particular, for SPM motors, since L_d and L_q have the same value, the reluctance torque will be zero and only the PM alignment torque remains.

5.2 Control strategy implementation

5.2.1 Control algorithm

Fig.5.7 shows the block diagram of the control strategy for the designed motor-pump prototype, basically, there are two tasks, an internal loop task (also known as the

current loop) and an external loop task to give the current references I_{d} and I_{q}. Furthermore, the corresponding algorithm related to the internal and external loop task are given below:

Algorithm 1 Internal Loop Task

Input: Measured current on phase a, I_{a}; Measured current on phase b, I_{b};
Output: Switching pattern to the inverter;
1: Filter the signals I_{a} and I_{b};
2: Execute task to obtain rotor speed Ω and position θ;
3: Filter the signals Ω and θ;
4: Apply Clarke transformation $\mathbf{T}_c$;
5: Apply Park transformation $\mathbf{T}_p$;
6: Compare with reference signals in PI and obtain signal error;
7: Compute PI output (voltage command);
8: Apply inverse Park transformation $\mathbf{T}_p^{-1}$;
9: Apply inverse Clarke transformation $\mathbf{T}_c^{-1}$;
10: Obtain switching pattern from three-phase voltage command through Space Vector Modulation (SVM);
11: **return**

Algorithm 2 External Loop Task

Input: Rotor speed, Ω; Damping coefficient gain (in [mA/rpm]), c_{eq};
Output: Reference current on d-axis, $I_{\mathrm{d,ref}}$; Reference current on q-axis, $I_{\mathrm{q,ref}}$;
1: Set $I_{\mathrm{d,ref}} = 0$;
2: Multiply the filtered signal Ω by c_{eq} to obtain $I_{\mathrm{q,ref}}$;
3: Saturate the obtained signal $I_{\mathrm{q,ref}}$ at 40A;
4: **return**

Since the rotor flux position is the core of FOC (noticed that both Park and inverse Park transformations need this information). In synchronous machines, the rotor speed is equal to the rotor flux speed. Then the rotor flux position can be directly measured by position sensors or by integration of rotor speed.

To compute the rotor speed, the angle sensors were placed to yield an electrical angle accuracy of $2\pi/6$, which means a 60-degree resolution in the electrical frame (electrical angles are needed for the commutation). To achieve a larger resolution, the angles were interpolated based on the previous measurements. In particular, the approach is to adapt the slope of these angles according to the previous measurements, and the mistake (if any) will be corrected right away at each Hall sensor edge. Finally, the speed can be estimated as the slope of the interpolation while the angle or position

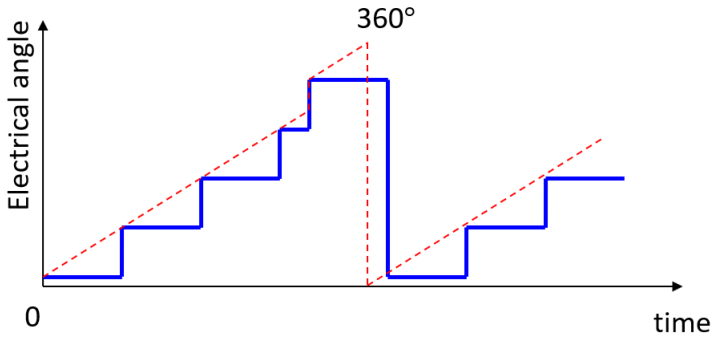

Fig. 5.8 Angle estimation plot from hall sensor

is just the integration of the speed as shown in Fig.5.8. Noticed that a noisy speed estimation may lead to a poor angle feedback for FOC (Park transformations) and a poor current reference, therefore, a 50 Hz low pass filter (LPF) has been also implemented to obtain a cleaner signal.

The Hall sensors are sampled at the switching frequency f_{sw} (40 kHz), and the speed is calculated with a 'capture' approach, as:

$$\Omega = \frac{\theta}{\Delta T} = \frac{\theta f_{sw}}{\text{count}} \tag{5.22}$$

where θ is a fixed angular displacement, while ΔT is the time that takes to move such a displacement. At first, the rising edge of one Hall sensor(i.e.H1) was taken as a reference with a $\theta = 360°/5 = 72°$.

Noticed that the minimum value of ΔT will be $25\mu s$ $(1 \cdot f_{sw}^{-1})$, which will yield a maximum measurable speed of 480 krpm. Whereas, the maximum ΔT is limited to 200 ms and leads to a minimum speed of 60 rpm.

It is worth to note that, for a time-varying speed signal, the speed measurement within an arc of $\theta = 360°/5$ might not be enough and thus, may lead to some wrong estimations. To solve this issue, it is possible to use all the Hall sensors to enhance the algorithm and reduce θ to a value of $60°/5$. In this case, the maximum measurable speed is limited to a more reasonable value (compared with 480 krpm):

$$\Omega_{\text{max}} = \frac{60°}{5} \cdot \frac{60\text{rpm}}{360°} \cdot \frac{1}{25\mu\text{s}} = 80\text{krpm} \tag{5.23}$$

5.2.2 Control unit management

Regarding the control unit management, since during the control process, there will be several system exceptions and errors that need to be handled, a discrete state machine is implemented here to describe this process. As shown below, basically, the state machine used in the control consists of three system states (i.e.S1, S2, and S3), for each state, if a specific transient condition (i.e.a,b,c,d) is achieved, the system will pass from current state to another (i.e.transients are indicated by arrowhead lines or curves). All the related parameters are described in Tab.5.1.

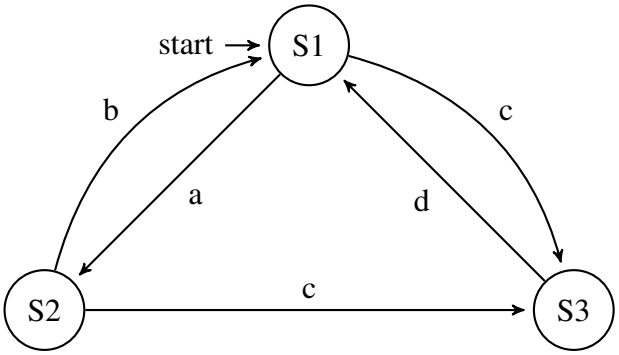

	Symbol	Description
State	**S1**	CONTROL READY
	S2	CONTROL EXECUTING
	S3	FAULT PRESENT
Condition	**a**	`Control_enable=1`
	b	`Force_idle=1`
	c	`Overcurrent=1` OR `Overtemperature=1`
	d	`Fault_reset=1` AND `Overcurrent=0` AND `Overtemperature=0`

Table 5.1 Legend table of system states and transient conditions for the state machine

At the beginning, the system is in 'CONTROL READY' state, to start, the user just need to give one command (i.e.insert 1 in 'FR.ON' cell), then the control will be enabled, and system will enter to 'CONTROL EXECUTING' state, if the user wants to go back to the initial state ('CONTROL READY'), similarly, another command

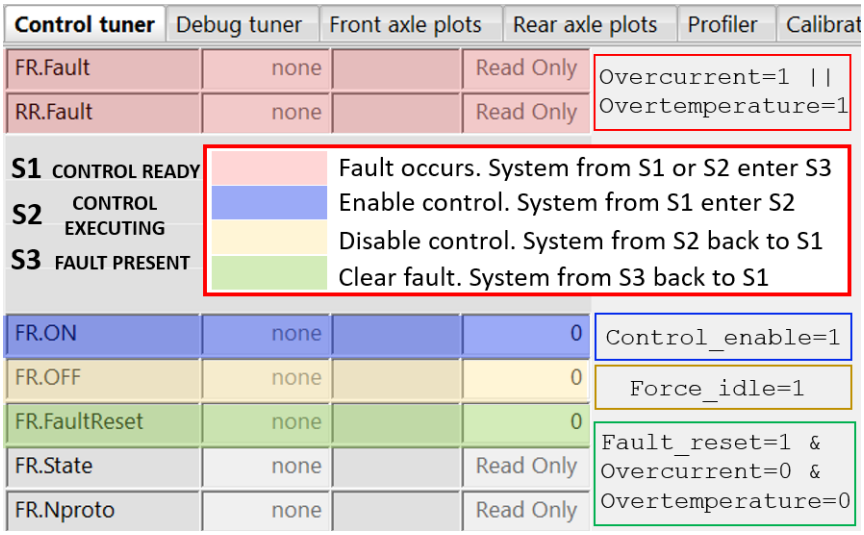

Fig. 5.9 Screen-shot of the User Interface for control unit

should be given (i.e.insert 1 in 'FR.OFF' cell). Noticed that in the control unit, usually there will be a threshold (limit) for the current and temperature considering the safety reasons, whenever an over current OR over temperature event occurs will bring the system to 'FAULT PRESENT' state immediately. However, to recover from the fault state, the user need to give the command to clear the fault (i.e.insert 1 in 'FR.FaultReset' cell) at the same time make sure that there is no critical issues lead to over-current or over temperature failure.

While Fig.5.9 shows the screen-shot from the user interface (UI) for communicating which is connected via CAN by a PCAN-USB adapter. Furthermore, all the above mentioned bidirectional communication variables can be found in such screen-shot.

5.2.3 Power stage hardware

The control strategies were executed by using the multipurpose power module (MPPM) shown in Fig.5.10. The control algorithms were directly implemented in a 32-bit floating-point Digital Signal Processing (DSP) unit (TI TMS320F28335). While the position feedback is obtained with an array of three Hall-effect latches (Allegro A1210) and a PM array fixed to the end of the rotor. The DC bus and phase currents are measured using Hall-effect current probes (AMPLOC AMP25).

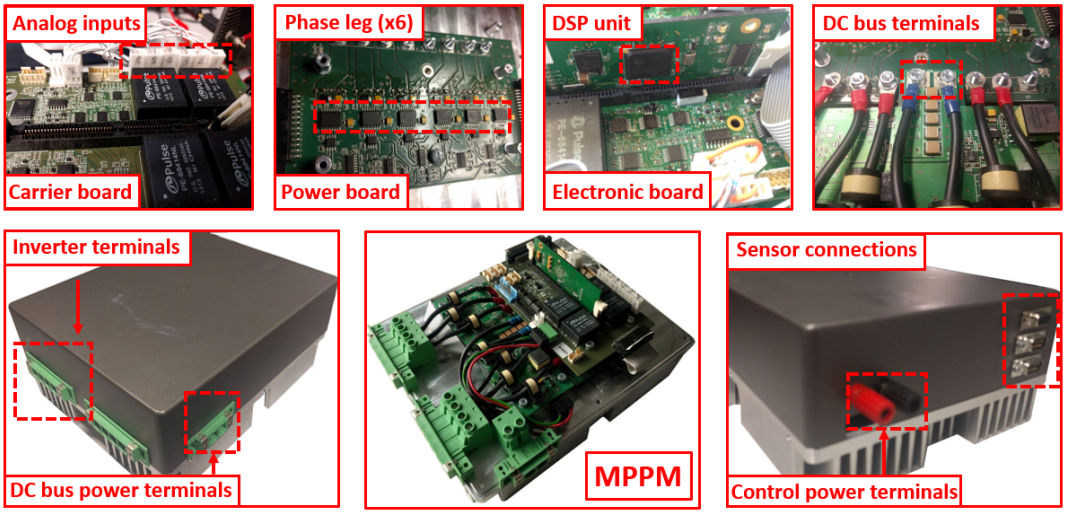

Fig. 5.10 Multipurpose power module (MPPM). Courtesy of Mechatronics Laboratory, Politecnico di Torino.

Furthermore, the internal (current)loop task runs at a frequency of 40 kHz while the external loop task runs at one tenth of the inner one, i.e. 4 kHz.

To provide full-active functionality, a power stage with a three-phase bridge is adopted, the employed power unit presents an inverter constructed by three MOSFET phase legs (IXYS FMM150-0075X2F). These switches were carefully selected to comply with the motor ratings and provide a low conduction resistance.

Chapter 6

Experimental Validation

Several experimental tests are carried out in this chapter. First, a static test bench is used to validate the proposed design and evaluate its performance. Then, the prototype will be mounted on a single vehicle shock absorber and tested on the damper test rig. In the end, all the four prototypes will be installed on a vehicle which is running on the real road and experimental data will be collected directly from the test. The testing process will be discussed and the results will be compared and analyzed.

6.1 Experiments based on static test bench

6.1.1 Test rig Setup and Testing Procedure

The static test should be carried out on the proposed design to replicate its behavior on a real shock absorber. Fig.6.1 shows the conceptual layout of such test rig, in which, on the left side of the layout, a motor-pump unit is used to drive the designed prototype by means of two hydraulic pipelines, a gas-loaded accumulator is also connected to stabilize the low-pressure side and avoid pump cavitation phenomenon. The speed of this driving motor-pump unit can be controlled through a dedicated inverter and the prototype is connected with its own power stage which is fed by a 48V battery array.

During the test, a hydraulic flow rate will be generated by the driving motor-pump unit in the circuit, and through the pipelines, the flow will be transformed as an

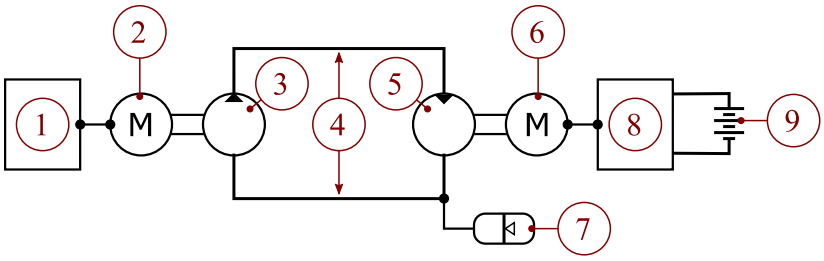

Fig. 6.1 Test rig layout. Inverter (1), driving motor (2), driving pump (3), hydraulic lines (4), prototype pump (5), prototype motor (6), gas-loaded accumulator (7), prototype power stage (8), battery array (9).

angular speed on the rotor of the prototype. If the power stage can simultaneously set constant damping coefficients to the tested electric machine, it is possible to attain different points in the working force-speed plane and thus, to characterize the efficiency.

As shown in Fig.6.2, the complete test rig consists of an inverter-controlled brushless PM motor which is coupled with an external gear pump, the hydrostatic circuit is made of two flexible pipelines together with an accumulator, the length, cross section and profile of the pipelines are chosen specifically in order to minimize the unwanted pressure losses.

A dedicated power stage is used to control the prototype and it is fed by four 12V lead acid batteries in series (48V in total), both the driving unit inverter and the power stage are connected to a PC to monitor and control the testing process by means of RS232 and CAN connection. Different type of sensors are also installed on the test rig to characterize the prototype (i.e. two pressure sensors used to measure the high-pressure and low-pressure sides of the hydraulic circuit, one turbine flow meter used to measure the circuit flow rate). Battery voltage and current can be obtained with dedicated probes. The angular speed of the prototype is monitored from one of the Hall latches with a voltage probe. All these signals are recorded in time using a dedicated data acquisition system. The detailed information of each equipment or device appeared in the test rig are listed in Tab.6.1.

To obtain more reliable and accurate results, during the test, a sequence of steps should be followed strictly as shown below:

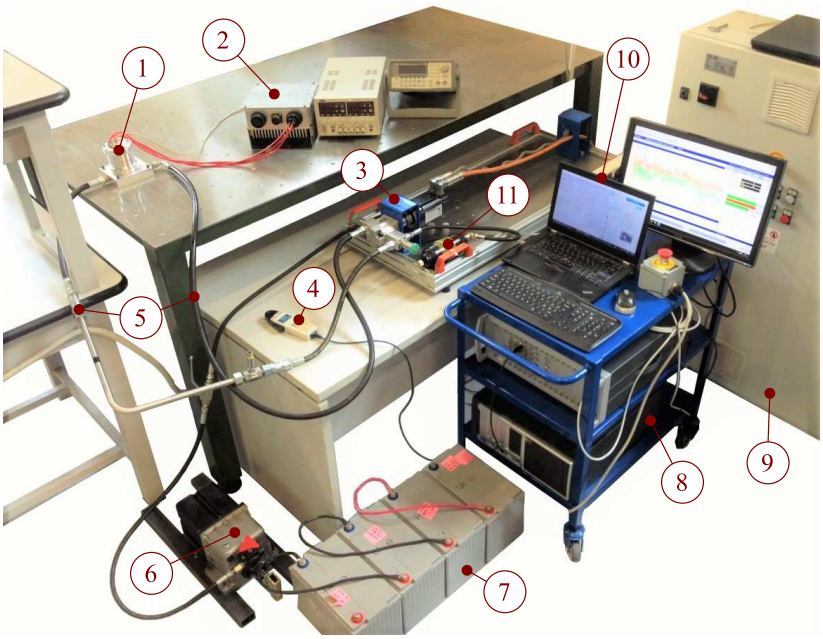

Fig. 6.2 Test rig setup. Motor-pump prototype (1), power stage (2), driving motor-pump unit (3), current probe (4), hydraulic lines (5), hand pump to fill the circuit (6), battery array (7), data logging PC (8), driving motor switchboard (9), control PC (10), gas-loaded accumulator (11).

1. Give a command to the driving motor to rotate with a constant speed, therefore, the external gear pump which is hydraulically connected to the prototype is also driven by a constant speed value.

2. A set of reference damping coefficients starting from zero is imposed from the power stage to the prototype, and these damping values will help to cover different working points on the damper force-speed plane.

3. Under each imposed damping coefficient, a set of measurements from the sensor signals (i.e. the pressure drop, input flow rate, gerotor angular speed, DC bus voltage and current) are acquired by the data acquisition system.

4. After acquiring the desired set of measurements, change the speed of the driving motor to another constant value and the same acquisition procedure from step 1 to 3 is repeated.

Noticed that since there will be four prototypes in total (one for each corner of the vehicle), the same testing procedure and post-processing of the measurement data will be performed for each single prototype.

Table 6.1 Equipments used in the test rig.

Device used in the test rig	Detailed information
Driving motor	Kollmorgen AKM42G
External gear pump	Casappa PLP10
Pipeline connector	G3/8
Accumulator	FOX GR2
Pressure sensor	GEFRAN TK
Flow meter	KEM HM11
Data acquisition hardware	LMS SCADAS

Regarding the data post-processing, different power contributions which will be calculated are summarized below:

- Hydraulic power:

$$P_{\mathrm{h}} = \Delta P Q \tag{6.1}$$

- Mechanical power:

$$P_{\mathrm{m}} = D_{\mathrm{g}} \Delta P \Omega \tag{6.2}$$

- Electromagnetic power:

$$P_{\mathrm{em}} = \frac{3}{2} K_{\mathrm{e}} I_{\mathrm{q,ref}} \Omega \tag{6.3}$$

- Supply power:

$$P_{\mathrm{dc}} = V_{\mathrm{dc}} I_{\mathrm{dc}} \tag{6.4}$$

Furthermore, the pump displacement D_{g} and the electric machine constant K_{e} can be directly extracted from pump and motor design results, in particular, $D_{\mathrm{g}} = 3.6$ cc/rev and $K_{\mathrm{e}} = 21.12$ mVs/rad are taken into account. All these power terms, together with the input flow rate will be interpolated with respect to the pressure drop by using different orders of polynomials.

The obtained polynomials will help to create a map of the different power terms with respect to ΔP and Q. Additional combinations of ΔP and Q can be evaluated through interpolation methods (i.e. *scatteredInterpolant* function in MATLAB).

Once the power functions have been evaluated for a set of ΔP and Q points, the corresponding efficiencies can be calculated as:

- Hydraulic efficiency:

$$\eta_{\mathrm{h}} = \frac{P_{\mathrm{m}}}{P_{\mathrm{h}}} \tag{6.5}$$

- Mechanical efficiency:

$$\eta_{\mathrm{m}} = \frac{P_{\mathrm{em}}}{P_{\mathrm{m}}} \tag{6.6}$$

- Electrical efficiency:

$$\eta_{\mathrm{e}} = \frac{P_{\mathrm{dc}}}{P_{\mathrm{em}}} \tag{6.7}$$

- Total conversion efficiency:

$$\eta_{\mathrm{tot}} = \frac{P_{\mathrm{dc}}}{P_{\mathrm{h}}} = \eta_{\mathrm{h}}\eta_{\mathrm{m}}\eta_{\mathrm{e}} \tag{6.8}$$

To be more realistic, the obtained efficiency map can be expressed in the force-speed plane through the transform in Eq. 3.19, it helps to convert the hydraulic variables into linear mechanical domain when an unitary efficiency of the damper and a cross section area A_{p} are considered.

6.1.2 Static Test Results

Since the proposed design intrinsically yields the same hydraulic behavior in both directions, the characterization result of such device can be represented only in a single quadrant on the force-speed plane.

Fig.6.3 exhibits the experimental results of the prototype which will be installed on the front right corner of the vehicle. Each efficiency contribution (including volumetric, hydro-mechanical and electrical) is plotted separately while the total conversion efficiency is also given as the product of each individual efficiency term.

As shown in the result, the minimum speed of the characterized area starts from about 0.3 m/s which is bounded by the minimum measurable flow rate. By converse, the maximum speed is around 0.8 m/s which is limited by the angular speed of the driving motor-pump unit. The characterized area covers force values between 400 N and 1400 N, which confirms the ability of the proposed design to span different damping characteristics. Furthermore, the maximum force of the prototype is kept below 1500 N to limit the pressure drop and the motor current.

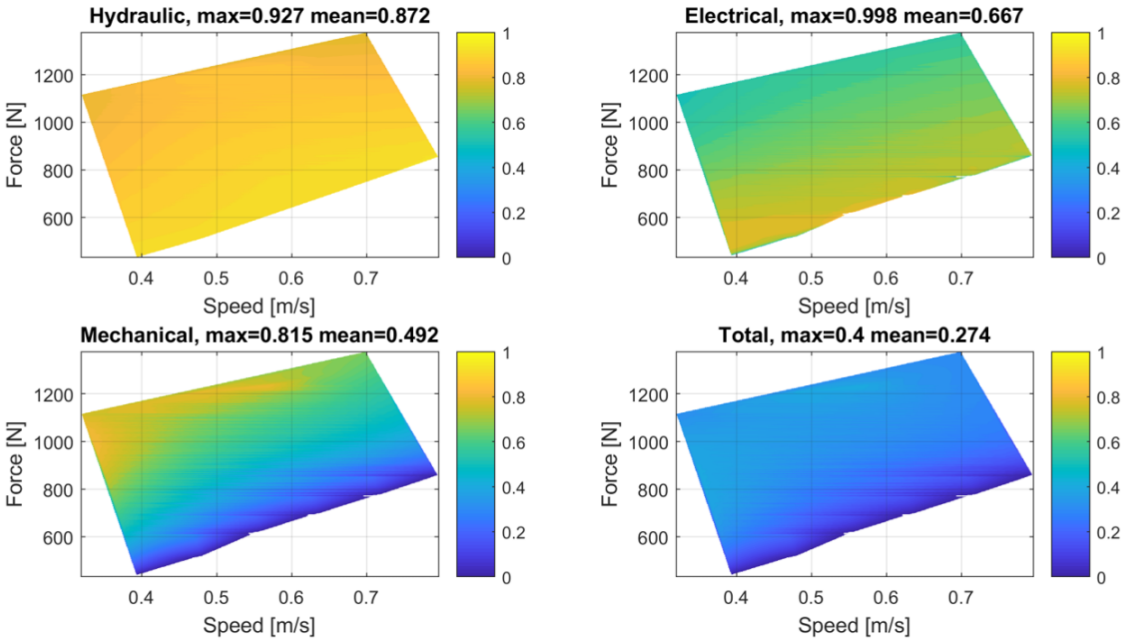

Fig. 6.3 Experimental volumetric, hydro-mechanical, electrical and total conversion efficiency maps obtained from the prototype (front right corner).

The experimental result shows that the hydraulic or volumetric efficiency tends to decrease as the damping value increases, this happens mainly due to the internal leakages inside the pump. While the hydro-mechanical efficiency tends to null in the lower bound of the map, this is because the viscous drag is dominant in the small damping region, as the damping increases, the drag will play a less-substantial role in the total power and change the purely-dissipative behavior. Regarding the electrical efficiency, when the damping increases, the electric machine works close to the short-circuit damping condition and in this case, the Joule loss will increase as well and therefore, lead to a less electrical efficiency value. In contrast, when the reference damping is null, the power stage imposes null current, i.e. infinite impedance, and the electrical efficiency tends to unit.

The total conversion efficiency map can be seen as the superposition of all the contributions. Noticed that at low damping region, the efficiency is lower because in this condition the viscous drag plays an important role and the hydro-mechanical loss is dominant. Then as the damping increases, the total efficiency will increase until reaching its maximum value and then drops again due to the increasing internal leakages and the Joule loss effect.

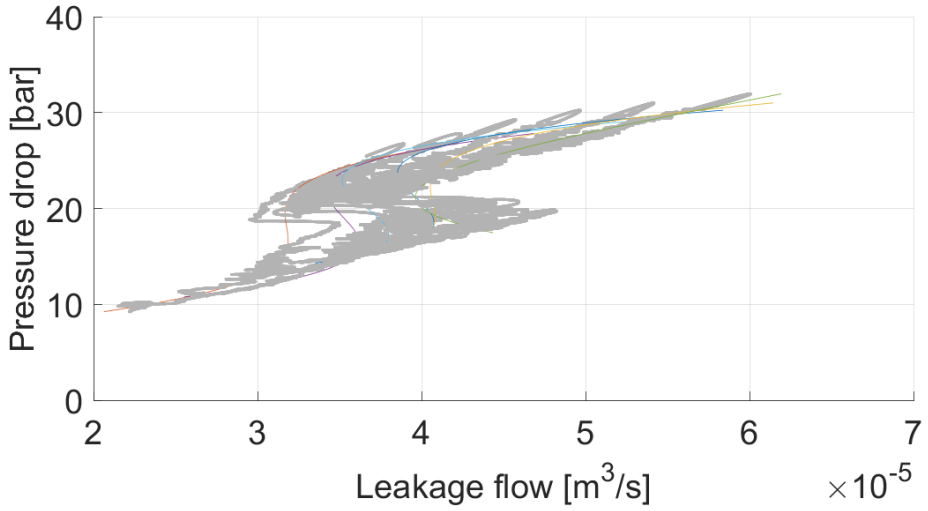

Fig. 6.4 Internal leakage flow characterization.

The results shown in Fig.6.3 can be also used to further characterize the volumetric losses and torque losses.

Eq.2.16 gives the expression of the volumetric efficiency considering the internal leakage phenomenon, therefore, the leakage flow Q_{leak} can be written as the difference between the inlet and outlet flow of the pump:

$$Q_{\text{leak}} = Q_{\text{g}} - V_{\text{g}}\Omega_{\text{g}}, \tag{6.9}$$

Instead of plotting the volumetric efficiency, the leakage flow can be characterized for different pressure drops and flow rates as shown in Fig.6.4 (The result should be in 3D, but since the dependence of leakages on the flow rate is very low, the internal leakage is considered to be depend on the pressure drop only). Suitable polynomials can be found to express this relationship between the leakage and pressure.

Similarly, the hydro-mechanical efficiency map can be used to characterize the torque losses which is mainly caused by hydraulic minor loss and mechanical friction affecting the rotating elements. As shown in Eq.2.17, the hydro-mechanical efficiency can be expressed as the ratio between the electromagnetic torque of the motor and the input torque produced by the rotating pump. Therefore, torque losses T_{loss} can be written as the difference of those two terms:

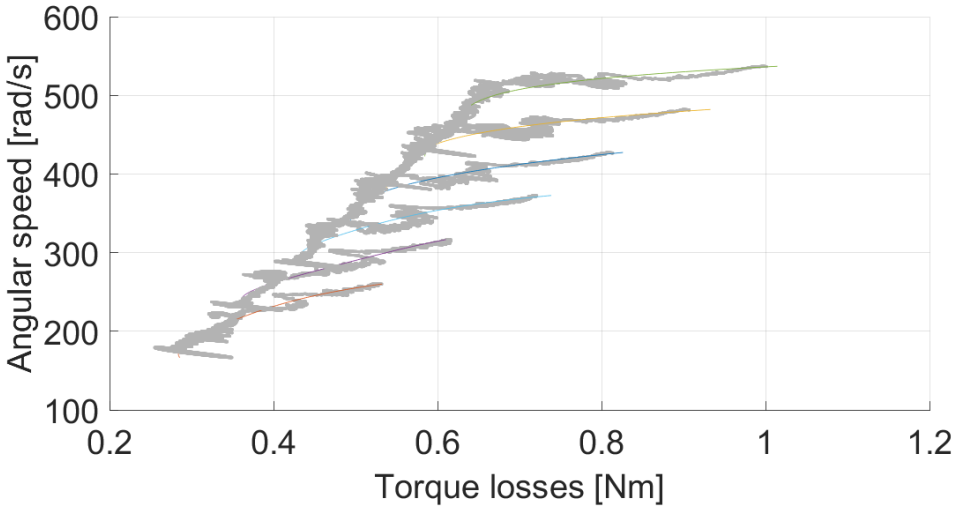

Fig. 6.5 Torque loss characterization.

$$T_{\text{loss}} = V_{\text{g}} \Delta P_{\text{g}} - T_{\text{m}}. \tag{6.10}$$

where T_{m} can be calculated by using Eq.2.4.

Different from the leakage flow, here, the dependence of the torque losses on the pressure drop is very low, instead, it is more related to the speed, as shown is Fig.6.5 (again the result should be in 3D, due to the weak dependence on pressure drop, the torque loss is considered to be depend on the speed only).

It is observed that it seems strange in Fig.6.4, the leakage flow is not continuous but shows a piecewise behavior, to investigate this phenomenon, the leakage and torque losses are compared at the same time as shown in Fig.6.6 where both plots share the same y-axis which indicates the pressure drop. From the plot, it is clear to see that when the pressure drop reaches about 19 bars, there is a jump on the angular speed, and one possible explanation could be that at the beginning, the pump gears are pushed against the casing, as the pressure increases, at a certain moment, pressure balance is achieved and the friction is therefore, reduced evidently and this causes a speedup on the gears and thus, reduces the internal leakage.

From the system modelling point of view, the pump behaves like a non-linear restrictor and the volumetric feature of the pump can be also represented as a non-

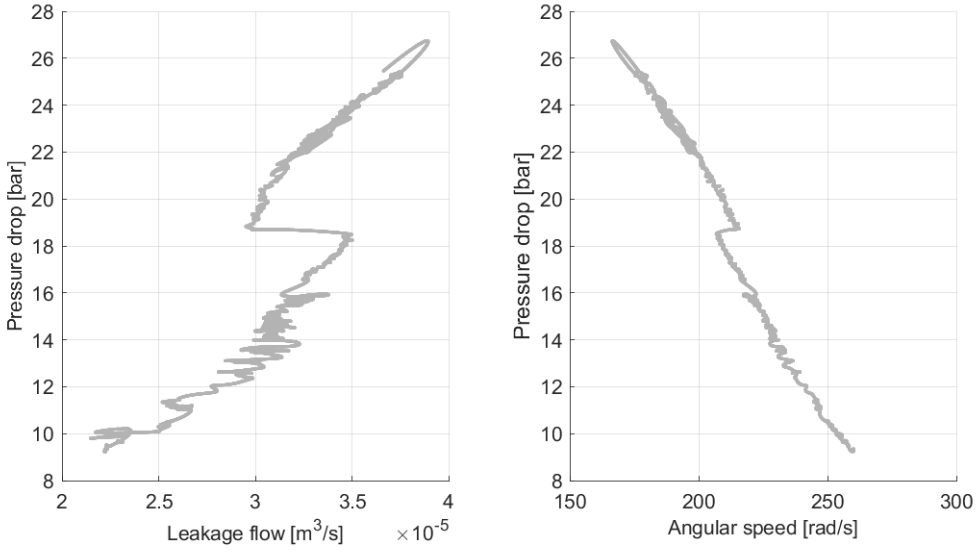

Fig. 6.6 Comparison between leakage and torque losses.

linear restrictor which is in parallel with the pump. While The behavior of the torque loss is more like a damping phenomenon and its damping coefficient can be calculated and this is useful to determine the damping of the moving part of the pump.

Tab.6.2 shows the results from statistical point of view including the average value, standard deviation, minimum, maximum and optimal values of different efficiency contributions and total conversion efficiency. It is observed that the standard deviation of both volumetric and electrical terms are kept below 8% while this value for hydro-mechanical efficiency becomes 17.4%. Considering their range of variety (the difference between maximum and minimum values), similarly the hydro-mechanical term has a larger value than the others. This less-variant behavior for volumetric and electrical terms is somehow expected because the characterized region in the test does not cover very large damping coefficients. As shown in Fig.6.7, the test was carried out in a region with a relative higher piston speed and lower damping force in the force-speed plane. Therefore, larger leakage phenomenon and electrical losses are expected when the damping values continue to increase. However, in the test, a maximum total conversion efficiency of 41.7% is assumed as an optimal value. Therein, the corresponding volumetric efficiency equals to 85%, and a 78% electrical efficiency is obtained. While the larger portion of hydro-

Table 6.2 Statistic features of the experimental efficiency map. The optimal values are obtained in the point where $\eta_t = \max \eta_t$.

Feature	Volumetric	Hydro-mechanical	Electrical	Total
Average value [%]	85.6	44	78.3	28
Standard deviation [%]	6	17.4	7.5	8.4
Minimum value [%]	69.7	0	50.1	0
Maximum value [%]	98.5	80	100	41.7
Optimal value [%]	85.5	62.4	78.2	41.7

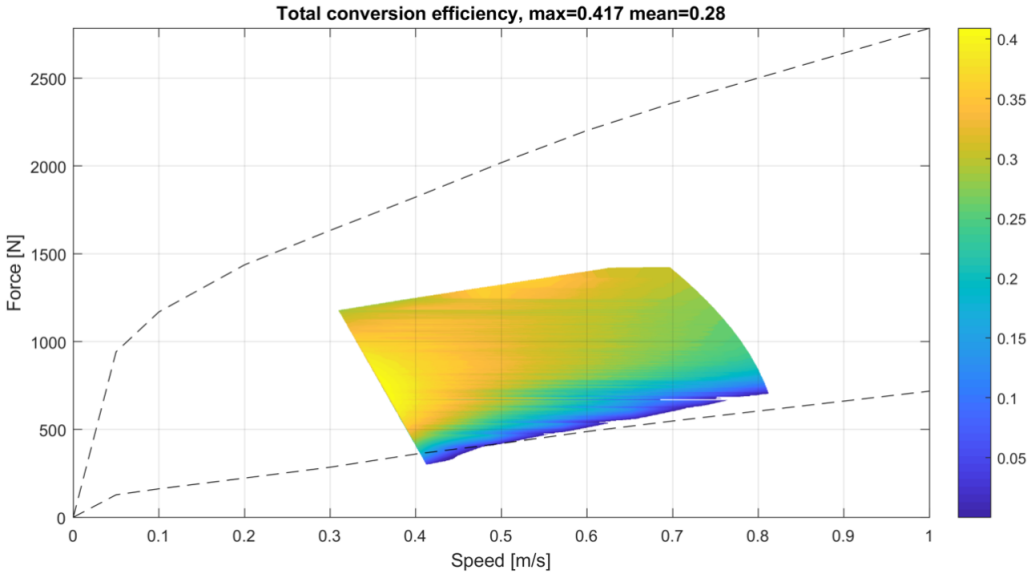

Fig. 6.7 Experimental total conversion efficiency map.

mechanical losses also indicates that the most critical aspect of the design is the hydro-mechanical efficiency.

The experimental results can be compared with the total efficiency map obtained from numerical analysis as shown in Fig. 6.8. The maximum conversion efficiency in this case is 48.7%, against 41.7% obtained in the experiments. The difference can be mainly attributed to larger hydro-mechanical losses. This phenomenon is expected because the pump gears can move axially and radially within the clearance gaps, thus increasing viscous drag, however, these phenomena are not reproduced by the used simulation tools. Furthermore, it is worth to note that when the piston speed is around 0.5 m/s, the minimum force, which is dictated by these losses, reaches about 200 N while in experiments, with the same speed, this force is larger (about

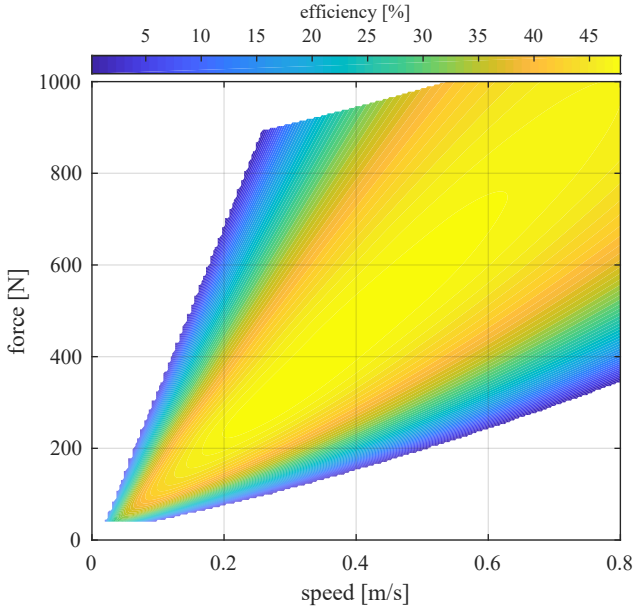

Fig. 6.8 Theoretical total conversion efficiency map of the motor-pump prototype.

500 N). Which means the damping span of the device is shifted to higher force values, as observed in Fig. 6.7, and thus, the total conversion efficiency is penalized.

The obtained results highlight the importance of the experimental characterization of the prototype: hydro-mechanical efficiency is identified as the main responsible of performance reduction. This phenomenon is more evident in the real prototype due to the limitations of the design tools. Hydro-mechanical efficiency can be further enhanced by introducing roller bearing elements on the perimeter of the pump outer gear, reducing the contact surface between the gears and the case and improving radial and axial pressure balance on both pump gears.

6.2 Experiments based on dynamic test bench

Fig.6.9 shows the test bench which is commonly used for characterizing shock absorbers. Before starting the test, the rod of the shock absorber is fixed to the test bench while its body can still move linearly. A certain motion profile can be imposed to the bench according to the need of the user (the most common ones are sinusoidal and triangular movements, sometimes other motion laws are also adopted to replicate

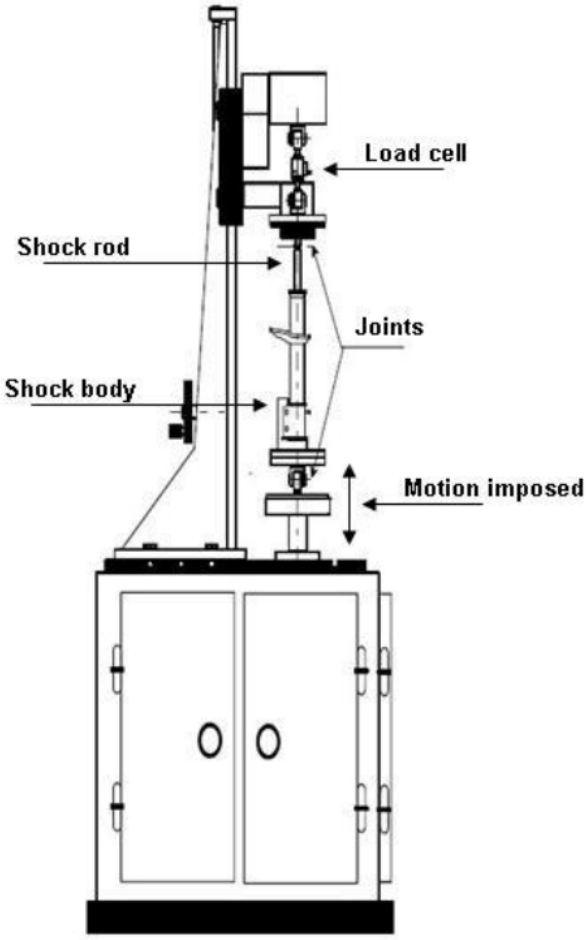

Fig. 6.9 Dynamic test rig for damper characterization used in [23].

specific movement profiles). The reaction force of the shock absorber is measured and acquired through a load cell which is connected with the rod. By convention, the measured forces from the bench are considered positive in extension (rebound) and negative in compression (bump). With this test bench, it is possible to fully characterize the shock absorber by plotting its force-displacement behavior or the force-velocity properties.

To simplify the case, if a sinusoidal movement profile is imposed to the test bench, the displacement d can be expressed by:

$$d = A\sin(2\pi ft) \tag{6.11}$$

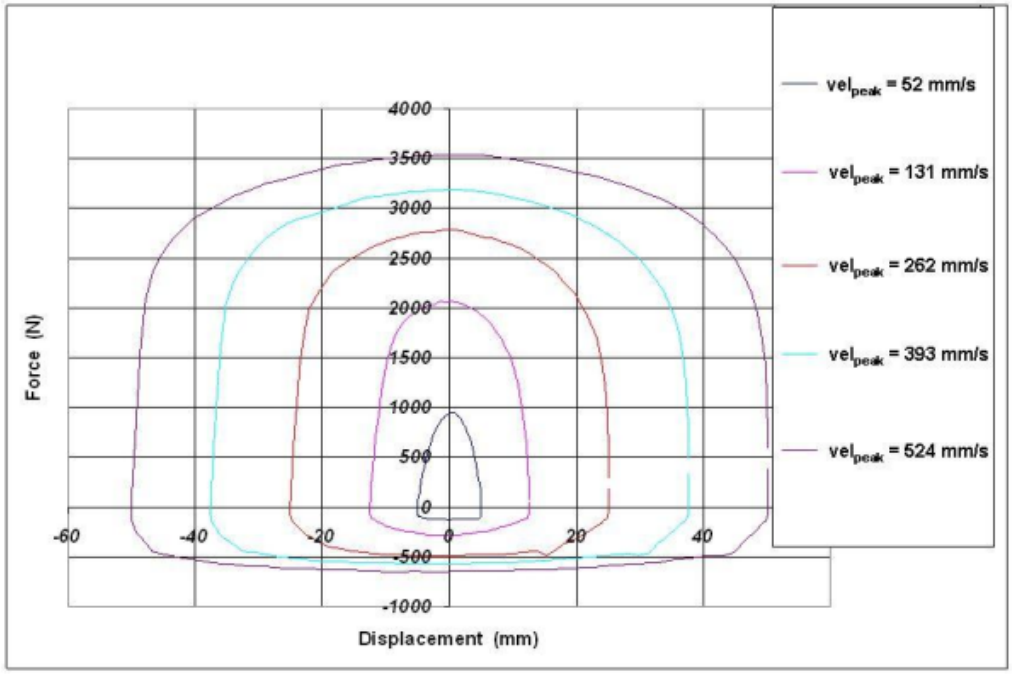

Fig. 6.10 An example of force-displacement graph for shock absorber characterization shown in [23].

where A is the amplitude and f indicates the frequency of the motion.

By definition, the moving velocity v should be the first derivative of the displacement d:

$$v = \dot{d} = 2\pi f A \cos(2\pi f t) \tag{6.12}$$

After assigning different values for the amplitude and frequency, a group of force–displacement curves can be obtained as shown in Fig.6.10. Each curve refers to a peak velocity v_{pk}, which can be defined as:

$$v_{\mathrm{pk}} = 2\pi f A \tag{6.13}$$

From the graph it is observed that for each curve, when the displacement is equal to zero, there will be two points (forces) corresponding to the current peak velocity, one appears during extension (rebound) region and the other one happens in compression (bump) part. Furthermore, the area enclosed within each curve represents the mechanical work that is considered as an input to the shock absorber,

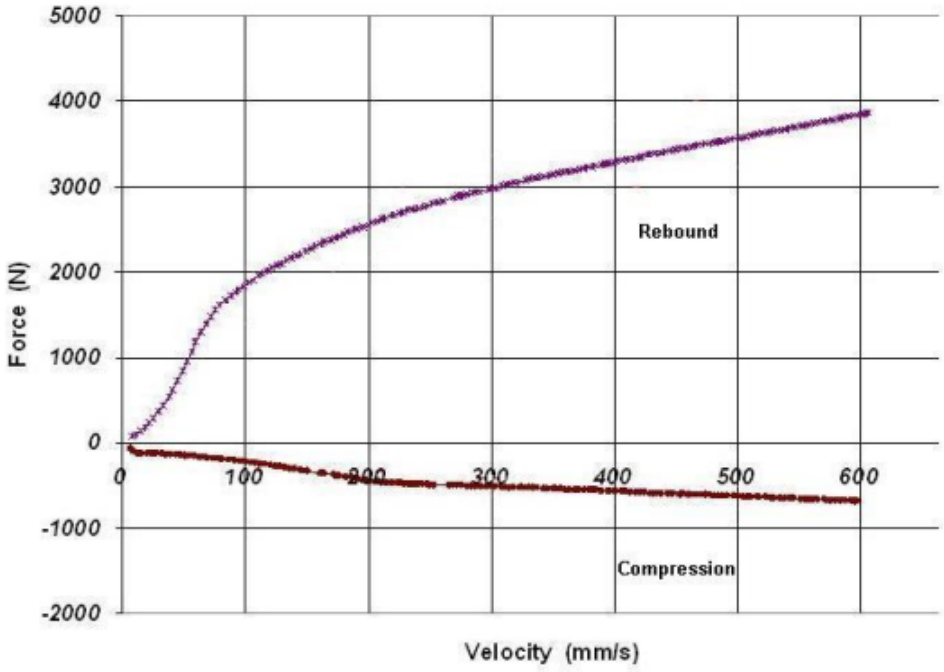

Fig. 6.11 An example of force-velocity graph for shock absorber characterization shown in [23].

which also equals to the energy dissipated during one cycle by the shock absorber under each test.

In some cases, besides using the force-displacement curve, the behavior of shock absorber can be also characterized by the force-velocity graph as shown in Fig.6.11. At each peak velocity, a set of two points (forces) corresponding to zero displacement are reported on the plot, changing force-displacement curves will generate different sets of points and in the end, two curves of forces as a function of the peak velocity is obtained (one for rebound and one for bump).

In the present work, similar dynamic test bench and testing procedures will be adopted for the proposed design. Once the force-displacement (or force-velocity) curve for the regenerative damper is obtained, the overall conversion efficiency can be further characterized accordingly.

In general, the overall conversion efficiency of the regenerative damper depends on its force–velocity characteristics. Furthermore, by definition, the overall conversion efficiency can be defined as the ratio between the electrical work recovered by the shock absorber and the required mechanical work during one cycle of each test.

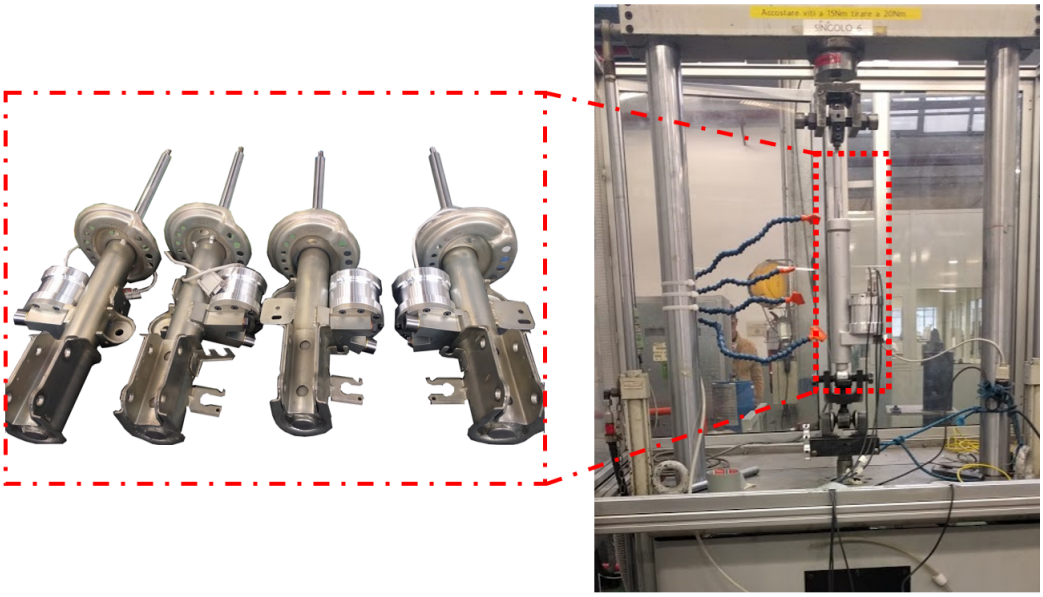

Fig. 6.12 Proposed regenerative damper prototypes and dynamic test bench for characterization.

As mentioned before, the mechanical work can be obtained by calculating the area enclosed within the force–displacement curve. While the recovered electrical work can be computed simply by integrating the output electric power (in this case, the electric power is calculated by the product of directly measured DC-bus voltage and current) delivered during each cycle.

It is worth to note that even for the same shock absorber, with different calibrations, the value of overall conversion efficiency may be changed and therefore, the testing procedure need to be repeated several times and the final overall conversion efficiency will be obtained as the mean value of all the individual efficiency in each single test.

6.2.1 Test rig Setup and testing procedure

Fig.6.12 shows all the four proposed regenerative dampers together with the dynamic test bench which is going to be used for the characterization. Before the test, each damper is filled with 340 cc of a specific suspension oil (with the properties listed in Tab.3.2) as its nominal volume and plus additional 115 cc taking into account the volume of valve and manifold, all the dampers are preloaded to a pressure

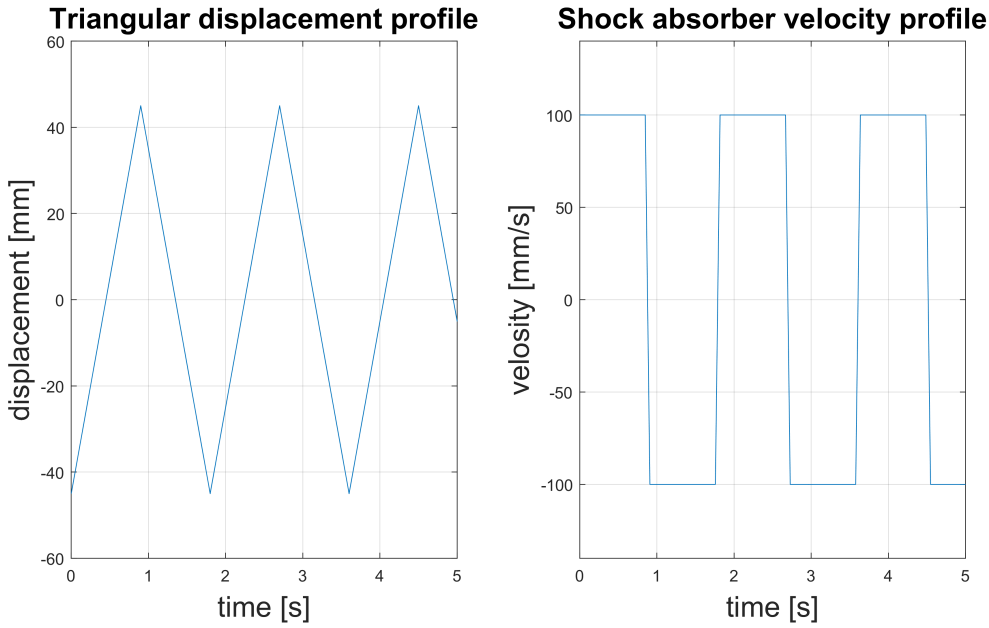

Fig. 6.13 Triangular displacement profile imposed to the test bench.

level between 6 to 8 bars aims to attenuate the cavitation problem during the tests. Furthermore, the regenerative shock absorber is electrically connected with the power stage and supplied by the same 48V battery array from which the DC bus voltage and current can be obtained directly. During the test, a predefined movement profile with triangular waveform is imposed to the bench, experiments are carried out under different frequencies to obtain the force-speed behaviors. At last, the force applied to the damper is measured and subsequently, the total conversion efficiency can be calculated.

6.2.2 Dynamic Test Results

In particular, the triangular waveform imposed to the bench has an amplitude of 45 mm (both for bump and rebound) with a certain frequency, as the velocity is defined by the first derivative of displacement, therefore, such triangular profile is equivalent to a square wave velocity as shown in Fig.6.13. After assigning different frequency values, the damper is able to cover a range of speed (i.e. from 25 mm/s to 1000 mm/s). At the same time, different damping coefficients are imposed to the shock absorber. Fig.6.14 shows the final result including the force-displacement curve and

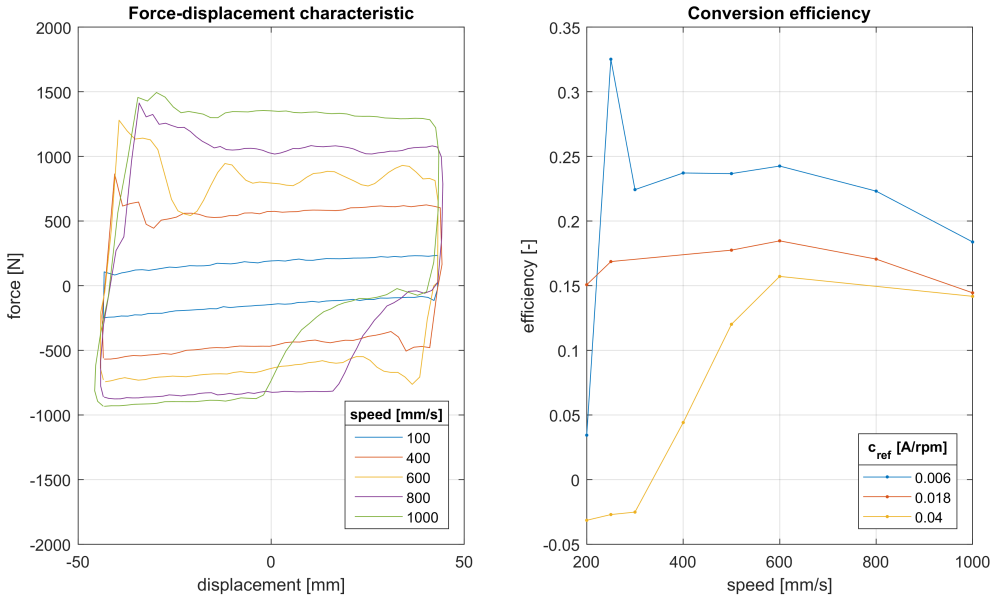

Fig. 6.14 Result of force-displacement curve and total conversion efficiency for the front right corner from dynamic test bench.

the total conversion efficiency (here, only five tests are selected and plotted to have a clear presentation).

It is observed from the result that the total conversion efficiency of the prototype is slightly above 30%. Considering that the measured efficiency in the static test is around 40%, which means the shock absorber itself leads to an efficiency of 75%.

Another observation is that all the prototypes provided a cavitation-free behavior when the input speed is limited to 600 mm/s. While when the speed further increases (i.e. above 800 and 1000 mm/s), the cavitation phenomenon starts to become more evident as shown in the plot (see the lower right corner of the curve). Nevertheless, it is also discovered that this cavitation phenomenon can dramatically reduced with a proper fluid filling condition.

6.3 Experiments based on real road testing

Once the assessments of both static and dynamic tests are done, next challenge will be to mount all the four regenerative dampers on the vehicle and start the real road testing.

During the test, the vehicle is equipped with two electronic control units (ECUs) on board, one is used to control the front axle (front-right and front-left corner) while the other one is in charge of the rear part (rear-right and rear-left corner). Each ECU has two independent output channels corresponding to the two wheels, therefore, it is possible to control the behavior and vary the damping coefficients of the damper separately. Both ECUs are supplied by a 48V battery array from which the DC bus voltage and current will be measured directly to obtain the recovered power. There are several other type of sensors (i.e. the displacement stroke sensor and accelerometers) installed on the vehicle to collect signals for computing the input mechanical power of the suspension. All these measurements are monitored and recorded by a data acquisition system and the final conversion efficiency will be assessed by just making the ratio of the two powers.

Furthermore, a one-degree-of-freedom (1-DOF) model in time domain is used to analyze the obtained signals from the sensors, specifically, this 1-DOF model can be represented as:

$$m_s\ddot{z}_s + k_s(z_s - z_u) + F_d = 0 \tag{6.14}$$

$$F_d = f(\dot{z}_s - \dot{z}_u) \tag{6.15}$$

where the body acceleration $\ddot{z}_s$ and hub acceleration $\ddot{z}_u$ are the measured signals from the sensors during the test.

Fig.6.15 shows the model which is used for simulating the road test, the hub acceleration is used as an input to the model while the body acceleration is extracted as an output. Numeric and measured data for $\ddot{z}_s$ are compared. The damper is represented with its nonlinear model comprising mechanical and volumetric losses. This 1-DOF model presents a single resonance due to the sprung mass at low frequency (close to 1 Hz). Hence, during pre-processing, the acceleration signals were filtered with a 20 Hz low-pass filter. The bias was also removed to avoid signal drift after integration.

During the test, the vehicle is supposed to run straightly along a specific road profile (i.e.ISO-C road) with a constant speed (through the cruise control function of the vehicle). To obtain more reliable and meaningful measurements, it is recom-

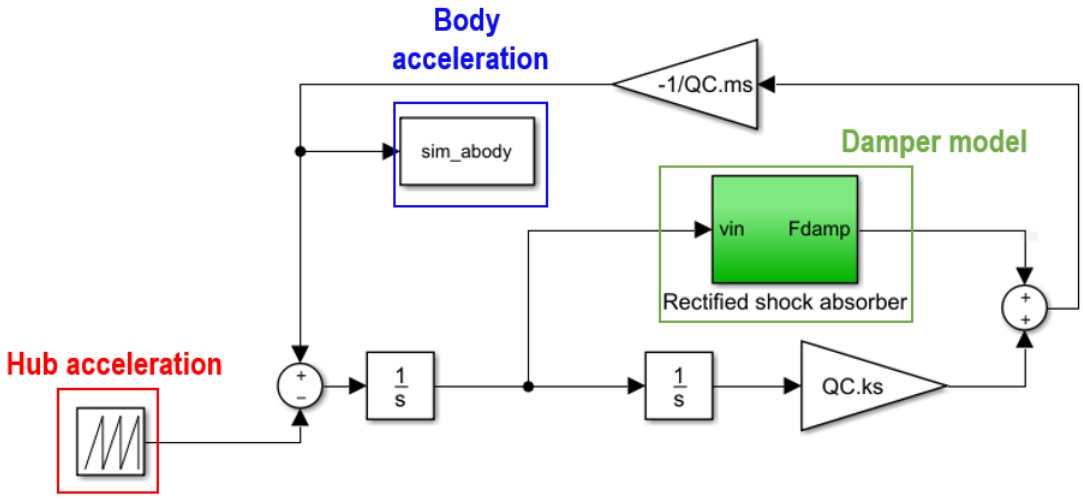

Fig. 6.15 Simulink model for road test.

mended to proceed with the test always on the same road with the same velocity under each damping condition, the duration time of each test can vary from some seconds up to some minutes.

6.3.1 Test rig Setup and Testing Procedure

A FIAT 500X vehicle is chosen to perform the real road testing. Fig.6.16 shows the status of electric wiring on board. Specifically, the front ECU is placed under the glove compartment while the rear ECU together with the 48 V battery array are fixed on the flat surface of a wooden support which is located in the luggage compartment, special protective actions (i.e. by putting some foam to work as a buffer) are made to avoid possible oscillations and therefore, potential damages during the test. To avoid direct connection to the battery, a fused 12 V output is available coming from the car lighter. On one hand, it can be used to connect the control side of the two power modules directly with 12 V and on the other hand, to supply the monitoring sensors (5 V output) through a step-down DC/DC converter. Fig.6.17 shows the real situation of some components on board.

To guarantee a proper work of the prototypes, before the test, the wire resistance of each phase and each corner is measured and the result will be compared with the winding resistance of electric machine. Tab.6.3 shows the average phase resistance

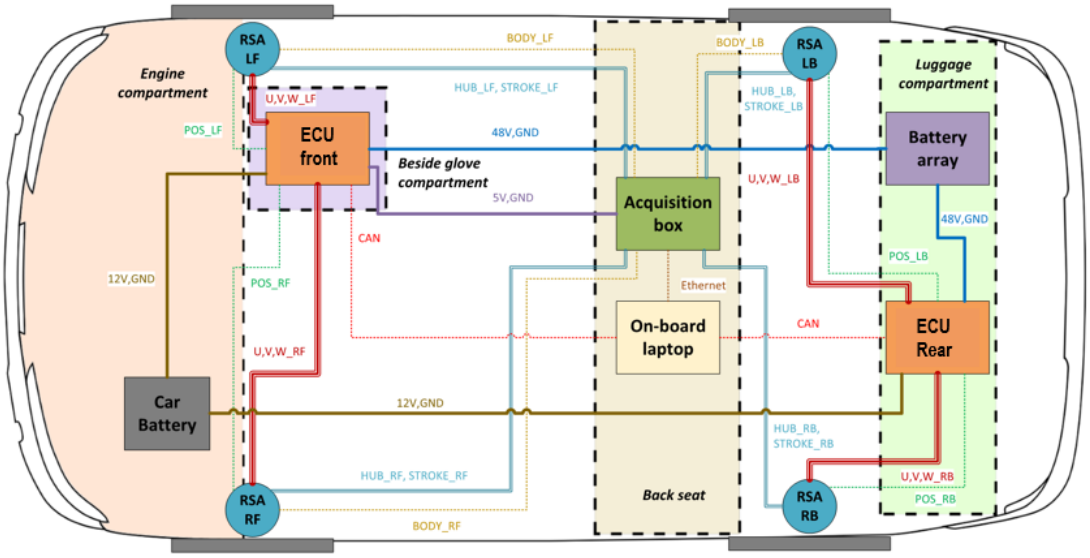

Fig. 6.16 Electric wiring layout for road testing.

of each corner and it turns out that these values are acceptable and the vehicle is ready to perform the following tests.

Fig.6.19 shows the user interface which is used during the test, it is possible to have the monitoring and control of the regenerative dampers at the same time for each corner. By looking at this interface, it can be divided into four different areas corresponding to the four corners of the vehicle. Within each area, the damping coefficient can be changed manually and the control action can be enabled or stopped at any time by the user, other informations for example, the system running status, gerotor rotating speed and reference control current are also indicated for monitoring

Table 6.3 Phase wire resistance assessment

Vehicle corner	**Average phase resistance**	**Relative to motor winding**
Front right	2.3 mΩ	0.12
Front left	3.2 mΩ	0.16
Rear right	2.6 mΩ	0.13
Rear left	2.8 mΩ	0.14

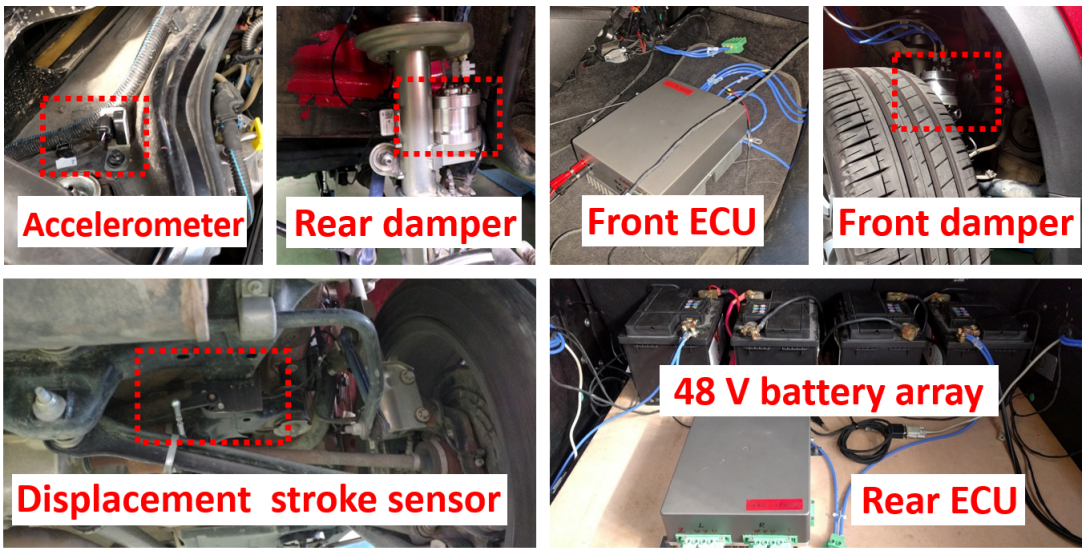

Fig. 6.17 Testing arrangement on the vehicle.

purpose. Furthermore, the regenerated power of front-right and front-left damper are added together as the indicator for front axle, similarly the rear axle regenerated power is also indicated.

6.3.2 Road Test Results

In particular, the road test is carried out focusing on the vehicle's *rear right* corner, besides the regenerative damper, that corner has also equipped with accelerometers for vehicle body and hub, plus a damper stroke sensor. The suspension power can be obtained directly from the sensor signals and independent from the suspension properties (i.e. stiffness or damping characteristics). Since the stiffness ideally yields a zero-mean contribution, the average value of the power can be considered as the dissipation of suspension. This value is also useful to identify the ISO road roughness index with the formula described in Eq.2.42. Furthermore, this dissipated power can be compared with the value calculated in the model to evaluate the damping performance of the suspension.

As shown in Fig.6.18, to complete the experiment, three road profiles with different speeds are tested. Based on the difference of the power stage and load, two testing setups are used for the vehicle rear right corner:

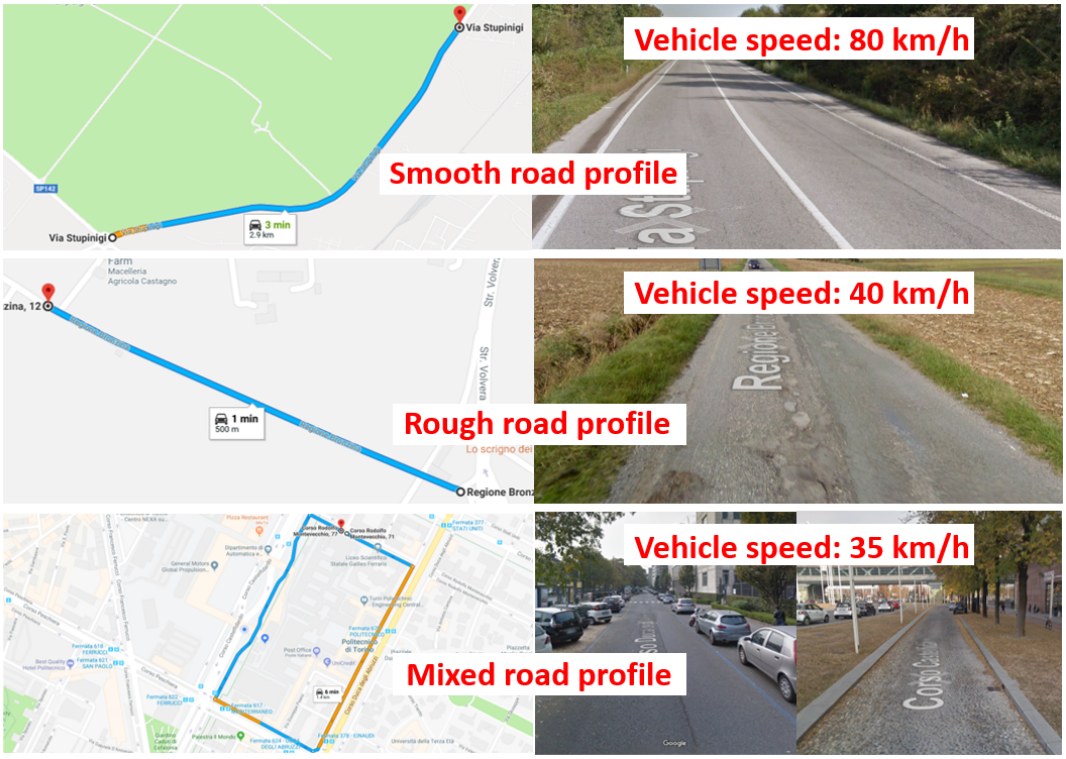

Fig. 6.18 Testing road profiles.

- Use the multi-purpose power module (MPPM) as power stage, and 48V battery array works as load.
- Use the three phase diode rectifier (bridge) as power stage, and different resistor configurations work as load (with external resistance equals to 55mΩ, 135mΩ and 465mΩ).

The test results are shown in Fig.6.20 and Fig.6.21. From the result, it is observed that at low damping region, in the region of maximum recovery, it is seen that the poor power recovery cannot be attributed to the MPPM control strategy. Volumetric and mechanical efficiency components might be lower than expected due to a non-proper fluid filling. While at high damping region, the active control struggles to impose the current because of possible position/speed feedback inaccuracy. The initially estimated speeds are impulsive and thus, the current references are high and produce a large power draw.

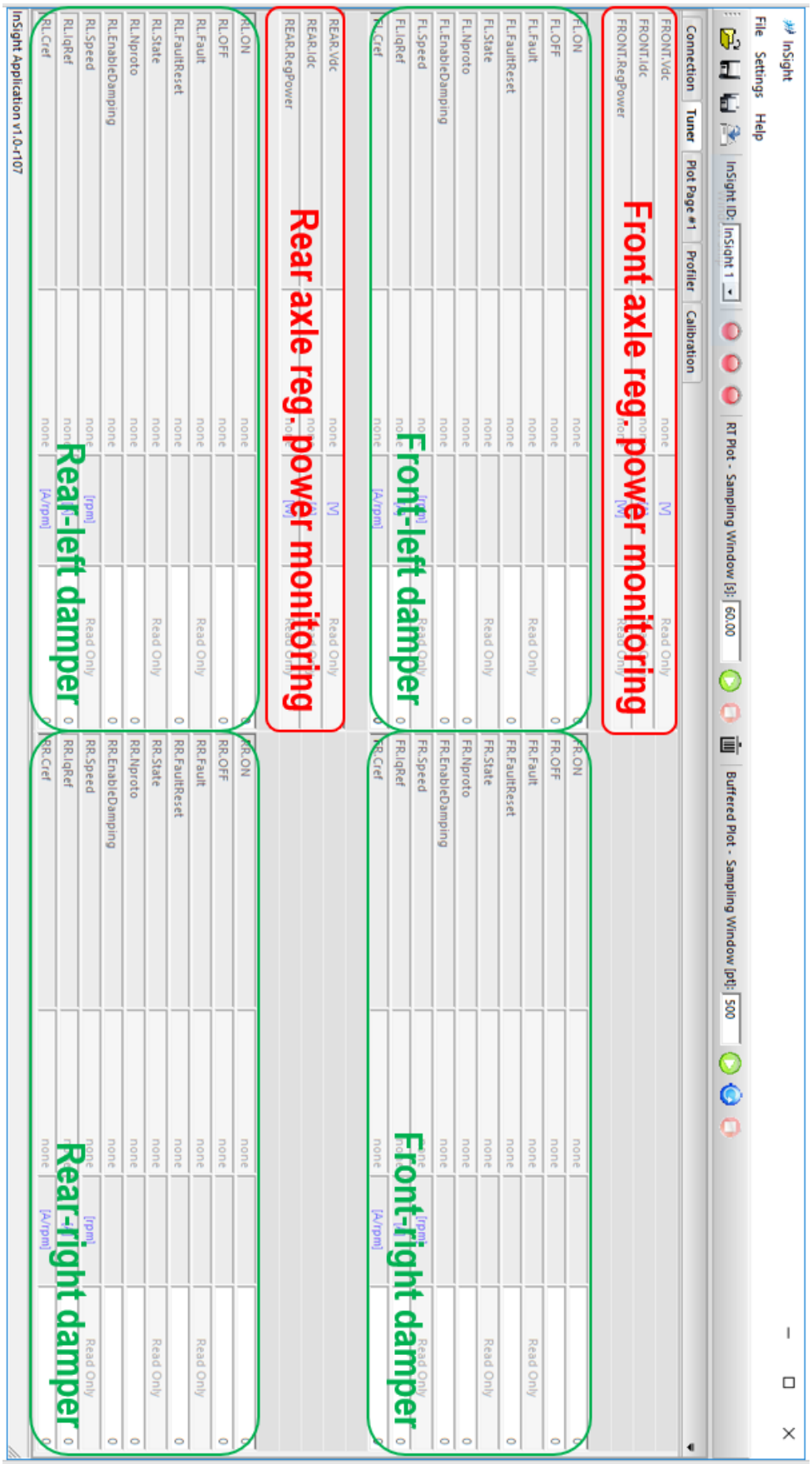

Fig. 6.19 User interface used in the test.

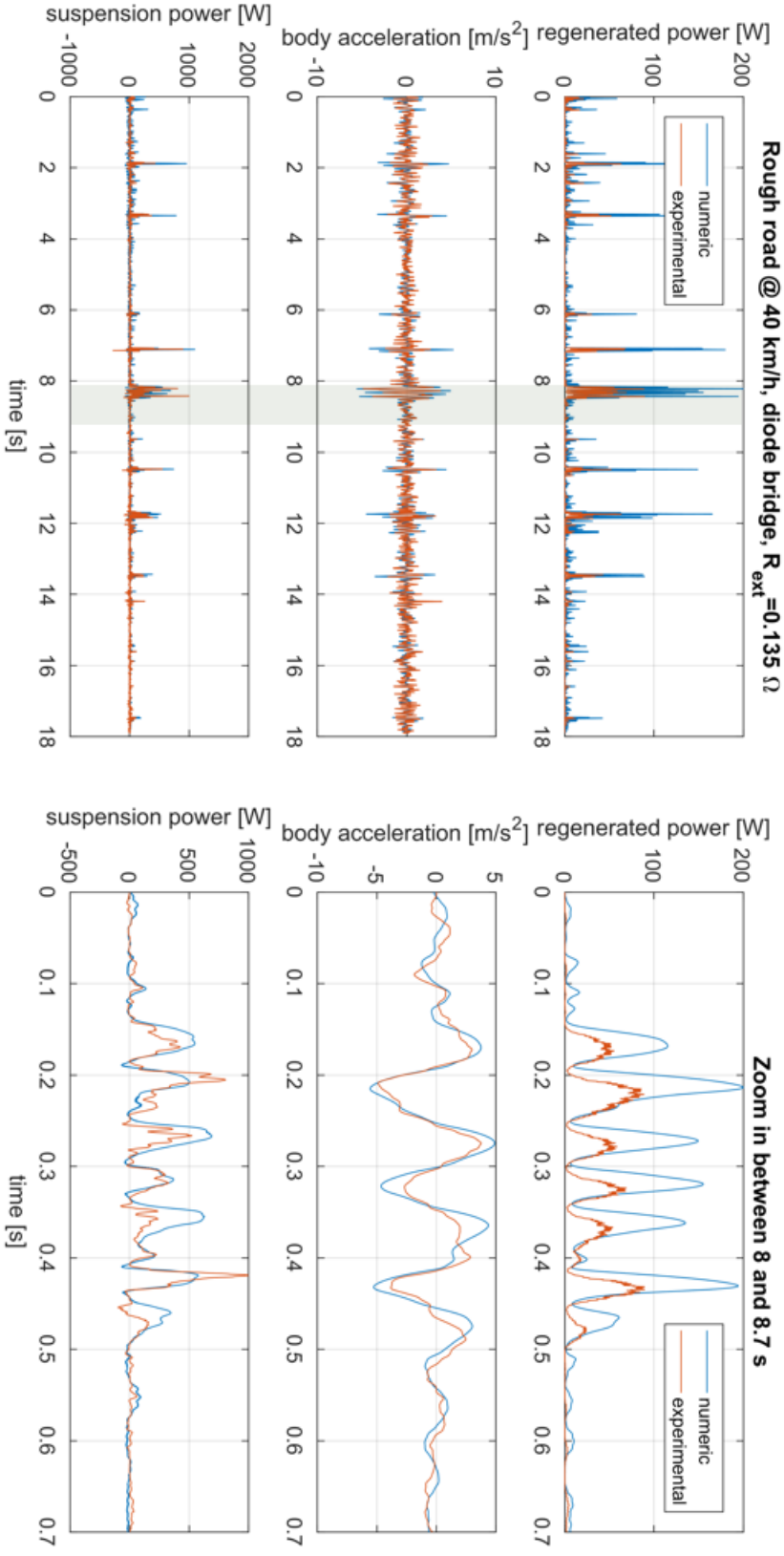

Fig. 6.20 Road testing results.

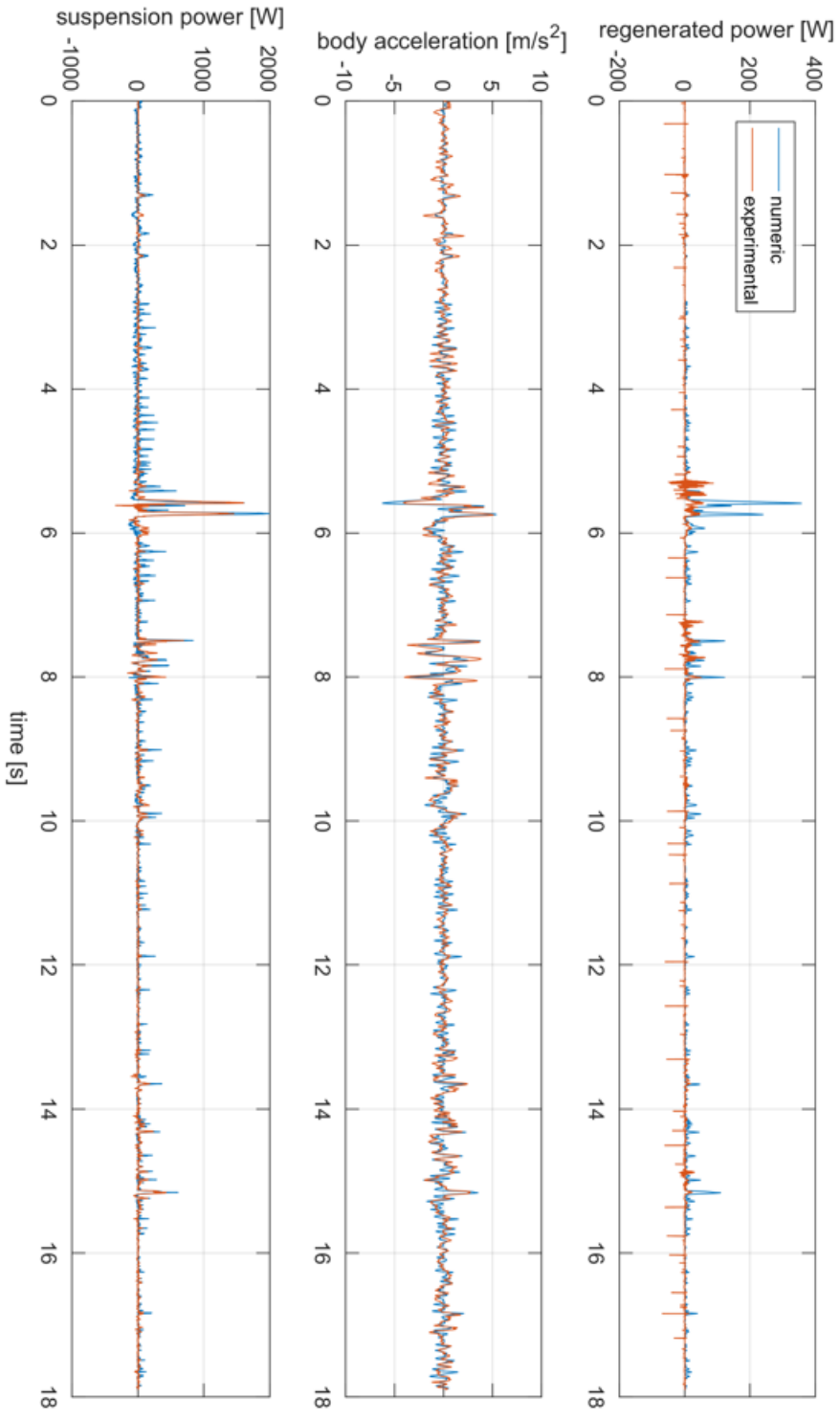

Fig. 6.21 Road testing results.

Chapter 7

Conclusions

The present dissertation discussed the design and implementation of an automotive regenerative shock absorber based on the electro-hydrostatic actuation system. The main contributions of this work consists in:

- Based on the quarter car model, a modified model is established taking into account different road profiles which will give us the indication on the potential regenerative energy.
- A system level approach is followed in the design phase to maximize the overall conversion efficiency.
- The volumetric, hydro-mechanical and electric efficiencies are analyzed individually to understand their influences and contributions.
- The whole system is controlled by a dedicated power stage and connected with load (a 48V battery) instead of using diode bridge rectifier and external resistances.
- A fully characterization of the prototype including static, dynamic and real road tests are carried out to assess the performance of the proposed design.

In the literature review part about the regenerative shock absorbers, it is common to see different works that focused on one or two aspects that influences the conversion efficiency, but very rare to see a fully analysis that covers all the aspects (volumetric, hydro-mechanical and electrical) which is also the novelty of this present work.

From the analysis, it is observed that among different efficiencies that affect the final overall conversion efficiency, the hydro-mechanical part is the most critical one especially at low speed working region. During the experimental test, it shows that sometimes due to the large portion of hydro-mechanical losses, the gerotor will be stuck and cannot rotate normally.

The static experimental results shows a maximum conversion efficiency of 41.7% while this value decreases in the dynamic test (considering the shock absorber efficiency and cavitation phenomenon) and gets further reduced in the real road testing, this is mainly because during the test, the road condition is not strictly the same as ISO standard and the road profile gives a very low excitation on the system and therefore, less energy will be recovered.

References

[1] iea, weo 2010, 450 scenario. http://www.iea.org/.

[2] Energy related nox emissions around the world in 2015. http://www.iea.org/.

[3] CO_2 emissions reducing for passenger vehicles. No.443/2009. Technical report, EU.

[4] Dean Karnopp. Permanent magnet linear motors used as variable mechanical dampers for vehicle suspensions. *Vehicle System Dynamics*, 18(4):187–200, 1989.

[5] Bart LJ Gysen, Tom PJ van der Sande, Johannes JH Paulides, and Elena A Lomonova. Efficiency of a regenerative direct-drive electromagnetic active suspension. *IEEE transactions on vehicular technology*, 60(4):1384–1393, 2011.

[6] Brian Scully, Lei Zuo, Jurgen Shestani, and Yu Zhou. Design and characterization of an electromagnetic energy harvester for vehicle suspensions. In *ASME 2009 International Mechanical Engineering Congress and Exposition*, pages 1007–1016. American Society of Mechanical Engineers, 2009.

[7] Bogdan Sapiński and Stanisław Krupa. Efficiency improvement in a vibration power generator for a linear mr damper: numerical study. *Smart Materials and Structures*, 22(4):045011, 2013.

[8] Zhongjie Li, Lei Zuo, George Luhrs, Liangjun Lin, and Yi-xian Qin. Electromagnetic energy-harvesting shock absorbers: design, modeling, and road tests. *IEEE Transactions on Vehicular Technology*, 62(3):1065–1074, 2013.

[9] Zhongjie Li, Lei Zuo, Jian Kuang, and George Luhrs. Energy-harvesting shock absorber with a mechanical motion rectifier. *Smart Materials and Structures*, 22(2):025008, 2012.

[10] Y Kawamoto, Y Suda, H Inoue, and T Kondo. Electro-mechanical suspension system considering energy consumption and vehicle manoeuvre. *Vehicle System Dynamics*, 46(S1):1053–1063, 2008.

[11] Andrea Tonoli, Nicola Amati, Joaquim Girardello Detoni, Renato Galluzzi, and Enrico Gasparin. Modelling and validation of electromechanical shock absorbers. *Vehicle System Dynamics*, 51(8):1186–1199, 2013.

[12] Xu Wang. *Frequency analysis of vibration energy harvesting systems*. Academic Press, 2016.

[13] Longhan Xie, Jiehong Li, Xiaodong Li, Ledeng Huang, and Siqi Cai. Damping-tunable energy-harvesting vehicle damper with multiple controlled generators: Design, modeling and experiments. *Mechanical Systems and Signal Processing*, 99:859–872, 2018.

[14] Amir Maravandi and Mehrdad Moallem. Regenerative shock absorber using a two-leg motion conversion mechanism. *IEEE/ASME Transactions on Mechatronics*, 20(6):2853–2861, 2015.

[15] Audi's latest chassis suspension system innovation: erot (electromechanical rotary damper). https://www.audi-mediacenter.com/en/press-releases/theinnovative-shock-absorber-system-from-audi-new-technology-saves-fuel-andenhances-comfort-6551.

[16] Zhigang Fang, Xuexun Guo, Lin Xu, and Han Zhang. Experimental study of damping and energy regeneration characteristics of a hydraulic electromagnetic shock absorber. *Advances in Mechanical Engineering*, 5:943528, 2013.

[17] Chuan Li, Rongrong Zhu, Ming Liang, and Shuai Yang. Integration of shock absorption and energy harvesting using a hydraulic rectifier. *Journal of Sound and Vibration*, 333(17):3904–3916, 2014.

[18] Mohamed AA Abdelkareem, Lin Xu, Xuexun Guo, Mohamed Kamal Ahmed Ali, Ahmed Elagouz, Mohamed A Hassan, FA Essa, and Junyi Zou. Energy harvesting sensitivity analysis and assessment of the potential power and full car dynamics for different road modes. *Mechanical Systems and Signal Processing*, 110:307–332, 2018.

[19] International Organization for Standardization. *Mechanical vibration - Road Surfaces Profiles - Reporting of measured data*. The Organization, 1995.

[20] Nichols Portland. Gerotor selection and pump design. Technical report, USA.

[21] Catalog HY09-PGG/MGG/US. Gerotor pump and motor. Technical report, Parker Hannifin Corporation.

[22] M Bhardwaj. Sensored field oriented control of 3-phase permanent magnet synchronous motors. *Texas Instruments, Dallas, TX, USA, Appl. Rep. SPRABQ2*, 2013.

[23] Giordano Greco, Luigi Ippolito, Andrea Nepote, Geert van Grootveld, and Giorgio Martini. Kinetic energy to electric energy conversion using shock absorber. *Material from Magneti Marelli*, pages 1–22, 2013.

[24] Christian Riese, Oliver Stump, and Frank Gauterin. Investigation of the energy recuperation potential of the damper system for a compact class passenger car. *International Journal of Vehicle Design*, 74(4):281, 2017.

[25] Harish Kumar Gangwar, Ankur Sharma, SB Pathak, VIvek Dwivedi, and Amit Nigam. Performance optimization of electronically controlled hydraulic fan drive (hfd) used in commercial application. Technical report, SAE Technical Paper, 2016.

[26] M Montazeri-Gh and O Kavianipour. Investigation of the passive electromagnetic damper. *Acta Mechanica*, 223(12):2633–2646, 2012.

[27] SagivBarDavid and BenZionBobrovsky. Actively controlled vehicle suspension with energy regeneration capabilities. *Vehicle System Dynamics*, 49(6):833–854, 2011.

[28] Zhaoxiang Deng and Fei Lai. Electromagnetic active vehicle suspension system. In *Third International Conference on Measuring Technology and Mechatronics Automation*, pages 15–18, 2011.

[29] BabakEbrahimi, HamidrezaBolandhemmat, MirBehradKhamesee, and FaridGolnaraghi. A hybrid electromagnetic shock absorber for active vehicle suspension systems. *Vehicle System Dynamics*, 49(1-2):311–332, 2011.

[30] Daniel Fischer and Rolf Isermann. Mechatronic semi-active and active vehicle suspensions. *Control Engineering Practice*, 12(11):1353–1367, 2004.

[31] Bart L. J. Gysen, Jeroen L. G. Janssen, Johannes J. H. Paulides, and Elena A. Lomonova. Design aspects of an active electromagnetic suspension system for automotive applications. *IEEE Transactions on Industry Applications*, 45(5):1589–1597, 2008.

[32] Bart L. J. Gysen, Johannes J. H. Paulides, Jeroen L. G. Janssen, and Elena A. Lomonova. Active electromagnetic suspension system for improved vehicle dynamics. *IEEE Transactions on Vehicular Technology*, 59(3):1156–1163, 2010.

[33] Seungho Lee and Won Jong Kim. Active suspension control with direct-drive tubular linear brushless permanent-magnet motor. *IEEE Transactions on Control Systems Technology*, 18(4):859–870, 2010.

[34] Xu Lin, Yang Bo, Xuexun Guo, and Jun Yan. Simulation and performance evaluation of hydraulic transmission electromagnetic energy-regenerative active suspension. In *Second Wri Global Congress on Intelligent Systems*, pages 58–61, 2010.

[35] I. Martins, J. Esteves, G. D. Marques, and F. Pina Da Silva. Permanent-magnets linear actuators applicability in automobile active suspensions. *IEEE Transactions on Vehicular Technology*, 55(1):86–94, 2006.

[36] M. Montazeri-Gh and O. Kavianipour. Investigation of the active electromagnetic suspension system considering hybrid control strategy. *ARCHIVE Proceedings of the Institution of Mechanical Engineers Part C Journal of Mechanical Engineering Science 1989-1996 (vols 203-210)*, 228(10):1658–1669, 2014.

[37] Hideyuki Harada, Yohji Okada, and Kohei Suzuki. Active and regenerative control of an electrodynamic-type suspension. *Transactions of the Japan Society of Mechanical Engineers*, 62(2):272–278, 2008.

[38] J Paulides, E Lomonova, and A Vandenput. Design considerations for an active electro-magnetic suspension system. In *Magnetics Conference, 2006. INTERMAG 2006. IEEE International*, pages 774–774, 2006.

[39] J. Wang, W. Wang, K. Atallah, and D. Howe. Comparative studies of linear permanent magnet motor topologies for active vehicle suspension. In *Vehicle Power and Propulsion Conference, 2008. VPPC '08. IEEE*, pages 1–6, 2008.

[40] Jiabin Wang, Weiya Wang, and Kais Atallah. A linear permanent-magnet motor for active vehicle suspension. *IEEE Transactions on Vehicular Technology*, 60(1):55–63, 2011.

[41] Jiabin Wang, Weiya Wang, Simon Tuplin, and Matthew Best. Design and control of a linear electromagnetic actuator for active vehicle suspension. pages 311–323, 2010.

[42] M Canale, M Milanese, C Novara, and Z Ahmad. Semi-active suspension control using "fast" model predictive control. In *American Control Conference, 2005. Proceedings of the*, pages 274–281, 2005.

[43] M. Canale, M. Milanese, and C. Novara. Semi-active suspension control using "fast" model-predictive techniques. *IEEE Transactions on Control Systems Technology*, 14(6):1034–1046, 2006.

[44] N. Docquier, A. Poncelet, M. Delannoy, and P. Fisette. Multiphysics modelling of multibody systems: application to car semi-active suspensions. *Vehicle System Dynamics*, 48(12):1439–1460, 2010.

[45] Renato Galluzzi, Andrea Tonoli, and Nicola Amati. Modeling, control, and validation of electrohydrostatic shock absorbers. *Journal of Vibration & Acoustics*, 137(1), 2015.

[46] N Giorgetti, A Bemporad, H. E Tsengz, and D Hrovat. Hybrid model predictive control application towards optimal semi-active suspension. *International Journal of Control*, 79(5):521–533, 2006.

[47] Guoliang Hu, Qianjie Liu, Ruqi Ding, and Gang Li. Vibration control of semi-active suspension system with magnetorheological damper based on hyperbolic tangent model. *Advances in Mechanical Engineering*, 9(5):168781401769458, 2017.

[48] DEANKARNOPP. Force generation in semi-active suspensions using modulated dissipative elements. *Vehicle System Dynamics*, 16(5-6):333–343, 1987.

[49] Olof Lindgärde. Kalman filtering in semi-active suspension control. *IFAC Proceedings Volumes*, 35(1):439–444, 2002.

[50] J. J. H. Paulides, L. Encica, E. A. Lomonova, and A. J. A. Vandenput. Design considerations for a semi-active electromagnetic suspension system. *IEEE Transactions on Magnetics*, 42(10):3446–3448, 2006.

[51] Sankaranarayanan Velupillai. Vehicle chassis control using adaptive semi-active suspension. *IFAC Proceedings Volumes*, 41(2):4677–4682, 2008.

[52] S. M. Savaresi, E. Silani, S. Bittanti, and N. Porciani. On performance evaluation methods and control strategies for semi-active suspension systems. In *Decision and Control, 2003. Proceedings. IEEE Conference on*, pages 2264–2269 Vol.3, 2003.

[53] Renato Galluzzi, Francesco Fornari, Enrico Gasparin, and Nicola Amati. Design methodology of electro-hydrostatic shock absorbers for automotive suspensions. In *Congresso Dell'associazione Italiana Di Meccanica Teorica E Applicata*, 2013.

[54] B. L. J Gysen. Generalized harmonic modeling technique for 2d electromagnetic problems : applied to the design of a direct-drive active suspension system. *Technische Universiteitndhoven*, 2011.

[55] K. Huang, F. Yu, and Y. Zhang. Active controller design for an electromagnetic energy-regenerative suspension. *International Journal of Automotive Technology*, 12(6):877–885, 2011.

[56] N. Amati, A. Tonoli, A. Canova, F. Cavalli, and M. Padovani. Dynamic behavior of torsional eddy-current dampers: Sensitivity of the design parameters. *IEEE Transactions on Magnetics*, 43(7):3266–3277, 2007.

[57] Renato Galluzzi, Yijun Xu, Nicola Amati, and Andrea Tonoli. Optimized design and characterization of motor-pump unit for energy-regenerative shock absorbers. *Applied Energy*, 210:16–27, 2018.

[58] Mina M. S. Kaldas, Kemal ?al??kan, Roman Henze, and Ferit Kü?ükay. Optimization of damper top mount characteristics to improve vehicle ride comfort and harshness. *Shock and Vibration,2014,(2014-3-13)*, 20(6):179–184, 2014.

[59] R. Sonnenburg. Optimized parameter combinations of hydraulic damper modules. *Journal of Transportation Technologies*, 4(3):277–288, 2014.

[60] Sijing Guo, Lin Xu, Yilun Liu, Xuexun Guo, and Lei Zuo. Modeling and experiments of a hydraulic electromagnetic energy harvesting shock absorber. *IEEE/ASME Transactions on Mechatronics*, PP(99):1–1, 2017.

[61] G. J. Stein, P. Múčka, T. P. Gunston, and S. Badura. Modelling and simulation of locomotive driver's seat vertical suspension vibration isolation system. *International Journal of Industrial Ergonomics*, 38(5–6):384–395, 2008.

[62] Mina M. S. Kaldas, Kemal Çalışkan, Roman Henze, and Ferit Küçükay. The influence of damper top mount characteristics on vehicle ride comfort and harshness: Parametric study. *SAE International Journal of Passenger Cars - Mechanical Systems*, 5(1):01–21, 2012.

[63] Yoshihiro Suda and Taichi Shiiba. A new hybrid suspension system with active control and energy regeneration. *Vehicle System Dynamics*, 25(S1):641–654, 1996.

[64] Nicola Amati, Andrea Festini, and Andrea Tonoli. Design of electromagnetic shock absorbers for automotive suspensions. *Vehicle system dynamics*, 49(12):1913–1928, 2011.

[65] Colin O'Shea, Yanjun Xia, and Sam Lowry. Analysis and optimization of an electrohydraulic power pack for use in a fully-active vehicle suspension through the use of computational fluid dynamics. In *ASME/BATH 2013 Symposium on Fluid Power and Motion Control*, pages V001T01A002–V001T01A002. American Society of Mechanical Engineers, 2013.

[66] Yuxin Zhang, Xinjie Zhang, Min Zhan, Konghui Guo, Fuquan Zhao, and Zongwei Liu. Study on a novel hydraulic pumping regenerative suspension for vehicles. *Journal of the Franklin Institute*, 352(2):485–499, 2015.

[67] Ruichen Wang, Fengshou Gu, Robert Cattley, and Andrew D Ball. Modelling, testing and analysis of a regenerative hydraulic shock absorber system. *Energies*, 9(5):386, 2016.

[68] Peng Li and Lei Zuo. Influences of the electromagnetic regenerative dampers on the vehicle suspension performance. *Proceedings of the Institution of Mechanical Engineers, Part D: Journal of Automobile Engineering*, 231(3):383–394, 2017.

[69] Chongxiao Zhang, Peng Li, Shaoxu Xing, Junyoung Kim, Liangyao Yu, and Lei Zuo. Integration of regenerative shock absorber into vehicle electric system. In *Active and Passive Smart Structures and Integrated Systems 2014*, volume 9057, page 90570V. International Society for Optics and Photonics, 2014.

[70] Zutao Zhang, Xingtian Zhang, Weiwu Chen, Yagubov Rasim, Waleed Salman, Hongye Pan, Yanping Yuan, and Chunbai Wang. A high-efficiency energy regenerative shock absorber using supercapacitors for renewable energy applications in range extended electric vehicle. *Applied Energy*, 178:177–188, 2016.

[71] Damon Andrews Weeks, Joseph H Beno, Andreas M Guenin, and Don A Bresie. Electromechanical active suspension demonstration for off-road vehicles. Technical report, SAE Technical Paper, 2000.

[72] Yasuhiro Kawamoto, Yoshihiro Suda, Hirofumi Inoue, and Takuhiro Kondo. Modeling of electromagnetic damper for automobile suspension. *Journal of System Design and Dynamics*, 1(3):524–535, 2007.

[73] Guoguang Zhang, Jianyong Cao, and Fan Yu. Design of active and energy-regenerative controllers for dc-motor-based suspension. *Mechatronics*, 22(8):1124–1134, 2012.

[74] Changmiao Yu, Subhash Rakheja, Weihua Wang, and Qingnian Wang. Analysis of an 'on–off'regenerative electromechanical damper. *Proceedings of the Institution of Mechanical Engineers, Part D: Journal of Automobile Engineering*, 227(5):704–722, 2013.

[75] Yilun Liu, Lin Xu, and Lei Zuo. Design, modeling, lab and field tests of a mechanical-motion-rectifier-based energy harvester using a ball-screw mechanism. *IEEE/ASME Transactions on Mechatronics*, 2017.

[76] Reza Sabzehgar, Amir Maravandi, and Mehrdad Moallem. Energy regenerative suspension using an algebraic screw linkage mechanism. *IEEE/ASME Transactions on Mechatronics*, 19(4):1251–1259, 2014.

[77] Waleed Salman, Lingfei Qi, Xin Zhu, Hongye Pan, Xingtian Zhang, Shehar Bano, Zutao Zhang, and Yanping Yuan. A high-efficiency energy regenerative shock absorber using helical gears for powering low-wattage electrical device of electric vehicles. *Energy*, 159:361–372, 2018.

[78] L Zuo, X Tang, and P Zhang. Regenerative shock absorbers with high energy density. *US Patent application*, 61(368.846), 2010.

[79] Zhongjie Li, Lei Zuo, George Luhrs, Liangjun Lin, and Yi-Xian Qin. Design, modeling, and road tests of electromagnetic energy-harvesting shock absorbers. In *ASME 2012 5th Annual Dynamic Systems and Control Conference joint with the JSME 2012 11th Motion and Vibration Conference*, pages 675–684. American Society of Mechanical Engineers, 2012.

[80] Xingtian Zhang, Zutao Zhang, Hongye Pan, Waleed Salman, Yanping Yuan, and Yujie Liu. A portable high-efficiency electromagnetic energy harvesting system using supercapacitors for renewable energy applications in railroads. *Energy Conversion and Management*, 118:287–294, 2016.

[81] Longhan Xie, Jiehong Li, Siqi Cai, and Xiaodong Li. Electromagnetic energy-harvesting damper with multiple independently controlled transducers: On-demand damping and optimal energy regeneration. *IEEE/ASME Transactions on Mechatronics*, 22(6):2705–2713, 2017.

[82] Yongchao Zhang, Kun Huang, Fan Yu, Yonghui Gu, and Daofei Li. Experimental verification of energy-regenerative feasibility for an automotive electrical suspension system. In *Vehicular Electronics and Safety, 2007. ICVES. IEEE International Conference on*, pages 1–5. IEEE, 2007.

[83] Xubin Song and Zhesheng Li. Regenerative damping method and apparatus, July 26 2005. US Patent 6,920,951.

[84] Xubin Song, Zhesheng Li, and Jeremy Richard Edmondson. Regenerative passive and semi-active suspension, August 8 2006. US Patent 7,087,342.

[85] Khushal Ahmad and Monis Alam. Design and simulated analysis of regenerative suspension system with hydraulic cylinder, motor and dynamo. Technical report, SAE Technical Paper, 2017.

[86] Mahmoud Omar, MM El-Kassaby, and Walid Abdelghaffar. A universal suspension test rig for electrohydraulic active and passive automotive suspension system. *Alexandria Engineering Journal*, 56(4):359–370, 2017.

[87] Jia Mi, Lin Xu, Sijing Guo, Lingshuai Meng, and Mohamed AA Abdelkareem. Energy harvesting potential comparison study of a novel railway vehicle bogie system with the hydraulic-electromagnetic energy-regenerative shock absorber. In *2017 Joint Rail Conference*, pages V001T07A004–V001T07A004. American Society of Mechanical Engineers, 2017.

[88] Mustafa Demetgul and Ismail Guney. Design of the hybrid regenerative shock absorber and energy harvesting from linear movement. *Journal of Clean Energy Technologies*, 5(1), 2017.

[89] Babak Ebrahimi, Hamidreza Bolandhemmat, Mir Behrad Khamesee, and Farid Golnaraghi. A hybrid electromagnetic shock absorber for active vehicle suspension systems. *Vehicle System Dynamics*, 49(1-2):311–332, 2011.

[90] Han Zhang, Xuexun Guo, Sanbao Hu, Zhigang Fang, Lin Xu, and Jie Zhang. Simulation analysis on hydraulic-electrical energy regenerative semi-active suspension control characteristic and energy recovery validation test. *Transactions of the Chinese Society of Agricultural Engineering*, 33(16):64–71, 2017.

[91] Ruichen Wang, Fengshou Gu, Robert Cattley, and Andrew D Ball. Modelling, testing and analysis of a regenerative hydraulic shock absorber system. *Energies*, 9(5):386, 2016.

[92] Nitin V Satpute, Shankar Singh, and SM Sawant. Energy harvesting shock absorber with electromagnetic and fluid damping. *Advances in Mechanical Engineering (Hindawi Publishing Corporation)*, 2014.

[93] Levant power‘s new activalve integrated valve technology. genshock energy-recovery suspension. https://www.speedgoat.com/user-stories/speedgoat-userstories/clearmotion.

[94] Zackary Martin Anderson, Shakeel Avadhany, Matthew D Cole, Robert Driscoll, John Giarratana, Marco Giovanardi, Vladimir Gorelik, Jonathan R Leehey, William G Near, Patrick W Neil, et al. Active vehicle suspension system, July 11 2017. US Patent 9,702,349.

[95] Marco Giovanardi, Clive Tucker, Ross J Wendell, Zackary Martin Anderson, Colin Patrick O'shea, Vladimir Gorelik, Tyson David Sawyer, Jonathan R Leehey, Johannes Schneider, Robert Driscoll, et al. Active suspension with on-demand energy flow, January 24 2017. US Patent 9,550,404.

[96] G Romeo. *Electro Hydrostatic Actuation: Comparison with Electro Mechanical Power Actuation System*. PhD thesis, Politecnico di Torino, 2011.

[97] C Prister'a. *Electro Hydrostatic Actuation: Industrial Applications*. PhD thesis, Politecnico di Torino, 2011.

[98] Lei Zuo, Brian Scully, Jurgen Shestani, and Yu Zhou. Design and characterization of an electromagnetic energy harvester for vehicle suspensions. *Smart Materials and Structures*, 19(4):045003, 2010.

[99] CLIMATE ACTION. Technical guidelines for the preparation of applications for the approval of innovative technologies pursuant to regulation (ec) no 443/2009 of the european parliament and of the. *February2013*, 2013.

[100] Andrea Tonoli. Dynamic characteristics of eddy current dampers and couplers. *Journal of Sound & Vibration*, 301(3–5):576–591, 2007.

[101] Renato Galluzzi, Andrea Tonoli, Nicola Amati, Gabriele Curcuruto, Piero Conti, Giordano Greco, and Andrea Nepote. Regenerative shock absorbers and the role of the motion rectifier. Technical report, SAE Technical Paper, 2016.

[102] Yuxin Zhang, Hong Chen, Konghui Guo, Xinjie Zhang, and Shengbo Eben Li. Electro-hydraulic damper for energy harvesting suspension: Modeling, prototyping and experimental validation. *Applied Energy*, 199:1–12, 2017.

[103] N Jasar Reza. Vehicle dynamics: theory and applications. *New York, Statele Unite ale Americii, EdituraSpringersScience+ Business Media, LLC*, 2008.

[104] Lei Zuo and Pei-Sheng Zhang. Energy harvesting, ride comfort, and road handling of regenerative vehicle suspensions. *Journal of Vibration and Acoustics*, 135(1):011002, 2013.

[105] International Organization for Standardization. *Mechanical vibration and shock-Evaluation of human exposure to whole-body vibration-Part 1: General requirements*. The Organization, 1997.

[106] Giorgio Altare and Massimo Rundo. Cfd analysis of gerotor lubricating pumps at high speed: Geometric features influencing the filling capability. In *ASME/BATH 2015 Symposium on Fluid Power and Motion Control*, pages V001T01A024–V001T01A024. American Society of Mechanical Engineers, 2015.

[107] Simerics Inc. Predicting pump leakage with computational fluid dynamics. *White paper, USA*, 2014.

[108] Hb Ding, FC Visser, Y Jiang, and M Furmanczyk. Demonstration and validation of a 3d cfd simulation tool predicting pump performance and cavitation for industrial applications. *Journal of fluids engineering*, 133(1):011101, 2011.

[109] Nicola Bianchi, Michele Dai Pre, Luigi Alberti, and Emanuele Fornasiero. Theory and design of fractional-slot pm machines. In *Conf. Rec. IEEE IAS Annu. Meeting*, page 196, 2007.

[110] Duane C Hanselman. *Brushless permanent magnet motor design*. The Writers' Collective, 2003.

[111] Philip A Hargreaves, Barrie C Mecrow, and Ross Hall. Calculation of iron loss in electrical generators using finite-element analysis. *IEEE Transactions on Industry Applications*, 48(5):1460–1466, 2012.

Appendix A

Permanent-Magnet Synchronous Motor Modelling

A.1 Three-phase model

Fig.A.1 shows the single-pole pair Permanent-Magnet Synchronous Motor (PMSM), the stator has three phases a, b, and c with their corresponding voltages v_i and currents i_i. The rotor is constituted by two phases d and q, with a permanent magnet flux linkage vector of amplitude Λ_r which is aligned to the d axis. The stator equations are:

$$\begin{cases} v_a = \lambda_a{}' + R_a i_a \\ v_b = \lambda_b{}' + R_b i_b \\ v_c = \lambda_c{}' + R_c i_c \end{cases} \tag{A.1}$$

where λ_i represents the flux linkage of the ith winding and R is the resistance. Furthermore, the flux linkages for each phase can be defined as:

$$\begin{cases} \lambda_a = L_a i_a + M_{ab} i_b + M_{ac} i_c + \Lambda_r \cos\theta \\ \lambda_b = M_{ba} i_a + L_b i_b + M_{bc} i_c + \Lambda_r \cos(\theta - 2\pi/3) \\ \lambda_c = M_{ca} i_a + M_{cb} i_b + L_c i_c + \Lambda_r \cos(\theta + 2\pi/3) \end{cases} \tag{A.2}$$

Here, L represents the (auto) inductance which is the flux generated by each phase seeing by the coil itself. This inductance will have a waveform with the angle

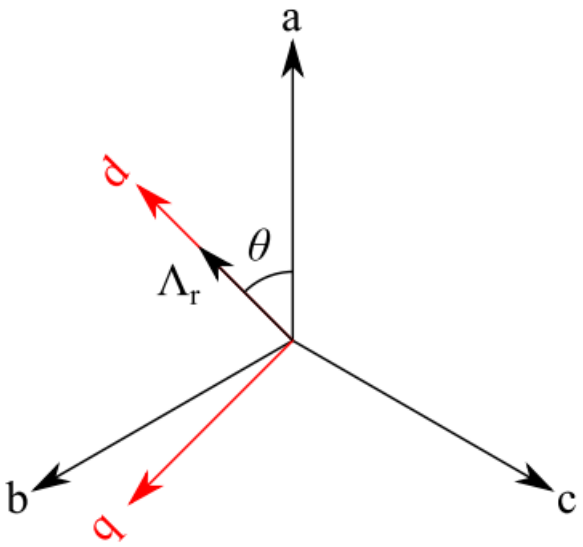

Fig. A.1 Three-phase model for PMSM.

as well. Because the reluctance of the rotor is variable along the circumferential direction in each case and M denotes the mutual inductance between two phases.

Combine Eq.A.1 and A.2 can yield the result in matrix form:

$$\mathbf{v}_{abc} = \mathbf{L}_{abc}\mathbf{i}_{abc}{}' + \mathbf{R}_{abc}\mathbf{i}_{abc} + \mathbf{e} \tag{A.3}$$

$$\begin{Bmatrix} v_a \\ v_b \\ v_c \end{Bmatrix} = \begin{bmatrix} L_a & M_{ab} & M_{ac} \\ M_{ba} & L_b & M_{bc} \\ M_{ca} & M_{cb} & L_c \end{bmatrix} \begin{Bmatrix} i_a \\ i_b \\ i_c \end{Bmatrix}' + \begin{bmatrix} R_a & 0 & 0 \\ 0 & R_b & 0 \\ 0 & 0 & R_c \end{bmatrix} \begin{Bmatrix} i_a \\ i_b \\ i_c \end{Bmatrix} - \Lambda_r \theta' \begin{Bmatrix} \sin\theta \\ \sin(\theta - 2\pi/3) \\ \sin(\theta + 2\pi/3) \end{Bmatrix} \tag{A.4}$$

In particular, the vector **e** represents the back EMF in each phase.

Assuming periodicity and symmetry machine conditions and an isotropic rotor rotating at constant speed Ω, it yields:

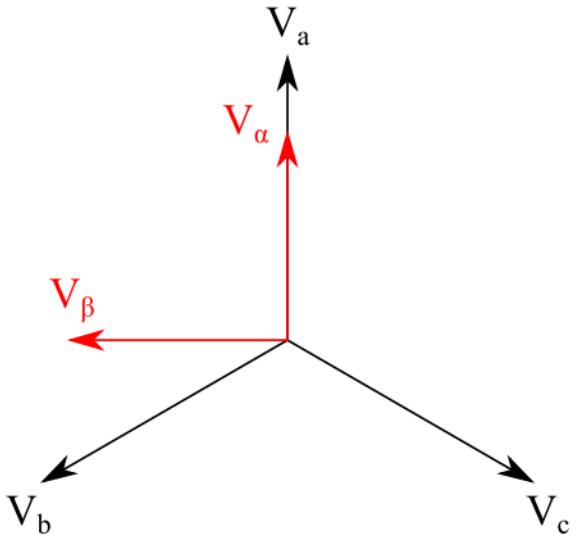

Fig. A.2 Two-phase model for PMSM.

$$\begin{Bmatrix} v_a \\ v_b \\ v_c \end{Bmatrix} = L_s \begin{bmatrix} 1 & -1/2 & -1/2 \\ -1/2 & 1 & -1/2 \\ -1/2 & -1/2 & 1 \end{bmatrix} \begin{Bmatrix} i_a \\ i_b \\ i_c \end{Bmatrix}' + R_s \begin{Bmatrix} i_a \\ i_b \\ i_c \end{Bmatrix} - \Lambda_r \Omega \begin{Bmatrix} \sin(\Omega t) \\ \sin(\Omega t - 2\pi/3) \\ \sin(\Omega t + 2\pi/3) \end{Bmatrix} \tag{A.5}$$

A.2 Two-phase model

Any poly-phase PMSM can be modelled as a two phase motor if an adequate reference frame transformation is applied. For three-to-two phase conversion as shown in Fig.A.2, in this case, the reference frame is fixed to the stator and this is also known as the Clarke transformation, considering:

$$\begin{cases} k_1(v_a + v_b\cos(2\pi/3) + v_c\cos(-2\pi/3)) = v_\alpha \\ k_1(v_b\sin(2\pi/3) + v_c\sin(-2\pi/3)) = v_\beta \\ k_1 k_2(v_a + v_b + v_c) = 0 \end{cases} \tag{A.6}$$

Similarly, it can be written in matrix form:

$$\mathbf{v}_{\alpha\beta 0} = \mathbf{T}_{\alpha\beta 0}\mathbf{v}_{abc} \tag{A.7}$$

$$\begin{Bmatrix} v_\alpha \\ v_\beta \\ 0 \end{Bmatrix} = k_1 \begin{bmatrix} 1 & -1/2 & -1/2 \\ 0 & \sqrt{3}/2 & -\sqrt{3}/2 \\ k_2 & k_2 & k_2 \end{bmatrix} \begin{Bmatrix} v_a \\ v_b \\ v_c \end{Bmatrix} \tag{A.8}$$

Noticed that here the introduction of two constants k_1 and k_2. These coefficients allow matching either the instantaneous power or the signal amplitude between two and three-phase representations. The condition for instantaneous power is orthonormality,since

$$P = \mathbf{v}_{abc}^{\mathrm{T}}\mathbf{i}_{abc} = \mathbf{v}_{\alpha\beta 0}^{\mathrm{T}}\mathbf{i}_{\alpha\beta 0} \tag{A.9}$$

$$\mathbf{v}_{abc}^{\mathrm{T}}\mathbf{i}_{abc} = (\mathbf{T}_{\alpha\beta 0}\mathbf{v}_{abc})^{\mathrm{T}}\mathbf{T}_{\alpha\beta 0}\mathbf{i}_{\alpha\beta 0} \tag{A.10}$$

$$\mathbf{v}_{abc}^{\mathrm{T}}\mathbf{i}_{abc} = \mathbf{v}_{abc}^{\mathrm{T}}\mathbf{T}_{\alpha\beta 0}^{\mathrm{T}}\mathbf{T}_{\alpha\beta 0}\mathbf{i}_{\alpha\beta 0} \tag{A.11}$$

Solving for k_1 and k_2 and substituting into the matrix yields:

$$\mathbf{T}_{\alpha\beta 0} = \begin{bmatrix} \sqrt{2/3} & -1/\sqrt{6} & -1/\sqrt{6} \\ 0 & 1/\sqrt{2} & -1/\sqrt{2} \\ 1/\sqrt{3} & 1/\sqrt{3} & 1/\sqrt{3} \end{bmatrix} \tag{A.12}$$

This matrix constitutes the Clarke transformation for three-phase systems. it is worth noting that, when applied to three-phase quantities, the peak values of their two-phase representations will be scaled by a factor of $\sqrt{3/2}$. This property clearly shows that the conversion of instantaneous power does not preserve the amplitude of the signals.

When apply this transformation to the three-phase model, it yields:

$$\mathbf{v}_{\alpha\beta 0} = \mathbf{T}_{\alpha\beta 0}\mathbf{L}_{abc}\mathbf{T}_{\alpha\beta 0}^{\mathrm{T}}\mathbf{i}_{\alpha\beta 0}{}' + \mathbf{T}_{\alpha\beta 0}\mathbf{R}_{abc}\mathbf{T}_{\alpha\beta 0}^{\mathrm{T}}\mathbf{i}_{\alpha\beta 0} + \mathbf{T}_{\alpha\beta 0}\mathbf{e} \tag{A.13}$$

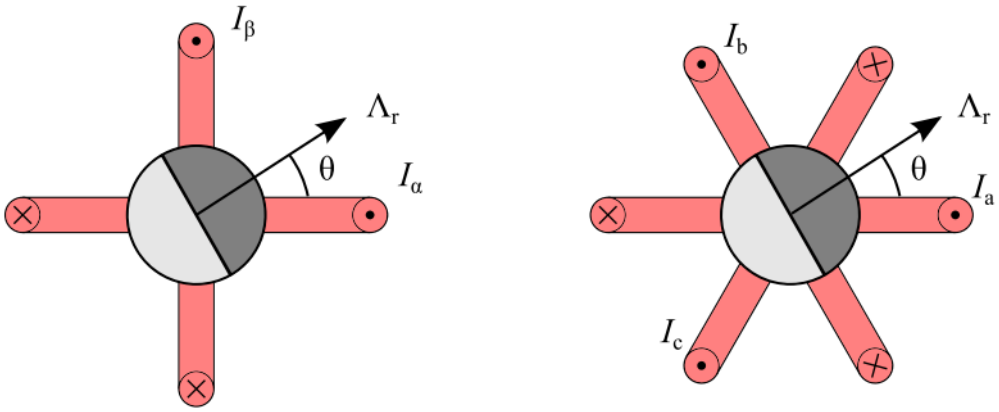

Fig. A.3 Two-phase and three-phase model of PMSM.

$$\begin{Bmatrix} v_\alpha \\ v_\beta \end{Bmatrix} = L \begin{Bmatrix} i_\alpha \\ i_\beta \end{Bmatrix}' + R \begin{Bmatrix} i_\alpha \\ i_\beta \end{Bmatrix} + \Lambda\Omega \begin{Bmatrix} -\sin(\Omega t) \\ \cos(\Omega t) \end{Bmatrix} \tag{A.14}$$

where $R = R_s$, $L = \sqrt{3/2}L_s$ and $\Lambda = \sqrt{3/2}\Lambda_r$. The third equation was neglected in the matrix form for simplicity.

The same set of equations can be represented in complex notation. Let:

$$\begin{cases} v_{\alpha\beta} = v_\alpha + \mathrm{j}v_\beta \\ i_{\alpha\beta} = i_\alpha + \mathrm{j}i_\beta \\ \mathrm{e}^{\mathrm{j}\Omega t} = \cos(\Omega t) + \mathrm{j}\cos(\Omega t) \end{cases} \tag{A.15}$$

Hence,

$$v_{\alpha\beta} = L{i_{\alpha\beta}}' + Ri_{\alpha\beta} + \mathrm{j}\Omega\Lambda\mathrm{e}^{\mathrm{j}\Omega t} \tag{A.16}$$

Moreover, consider the following system as shown in Fig.A.3, the same rotor is positioned inside two-phase ($\alpha\beta$) and three-phase (abc) winding layouts. Derived from the Lorentz force term, the magnitude of the torque is calculated as:

$$\begin{cases} T_{\alpha\beta} = I_\alpha\Lambda_r\sin\theta + I_\beta\Lambda_r\cos\theta \\ T_{abc} = I_a\Lambda_r\sin\theta + I_b\Lambda_r\sin(\theta - 2\pi/3) + I_c\Lambda_r\sin(\theta + 2\pi/3) \end{cases} \tag{A.17}$$

Suppose that the rotor spins at constant speed ω. To have maximum and constant output torque, the current imposed in the windings should try to keep orthogonality with respect to the PM flux linkage.

To do this, currents must be sinusoids with opportune phase lags and an angular frequency that matches the angular speed of the rotor.

$$\begin{cases} T_2 = I_2\Lambda_r \sin^2(\omega t) + I_2\Lambda_r \cos^2(\omega t) \\ T_{abc} = I_3\Lambda_r \sin^2\omega + I_3\Lambda_r \sin^2(\omega t - 2\pi/3) + I_3\Lambda_r \sin^2(\omega t + 2\pi/3) \end{cases} \tag{A.18}$$

The indexes 2 and 3 denotes the amplitude of both torque and current for the two and three-phase system. Applying trigonometric identities:

$$\sin^2\theta + \cos^2\theta = 1 \tag{A.19}$$

$$\sin^2\theta = \frac{1+\cos 2\theta}{2} \tag{A.20}$$

the final expression for torque are:

$$\begin{cases} T_2 = I_2\Lambda_r \\ T_3 = \frac{3}{2} I_3\Lambda_r \end{cases} \tag{A.21}$$

Since the mechanical power produced in one system must equate the other and the speed is the same in both cases $T_2 = T_3 = T$. Thus:

$$I_2\Lambda_r = \frac{3}{2} I_3\Lambda_r \tag{A.22}$$

There is another commonly used two-phase model which is called the Park transformation, different from the previous Clarke transformation, in this case as shown in Fig.A.4, the two-phase reference fixed to the stator is transformed into a two-phase reference which is fixed to the rotor. Considering a rotor angular displacement θ, a rotation of the same magnitude but with opposite sign should be applied to the stator quantities. In other words, if the rotor presents a displacement θ, a frame fixed to the rotor sees that the stator presents a displacement $-\theta$.

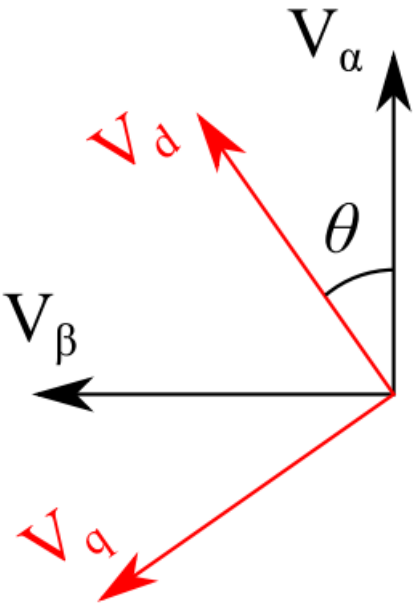

Fig. A.4 Two-phase and three-phase model of PMSM.

$$\mathbf{v}_{dq0} = \mathbf{T}_{dq0}\mathbf{v}_{\alpha\beta0} \tag{A.23}$$

$$\mathbf{T}_{dq0} = \mathbf{R}(-\theta) = \begin{bmatrix} \cos\theta & \sin\theta & 0 \\ -\sin\theta & \cos\theta & 0 \\ 0 & 0 & 1 \end{bmatrix} \tag{A.24}$$

The matrix above is known as the Park transformation. If constant speed Ω is assumed and the third column and row are omitted for simplicity.

$$\mathbf{T}_{dq} = \begin{bmatrix} \cos(\Omega t) & \sin(\Omega t) \\ -\sin(\Omega t) & \cos(\Omega t) \end{bmatrix} \tag{A.25}$$

Since rotation matrices are intrinsically orthonormal, the resulting set of equations preserves the instantaneous power of the original system as well. The advantage of applying this transformation resides in the fact that alternating currents become constant values.

Following the same approach as for the three-phase transformation results in:

$$\begin{Bmatrix} v_d \\ v_q \end{Bmatrix} = L\begin{Bmatrix} i_d \\ i_q \end{Bmatrix}' + \begin{bmatrix} R & -L\Omega \\ L\Omega & R \end{bmatrix}\begin{Bmatrix} i_d \\ i_q \end{Bmatrix} + \Lambda\Omega\begin{Bmatrix} 0 \\ 1 \end{Bmatrix} \tag{A.26}$$

similarly, it can be represented in the complex notation form:

$$\begin{cases} v_{dq} = v_d + \mathrm{j}v_q \\ i_{dq} = i_d + \mathrm{j}i_q \end{cases} \tag{A.27}$$

$$v_{dq} = Li_{dq}{}' + (R + \mathrm{j}\Omega L)i_{dq} + \mathrm{j}\Omega\Lambda \tag{A.28}$$

Suppose the system is fed by a three-phase input voltage:

$$\begin{cases} v_a = -V_x \sin(\omega t) \\ v_b = -V_x \sin(\omega t - 2\pi/3) \\ v_c = -V_x \sin(\omega t + 2\pi/3) \end{cases} \tag{A.29}$$

In dq axes, this three-phase voltage set becomes:

$$\begin{cases} v_d = \sqrt{\frac{3}{2}} V_x \sin(\theta - \omega t) \\ v_q = \sqrt{\frac{3}{2}} V_x \cos(\theta - \omega t) \end{cases} \tag{A.30}$$

If the peak voltage in the three-phase representation is limited by the DC bus voltage V_{dc}, it can be stated that:

$$\left|v_{dq}\right| = \sqrt{v_d^2 + v_q^2} \leq \sqrt{\frac{3}{2}} V_{\mathrm{dc}} \tag{A.31}$$

Considering steady-state operation:

$$v_{dq} = (R + \mathrm{j}\Omega L)(i_d + \mathrm{j}i_q) + \mathrm{j}\Omega\Lambda \tag{A.32}$$

$$v_{dq} = Ri_d - \Omega L i_q + \mathrm{j}(Ri_q + \Omega L i_d + \Omega\Lambda) \tag{A.33}$$

$$\left|v_{dq}\right| = \sqrt{(Ri_d - \Omega L i_q)^2 + (Ri_q + \Omega L i_d + \Omega\Lambda)^2} \tag{A.34}$$

Introducing the constraint on the peak voltage produces:

$$(Ri_d - \Omega L i_q)^2 + (Ri_q + \Omega L i_d + \Omega\Lambda)^2 \leq \frac{3}{2} V_{\mathrm{dc}}^2 \tag{A.35}$$

If the resistance term is neglected, the currents are limited by the circle

$$(i_q)^2 + (i_d + \frac{\Lambda}{L})^2 \leq \frac{3}{2}\frac{V_{\mathrm{dc}}^2}{\Omega^2 L^2} \tag{A.36}$$

Substituting the actual three-phase parameters, it yields:

$$(i_q)^2 + (i_d + \frac{\sqrt{3/2}\Lambda_r}{L})^2 \leq \frac{V_{\mathrm{dc}}^2}{\Omega^2 L_s^2} \tag{A.37}$$